Analysis for reaction mechanism of cathode materials for lithium–sulfur batteries

Yao Xiao

Analysis for reaction mechanism of cathode materials for lithium–sulfur batteries

Yao Xiao

Graduate School of Human and Environmental Studies

Kyoto University

Supervised by

Prof. Dr. Yoshiharu Uchimoto

Contents

Chapter 1 Introduction

1.1   Research background

Currently, fossil fuels, including petroleum, coal, and natural gas, are essential energy sources. However, the development of human society led to the increase in energy requirements. The excessive exploitation and consumption of fossil fuels has disrupted the original carbon balance in the environment and caused a significant greenhouse effect. Moreover burning fossil fuels has contributed to environmental pollution, including dust and toxic gas pollution.[1-3] Therefore, the exploitation of renewable new energy sources, including solar, geothermal, and wind energy has become a research hotspot. Nowadays, fossil fuels are mainly used as electric power supply sources and for transportation, particularly as automobile fuel. Therefore, electric vehicles can reduce the demand for crude oil. Currently electric vehicles, which do not consume conventional fuel, have eliminated many drawbacks and restrictive factors, and have entered a period of rapid development. The battery is the most critical component of electric vehicles; moreover, currently, lithium-ion batteries are the main type of batteries on the market and the most widely used secondary batteries.[4-6]

1.2   Lithium-ion secondary batteries

Lithium-ion secondary batteries play a very important role in modern society. Currently, rechargeable secondary batteries can be roughly divided into three generations. Lead-acid batteries are first-generation secondary rechargeable batteries, and nickel-cadmium and nickel-metal hydride batteries are second-generation secondary batteries. The energy density of these types of batteries is insufficient; therefore, they are mostly used in hybrid vehicles only to start the engine or during low fuel consumption episodes. Current third-generation electric vehicles use advanced lithium-ion batteries. The number of pure electric vehicles on the market has gradually increased with increasing specific energy of electric vehicle batteries. Owing to their high electrode specific capacity and energy density, lithium-ion batteries are widely used not only for electric vehicles but also for different applications.[2, 6-8]

Since Sony Corporation successfully introduced lithium-ion batteries, they have been extensively used in different portable electronic devices, such as mobile phones, laptops, and tablets. Moreover, lithium-ion batteries are used for large-scale energy storage applications, including power vehicles and power station energy storage systems. Therefore, the lithium-ion battery industry has received increasing attention. The development of electric vehicles and portable electronic devices drove the increase in the demand for and functional requirements of lithium-ion batteries. As the demand for lithium-ion batteries increased, their high energy storage capacity and safety have gradually increased and their cost has decreased. The energy density of conventional lithium-ion batteries has approached the development limit. Hence, it has become increasingly difficult to meet the energy requirements of portable devices with ever-increasing functions and high-range electric vehicles. Therefore, the development has higher capabilities. Furthermore, high-energy-density batteries should meet the critical

development needs of human society.[9-11]

Herein, we briefly describe the operation of lithium-ion secondary batteries. The schematic diagram of a representative commercial lithium-ion secondary battery is presented in Figure 1.1.[12] A lithium-containing transition metal oxide, such as $LiCoO_2$, graphite, and an organic electrolyte in which lithium salts are dissolved are used as the cathode, anode, and electrolyte, respectively. The charge–discharge process of this battery can be expressed as follows:

Cathode: $Li_{1-x}CoO_2 + xLi^+ + xe^- \rightleftarrows LiCoO_2$ (1)

Anode: $Li_xC_6 \rightleftarrows xLi^+ + xe^- + C_6$ (2)

Overall: $Li_{1-x}CoO_2 + Li_xC_6 \rightleftarrows LiCoO_2 + C_6$ (3)
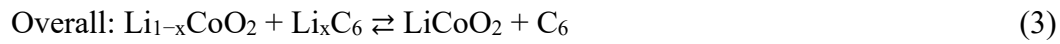
Currently, typical cathode materials for lithium-ion secondary batteries include layered oxides[13] (e.g., $LiCoO_2$), spinel oxides[14, 15] (e.g., $LiMn_2O_4$), and olivine oxides[16, 17] (e.g., $LiFePO_4$). Furthermore, sulfur-based materials with high theoretical capacity have been drawing increasing attention as next-generation cathode materials.

The maximum capacity of layered oxide-based cathode materials (e.g., $LiCoO_2$) is approximately 300 mAh/g; however, because of their low power density and thermal stability, these materials are often used for small mobile devices which do not require high energy density. Although the thermal stability and output performance of spinel- and olivine-type cathode materials (e.g., $LiMn_2O_4$ and $LiFePO_4$, respectively) are higher than those of layered oxide-based cathode materials, they are typically used for electric vehicles and large-scale storage battery systems because of their relatively low capacity (150 mAh/g) and conductivity. Recently, the demand for batteries with high energy and power density has increased rapidly; therefore, it is necessary to improve the current cathode materials and, simultaneously, search for new high-performance cathode materials.

The rapid development of electronic equipment and energy-storage devices has led to an increasing demand for high-energy storage systems. Sulfur-based cathode materials have received much attention because of their high theoretical specific capacity, low cost, high availability, and environmental friendliness.[18-21] Therefore, sulfur cathodes are considered promising components of next-generation energy-storage systems.[22-24] However, because of the chemical properties of sulfur, the safety and cycle performance of sulfur cathodes should be improved.

1.3   Brief introduction of lithium–sulfur batteries

Lithium–sulfur batteries are a new generation of lithium secondary batteries. Unlike the traditional transition metal oxide lithium-ion batteries, lithium–sulfur batteries consist of elemental sulfur, lithium metal, and conventional organic ethers as the cathode, anode, and electrolyte, respectively. During battery operation, sulfur can contribute two electrons. Therefore, the specific capacity and energy density of sulfur cathodes can reach extremely high values (1675 mAh/g and 2600 Wh/kg, respectively), which exceed those of the current lithium-ion battery cathodes.[25-27] Because elemental sulfur is abundant, inexpensive compared with metallic minerals, low-toxic, environmentally friendly, and degradable, it presents great potential for large-scale practical applications.

1.3.1   Liquid lithium–sulfur batteries

Conventional liquid lithium–sulfur batteries comprise a cathode, an anode, and a liquid electrolyte with good ionic conductivity. Typical lithium–sulfur battery cathodes consist of sulfur, as the active material, a conductive material, a binder, and a current collector, which supports the electrode. However, some self-supporting cathodes do not require the use of binders and additional current collectors. Owing to the poor conductivities of sulfur and Li_2S, the discharge product, the positive conductive network of lithium–sulfur batteries requires high conductivity and must be fully and uniformly combined with sulfur, such that sulfur can fully combine electrons and lithium ions and store energy.[28, 29] Metal lithium foil is the most commonly used anode for lithium–sulfur batteries. The electrolytes of conventional lithium–sulfur batteries are organic ether electrolytes that can dissolve lithium salts; in addition, a polymer

separator is used to separate the cathode and anode. The final discharge product of lithium–sulfur batteries is Li$_2$S, and the corresponding electrochemical reaction is: S$_8$ + 16Li$^+$ + 16e$^-$ → 8Li$_2$S; E = 2.15 V vs. Li$^+$/Li. The charge–discharge curves of a typical lithium–sulfur battery are illustrated in Figure 1.2.[25]

However, lithium–sulfur batteries still present many drawbacks that should be addressed, including cathode and anode design, electrolyte optimization, and overall battery structure design. These problems mainly on:

(1) The electronic and ionic conductivities of sulfur and Li$_2$S are low and result in the low utilization of active materials and difficulty in exerting the true energy density advantage.

(2) During discharge, sulfur gradually produces soluble polysulfides. The soluble discharge products cause a shuttle effect which corrodes the lithium metal anode and redistributes lithium inside the battery, and therefore, causes the loss of active materials.

(3) The volume change of the cathode material in lithium–sulfur batteries before and after the charge–discharge process is extremely high (density ratio S$_8$/Li$_2$S = 2.03/1.67). The formation of Li$_2$S from elemental sulfur causes a volume change of 80% during continuous charge–discharge, and the continuous expansion and contraction causes damage to the cathode structure, which results in a significant decline in battery performance. This is particularly noticeable for high-load electrodes with practical application potential.

(4) Lithium metal reacts with the electrolyte and forms an unstable solid electrolyte interface (SEI) film. During battery operation, lithium metal is consumed and can also form lithium dendrites, which hinder the large-scale use of lithium–sulfur batteries.

1.3.2 Solid-state lithium–sulfur batteries

Compared with liquid batteries, all-solid-state batteries present the following advantages.

(1) Excellent safety performance. Because all-solid-state batteries comprise only solid components (electrolyte, cathode, and anode) and no flammable organic electrolytes, burning or explosion accidents are prevented.

(2) High energy density. Because all-solid-state batteries do not contain liquid electrolytes and lithium metal can be used directly as the anode, the energy density of the batteries is high. In addition, the wide electrochemical windows of solid electrolytes and high-voltage cathodes greatly increase the energy density of all-solid-state batteries.

(3) Wide operating temperature range. Liquid electrolytes freeze at low temperatures, which prevents charging–discharging and greatly affects battery performance. All-solid-state batteries can conduct lithium ions at high and low temperatures; therefore, they can be used under extreme environment conditions.

(4) Flexibility. Polymer electrolytes are flexible and can be used to construct thin-film and flexible batteries, which are required for future wearable devices.

Similar to all-solid-state batteries, sulfur solid-state batteries consist of a cathode, an anode, the sulfur electrolyte, and a collector. The assembly of sulfur solid-state batteries is similar. The sulfur solid electrolyte is prepared using high-energy ball milling, high-temperature quenching, and the cooling or the solution method. The cathode typically consists of a uniform mixture of active material, solid electrolyte, and conductive carbon black with a predetermined mass ratio that confers it high ionic and electronic conductivities. The anode usually consists of graphite lithium metal, or a lithium alloy. Because the sulfide solid electrolyte is very sensitive to air, all-solid-state batteries should be assembled under argon atmosphere. Typically, a special battery mold is used

to assemble all-solid-state batteries. First, a predetermined amount of sulfur solid electrolyte is weighed and added to the mold. Next, the electrolyte is flattened. Thereafter, the cathode material is weighed, evenly spread on one side of the solid electrolyte, and placed in a tablet press to be cold pressed into a sheet. Typically, freshly assembled solid-state batteries are allowed to reach steady state before electrochemical testing.

1.4   Liquid lithium–sulfur batteries

1.4.1   Cathode materials for liquid lithium–sulfur batteries

The electrolytes of lithium–sulfur batteries are different from those used for conventional commercial lithium-ion batteries and consist of organic ethers, such as ethylene glycol dimethyl ether, dioxolane, and tetrahydrofuran. The main research areas for conventional lithium–sulfur batteries with liquid electrolytes include cathode structure design, electrolyte component optimization, lithium salt additives, and lithium metal protection.

The conductivity of elemental sulfur at room temperature is low (5×10^{-30} S/cm); therefore, elemental sulfur is an electronic insulating material and cannot be used by itself as cathode material for lithium-sulfur batteries. Therefore, a conductive agent must be added to increase the overall conductivity of the cathode. In addition, the "shuttle effect" of lithium polysulfide in liquid lithium–sulfur batteries leads to a large amount of active materials separating from the cathode current collector and dissolving in the electrolyte. This causes problems, such as low utilization of active materials and low specific capacity. Therefore, when the cathode material powder is prepared, sulfur is typically uniformly dispersed in a conductive carrier, which confines polysulfide ions and increases the conductivity of the cathode and the utilization rate of active materials. To achieve a high overall specific capacity, carbon, which is the lightest conductive material, is the first conductive carrier choice.

In 2009, Ji et al.[30] used CMK-3, an ordered mesoporous carbon, as sulfur carrier for the first time and studied the electrochemical performance of the CMK-3/S composite as cathode material for lithium–sulfur batteries. As illustrated in Figure 1.3, the diameters of the carbon nanotubes and pores of CMK-3 were approximately 6.5 nm

and approximately 3 nm, respectively. The high-temperature sulfur melting method was used to introduce sulfur into the pores of CMK-3. The dispersibility of elemental sulfur further increased the conductivity of the cathode composite material, and the pore structure of CMK-3 restrained the lithium polysulfide produced during the electrochemical reaction. This improved the charge–discharge and cycle performances of the analyzed battery. This study prompted an upsurge in the research of lithium–sulfur battery cathode composite materials. Different carbon materials, such as porous carbon, graphene, carbon nanotubes, carbon nanofibers, and combined structured carbon have been used for sulfur cathodes. Experiments have revealed that these carbon materials can change the conductivity of sulfur anodes to varying degrees, improve the dispersion of sulfur active material, inhibit the shuttle effect, and improve the electrochemical performance of lithium–sulfur batteries.

According to pore diameter, porous carbon can be divided into microporous, mesoporous, porous, and hierarchical porous carbon. Typically, the pore diameter of microporous carbon is below 2 nm, which is smaller than the diameter of S_8 molecules. Therefore, when S_8 is combined with microporous carbon via melting, elemental sulfur cannot be present in the mesopores as S_8 molecules, but only as S_2 or S_4 molecules with low polymerization degrees.[31, 32] Hence, the discharge reaction that occurs is a redox reaction in which sulfur and lithium generate Li_2S and mesophase lithium polysulfide does not form. Han et al.[33] used heat-treated and alkali-etched macadamia nut shells as raw material to successfully prepare microporous carbon materials (c-MNS; pore diameter < 0.6 nm) and used them as sulfur carrier. The sulfur–carbon composite comprising short-chain small-molecule sulfur compounded with microporous carbon presented a very high specific discharge capacity. However the voltage plateau of the battery featuring this composite as the cathode was low; moreover, the assembled

battery presented only one inclined discharge plateau instead of two conventional discharge plateaus, which are typical for lithium–sulfur batteries. This was ascribed to the strong adsorption ability of microporous carbon for lithium polysulfide and the changes in the existence of active substances. However, because of the limited quantity of prepared c-MNS, the loading capacity of small-molecule sulfur was limited. When the sulfur loading of the composite cathode was increased, the sulfur that could not enter the micropores was present as ring-shaped S_8 molecules. Therefore, the inclined single discharge plateau was replaced by three discharge plateau (the first two discharge curves) or two discharge platforms (third discharge curve); the discharge capacity also decreased.

Recently, carbon materials with one-dimensional linear structures, such as carbon nanotubes (CNTs) and carbon nanofibers have become research hotspots. Traditional sulfur cathodes require non-conductive binders, which reduce the sulfur content of the cathode and decrease the continuous ion–electron conduction path during electrochemical reaction. Therefore, when carbon nanowires and CNTs, which possess excellent conductivity and can easily form three-dimensional conductive networks, are combined with sulfur to prepare sulfur cathode composite materials, they can shorten the transmission distance of lithium ions and decrease the impedance of the cathode; furthermore, high-aspect-ratio (>104) CNTs or carbon nanowires can be used to prepare self-supporting composite electrodes.[34-36] Furthermore, the three-dimensional structures built using CNTs or carbon nanowires can provide ample space for sulfur loading. Two main methods are typically used to prepare CNT/carbon nanowire–sulfur composite electrodes. (1) First, a flexible CNT/carbon nanowire structure is prepared, and then sulfur is directly infiltrated into the structure using chemical or physical methods to obtain composite cathodes. (2) The CNTs/carbon nanowires are combined

with sulfur and then are assembled into composite cathodes with different morphologies.[37, 38] However, during the early research stages on the use of CNTs and carbon nanofibers as lithium–sulfur battery cathode carriers, it was determined that it was difficult to coat sulfur uniformly on the surface of one-dimensional carbon materials when preparing composite cathodes via high-temperature melting; furthermore, the electrochemical performance of the prepared cathodes was poor.[39-41] Even if sulfur was uniformly coated on the surface of CNTs or carbon nanowires, the electrochemical performance of the prepared cathodes was still limited because sulfur was be exposed to the outside environment and the dissolution and shuttle of lithium polysulfide could not be effectively avoided. This reduced the utilization of active materials and ultimately affected battery cycle performance.

To solve the aforementioned problems, researchers have used metastable small-molecule sulfur (i.e., S_2, S_3, and S_4 (S_{2-4})) to prepare CNT–sulfur composite cathodes, and utilized the enclosed space of CNTs nanotube to load S_{2-4}. This increased electrode conductivity and also prevented the formation of mesophase lithium polysulfide because small-molecule sulfur reacted with lithium to form Li_2S. Guo et al.[42] prepared disordered CNTs using the anodic aluminum oxide (AAO) template synthesis method. The effect of different heat treatment temperatures on sulfur-loaded CNTs was studied, and the results indicated that high temperature (500 °C) could cause sulfur vapor (S_6 or S_2) to enter the CNTs; furthermore, because chemical bonds could be formed between sulfur and carbon, the active material would not be easily lost during charge–discharge. The lithium–sulfur battery assembled using the aforementioned composite electrode presented excellent performance. The CNT–S_{2-4} composite electrode prepared by Xin et al.[31] presented a single discharge plateau (at approximately 1.9 V) at a current density of 5 C and a discharge specific capacity as high as 1670 mAh/g (Figure 1.4). Moreover,

after 200 charge–discharge cycles, the battery still maintained a capacity of 800 mAh/g.

1.4.2　Liquid lithium–sulfur battery electrolytes

Lithium–sulfur battery electrolytes are different from those of conventional lithium-ion batteries. Most lithium-ion battery electrolytes are carbonate-based; however, ester-based electrolytes cannot be used for conventional lithium–sulfur batteries. Yim et al.[43] reported that lithium polysulfide, an intermediate product of sulfur discharge, underwent nucleophilic substitution with ester electrolytes, which led to the irreversible consumption of the active material (Figure 1.5). Therefore sulfur-containing cathodes would fail to work in ester liquid electrolytes. Once the formation of polysulfides can be effectively controlled in cathode systems by using sulfur–polyacrylonitrile (S–PAN) or short-chain small-molecule sulfur as the cathode, ester electrolytes can still be used to achieve the normal battery operation.[31, 44] However, in most lithium–sulfur battery systems, the production of lithium polysulfide is inevitable. Therefore, ester-based organic liquid electrolytes have been replaced with ether-based electrolytes, such as 1,2-dimethoxyethane (DME) and 1,3-dioxolane (DOL). Moreover, mixed solvents are widely used in lithium–sulfur batteries. The main components of lithium–sulfur battery electrolytes are organic solvents, lithium salts, and functional additives. Therefore, to optimize lithium–sulfur battery electrolytes the solvent-to-lithium salt-to-additives ratio should be selectively adjusted. Because the electrolyte comes in contact with both the cathode and anode, optimizing electrolyte composition can simultaneously improve the function and efficiency of cathodes and anodes of lithium–sulfur batteries.

The partial dissolution and conversion of polysulfides in electrolytes is the basis for achieving high sulfur utilization. However, excessive dissolution of polysulfides can cause significant redistribution and active material shuttling, which decrease battery

13

stability. For lithium–sulfur batteries, the electrolyte system should present high ionic conductivity; however, polysulfide dissolution is facilitated as the ionic conductivity of the electrolyte increases. Carbone et al.[45] studied the effects of ether electrolytes with different chain lengths on the performance of lithium–sulfur batteries and reported that the longer the solvent chain, the more difficult the dissolution of polysulfides. Moreover, the shuttle effect was suppressed when electrolytes with long solvent chains were used. Furthermore, conductivity decreased as solvent chain length increased and the sulfur utilization rate of lithium–sulfur batteries decreased. Therefore, to construct performant batteries, the solvent should present adequate ionic conductivity and the excessive dissolution of polysulfides should be inhibited. Gu et al.[46] used 1,3-(1,1,2,2-tetrafluoroethoxy)propane, a fluorinated diether (FDE), as the electrolyte cosolvent for lithium–sulfur batteries, and selected the appropriate The components of viscosity and ionic conductivity greatly improve the performance of lithium–sulfur batteries. In the absence of $LiNO_3$ additives, when electrolytes with FDE volume fractions higher than 70% were used, the coulombic efficiency of lithium–sulfur batteries reached 99% and the capacity reached 700 mAh/g after 200 cycles. Azimi et al.[47] used 1,1,2,2-tetrafluoroethyl 2,2,3,3-tetrafluoropropyl ether (TTE) as the electrolyte for lithium–sulfur batteries. Lithium polysulfide is used in this type of electrolyte. The solubility has been greatly reduced, so the performance of lithium–sulfur batteries has also been improved. Cuisiner et al.[48] used a combination of $(ACN)_2$-LiTFSI (ACN and LiTSFi denote acetonitrile and lithium bis(trifluoromethanesulfonyl)imide, respectively) and hydrofluoroether as lithium–sulfur battery electrolyte (Figure 1.6). The composition of this electrolyte was stable in the presence of lithium metal, controlled the dissolution of lithium polysulfide, and regulated the deposition of Li_2S. The reversible capacity of lithium–sulfur batteries featuring this electrolyte reached 1300-1400 mAh/g. The

performance of lithium–sulfur batteries can also be improved by adjusting the electrolyte composition to increase salt concentration in the electrolyte. A very high salt concentration can present a similar effect with the common ion and can inhibit the excessive dissolution and diffusion of polysulfides. Because the fraction of salt in the electrolyte exceeded that of the solvent, this type of electrolyte has been termed "solvent in salt".[49] Lithium–sulfur batteries featuring this type of electrolyte can reach extremely high coulombic efficiency in the absence of $LiNO_3$, which confirms that polysulfide shuttling is greatly suppressed. Moreover, high salt concentrations facilitate the formation of a stable protective layer on the surface of lithium metal.

The self-discharge behavior of lithium–sulfur batteries is noticeable because both sulfur and polysulfide are soluble in organic electrolytes, and the different states of the cathode also represent different states of charge (SOC). Long-chain polysulfides present strong dissolving ability during mid-discharge. Once in the SOC state that is not fully charged, it is easy to cause the irreversible loss of polysulfide redistribution and migration to the anode.[50] Therefore, battery electrolyte design is extremely important for solving such problems in practice. Wang et al.[51] used $PP_{13}TFSI$ ionic liquid to improve the performance of lithium–sulfur battery electrolytes by inhibiting the dissolution of lithium polysulfide. When the electrolyte contained 0.2 M $LiNO_3$, 100% SOC lithium–sulfur batteries was stored. Moreover, no capacity loss was observed after two days, whereas the capacity loss of common ether electrolytes reached 40%.

1.4.3 Anode materials for liquid lithium–sulfur batteries

Lithium metal is the most popular anode material for liquid lithium–sulfur batteries, and the use of lithium metal is an important prerequisite for ensuring the high energy density of lithium–sulfur batteries. Lithium metal presents the highest negative potential (-3.04 V vs. H^+/H_2), low density (0.53 g/cm^3), and extremely high theoretical specific capacity (3860 mAh/g). When lithium metal is used as the anode, no additional materials, such as conductive agents, binders, and conductive current collectors are required. Therefore, lithium metal can achieve a higher specific capacity than traditional anodes, such as silicon carbon and graphite anodes, which directly increases the actual energy density of batteries. However, lithium metal is active and difficult to store. Moreover, when lithium metal is used as the anode in batteries featuring organic electrolytes, it will directly react with electrolyte components to form an unstable SEI.[52] The unstable SEI induces changes in the ion concentration on the surface of lithium metal, which lead to the uneven deposition of lithium metal and the formation of lithium dendrites.[53] Because lithium dendrites grow quickly, they can pierce the separator, which short circuits the battery and poses a high safety hazard.[54] The unstable SEI undergoes continuous fragmentation, dissolution, and regeneration during long battery cycles, and that consumes the lithium metal anode and electrolyte components and causes the gradual breakdown of lithium metal. Furthermore, the lithium metal anode causes a large volume expansion during dissolution and deposition. These processes pulverize lithium metal and cause it to partly lose its current collecting ability, which leads to a rapid battery capacity loss. The polysulfide at the sulfur cathode of lithium–sulfur batteries is extremely corrosive and migrates to the surface of lithium metal where it causes corrosion (shuttle effect). Therefore, to produce lithium–sulfur batteries with high specific energy, the problem of lithium metal anodes must be properly solved.

To date, the studies on lithium metal anodes have focused on the following three aspects. (1) In situ protecting lithium metal using electrolyte additives or by changing the electrolyte composition to form stable SEI films on the surface of lithium metal during charge–discharge.[55] (2) Designing lithium metal framework structures. A high current density tends to amplify the local difference of the lithium metal surface and produce an uneven ion flow, which eventually produces lithium dendrites.[56] Therefore, reducing the local current density by using a material with a high specific surface area as the lithium metal framework can decrease the volume expansion of lithium metal during dissolution–deposition and also decrease the local current density and suppress the uneven ion flow. (3) Ex situ protecting lithium metal by growing a protective layer on its surface before cycling. This protective layer should possess a certain ionic conductivity, high mechanical strength, and dense morphology, good for lithium metal and electrolyte liquid composition is relatively stable and other characteristics.[57]

1.5   Solid-state lithium–sulfur batteries

1.5.1   Cathode materials for all-solid-state lithium–sulfur batteries

Currently, the most commonly used cathode materials for sulfide solid-state batteries are transition metal oxides, such as $LiCoO_2$, $LiNi_{1/3}Co_{1/3}Mn_{1/3}O_2$, and $LiMn_2O_4$, and sulfur-based materials, such as sulfur, Li_2S, and metal sulfides.

Layered $LiCoO_2$ was first commercialized as cathode materials for liquid batteries. However, $LiCoO_2$ presents a low specific capacity and poor multiplicative performance. Moreover, a space charge layer forms between $LiCoO_2$ and sulfide solid electrolytes; therefore, the interfacial impedance is large, which greatly limits its use for solid-state batteries. Ohta et al.[58] have developed a new $LiCoO_2$ cathode for liquid batteries by coating the $LiCoO_2$ surface with a layer of $LiNbO_3$. This can effectively inhibit the formation of the space charge layer and increase battery power density. Sakuda et al.[59] reported that the electrochemistry of $LiCoO_2$ can be improved by coating its surface with an electronic conducting layer (NiS or CoS), Woo et al.[60] indicated that the interfacial impedance between the cathode and the solid electrolyte can be decreased via the atomic deposition of Al_2O_3 layers on the $LiCoO_2$ cathode.

$LiNi_{1/3}Co_{1/3}Mn_{1/3}O_2$, which was first reported by Ohzuku and Makimura,[61] presents the highest theoretical capacity of all Li–Ni–Co–Mn cathode materials and excellent cycling performance. Kitaura et al.[62] reported a sulfide solid-state battery with $LiNi_{1/3}Co_{1/3}Mn_{1/3}O_2$ and $Li_{10}GeP_2S_{12}$ as the cathode and electrolyte, respectively, which exhibited excellent charge–discharge performance. Recently, Iwasaki et al.[63] coated $LiNi_{1/3}Co_{1/3}Mn_{1/3}O_2$ with a $LiNbO_2$ layer to reduce the cathode–electrolyte interface impedance and further improve the electrochemical performance of the all-solid-state battery.

LiMn$_2$O$_4$ is another important cathode material with spinel structure. Despite its low discharge capacity, its reversible performance is good. Batteries featuring sulfide, LiMn$_2$O$_4$, and indium as the solid electrolyte, cathode, and anode, respectively, present better charge–discharge performance; however, their interfacial impedance is high, and can be decreased via cladding and other methods, which improve battery cycling and rate performance.

Sulfur presents a high theoretical energy density (2600 Wh/kg) and is one of the most promising cathode materials for lithium–sulfur batteries. However, when sulfur is used as the cathode, it reacts with the electrolyte. This causes a shuttle effect and leads to the consumption of the active substances, which results in poor cycling performance. Replacing liquid electrolytes with solid electrolytes can completely prevent sulfur dissolution in electrolytes.[64] However, the ionic and electronic insulating properties of sulfur are major drawbacks for the development of sulfur cathodes. The electronic and ionic conductivity of sulfur can be improved by homogeneously mixing electronic and ionic conductor additives with sulfur.[65] Nagao et al.[66] prepared cathodes by homogeneously mixing sulfur with conductive carbon black. Moreover, they used sulfide solid electrolytes, and the all-solid-state batteries featuring composite cathodes exhibited excellent cycling and rate performance. Recently, Yao et al.[67] addressed the stress changes caused by the volume expansion of sulfur cathodes during charge–discharge. They prepared a battery with excellent performance by introducing a graphene oxide skeleton into the cathode (Figure 1.7).

Because Li$_2$S presents a theoretical capacity of 1168 mAh/g and does not undergo volume expansion during charge–discharge, it is a promising cathode candidate. However, similar to sulfur cathodes, Li$_2$S cathodes present low ionic and electronic conductivities. Han et al.[68] used a bottom-up method to prepare a battery featuring Li$_2$S,

Li_6PS_5Cl, and polyvinylpyrrolidone as the active material, electrolyte, and carbon precursor of the cathode material (Figure 1.8). Nagao et al[69] studied the effect of Li_2S particle size on the electrochemical performance of all-solid-state batteries and determined that decreasing cathode particle size can effectively improve the reversible and rate performances of batteries.

Recently, metal sulfides have received increasing attention owing to their high electrochemical activity, excellent electronic conductivity, and remarkable theoretical capacity. The interface between the sulfide cathode and the sulfide solid electrolyte is stable and presents low resistance and excellent electrochemical properties.[70] For example, TiS_2 nanoparticles and $Li_2S–P_2S_5$ were used as the composite cathode and solid electrolyte, respectively, to obtain an amorphous Li–Ti–P–S phase, and the prepared solid-state battery presented excellent electrochemical performance.[71] Chen et al[72] prepared a battery featuring a composite cathode comprising MoS_2, conductive carbon black, and Li_6PS_5Br, and the battery can be stabilized charge and discharge at 0.2 C for 700 cycles. Recently, Yao et al.[73] used the solution method to prepare Co_9O_8 nanoparticles coated with Li_7P_3Sn solid electrolyte and utilized them to assemble a battery with excellent electrochemical properties. The battery was cycled at 1.27 mA/cm^2 for 1000 cycles and still maintained a discharge capacity of approximately 421 mAh/g.

1.5.2 Solid-state electrolytes for all-solid-state lithium–sulfur batteries

Solid-state batteries present significant advantages compared with traditional batteries which feature liquid electrolytes, particularly in terms of safety. (1) Solid-state batteries do not use organic liquid electrolytes; therefore, there are no hidden dangers,

such as leakage and combustion. (2) The electrochemical window of solid electrolytes used for solid-state batteries is wide; moreover, the electrolytes are stable, which helps to improve battery energy density. (3) Solid-state battery electrolytes present a certain strength. The formation of lithium dendrites at the lithium metal anode can be prevented using ether electrolytes. The ether electrolytes used for traditional lithium–sulfur batteries are unstable in the presence of lithium metal and present extremely low flash points; moreover, the shuttling of the sulfur intermediate discharge products in ether electrolytes cannot be completely prevented. These problems can be solved using solid electrolytes; therefore, the solidification of lithium–sulfur batteries can increase their application potential.

The most important part of solid-state batteries is the solid electrolyte. Solid electrolytes can be divided into several categories, including organic polymer, oxide solid, sulfide solid, nitrogen oxide, and hydride electrolytes. Polymer electrolytes consist of long-chain organic substances, whereas the other types of solid electrolytes are inorganic substances. Several of the aforementioned electrolyte types are described below. Because the solid electrolytes used in solid-state batteries are different, the design concepts of the corresponding batteries are also different.

Organic polymeric solid electrolytes are a class of polymeric matrices dissolved with lithium salts that present lithium-ion conductivity. The lithium salts are dissociated in the polymer matrices and lithium ions move between specific polymer chain segments, which confer ion transport ability to the electrolytes. To date, polyethylene oxide (PEO), polyvinylidene fluoride (PVDF), and PAN have been studied and used as polymer matrices, and most current polymer electrolytes comprise PEO matrices.[74, 75] However, polymers are more crystalline at room temperature and the free movement of the chain segments is very limited; therefore, the ionic conductivity of polymer solid electrolytes

is typically 10^{-6} S/cm or lower. As the temperature increases, the fraction of amorphous phase of polymers and the number of polymer chain segments that can move freely increase. Typically, the number of free polymer chain segments and the movement ability of polymers greatly increase only when the temperature is above the glass transition temperature of polymers, and that is when the ionic conductivity of polymer electrolytes can meet the requirements for solid-state batteries. The operating temperatures of most of the current battery systems featuring polymer electrolytes are much higher than room temperature; therefore, polymer electrolytes cannot fully meet the practical application requirements.[76] The organic polymer electrolytes in lithium-ion polymer electrolyte systems are classified as solid or gel polymer electrolytes (SPE or GPE, respectively) because the polymer matrix can be partially filled with organic liquid plasticizers. The addition of plasticizers to polymer electrolytes greatly increases ionic conductivity and improves the interfacial contact properties; however, because plasticizers are liquid, these electrolytes cannot be strictly considered solid electrolytes. The advantages and disadvantages of organic polymer electrolytes are noticeable. They can be cast to form films, can be subjected to the roll-to-roll process used during battery manufacturing, present great potential for mass production, and are flexible enough to allow their use in wearable devices. Conversely their room-temperature ionic conductivity is low, it needed to provide the appropriate operating temperature; moreover, because of their low strength, they can be affected by problems such as lithium dendrites.

Oxide electrolytes are currently the mainstream solid-state electrolytes; furthermore, oxide solid electrolytes have been studied in depth and are used for several types of applications. Oxide electrolytes present several specific structures as follows: lithium super ionic conductor (LISICON), sodium super ionic conductor (NASICON), calcite,

anti-calcite, and garnet.[77] Oxide electrolytes present several noticeable advantages. The preparation conditions of oxide solid electrolytes are not strict and no special atmosphere is needed to protect them; moreover, oxide electrolytes can be sintered densely to increase their strength. Most lithium ions are fixed in crystal lattices via Li–O bonds. Therefore, the intrinsic ionic conductivity of solid electrolytes with this type of structure is very low, and the Li–O bonds partially break only when the temperature is sufficiently high. Owing to the high lattice stability of these structures, they can remain stable at high temperatures, and therefore, are suitable as solid electrolytes for high-temperature batteries. The room-temperature ionic conductivity of oxide electrolytes is only 10^{-7} S/cm, which is much lower than the conductivity required for room-temperature batteries.

NASICON electrolytes is a collective term used to designate solid electrolytes with the crystal structure of $Na_{1+x}Zr_2P_{3-x}Si_xO_{12}$, which are used as sodium ion conductors. NASICON electrolytes present three-dimensional ion channels, which are advantageous compared with the two-dimensional ion channels of LISICON electrolytes. By replacing all sodium ions in NASICON electrolytes with lithium ions, they can be used as solid-state lithium ion electrolytes. By adjusting the composition and element proportion in NASICON solid electrolytes, the lithium-ion channels can be adjusted to obtain solid-state lithium-ion electrolytes with NASICON structure that meet the requirements of solid-state batteries.[78, 79] Aluminum doping can be used to obtain excellent NASICON-structured lithium-ion conductors, namely $Li_{1+x}Al_xTi_{2-x}(PO_4)_3$ (LATP) and $Li_{1+x}Al_xGe_{2-x}(PO_4)_3$ (LAGP). By modifying the sintering method, the room-temperature ionic conductivity of these electrolytes can be increased to 10^{-4}-10^{-3} S/cm, which can meet the requirements for room-temperature batteries.[77] The preparation of lithium-ion conductors is simple and proceeds with high

efficiency. However the titanium and germanium ions in their composition are unstable in the presence of lithium metal and undergo reduction reactions with lithium metal, which result in interfacial side reactions and even the decomposition of the electrolyte. Therefore, the direct application of these electrolytes for lithium metal solid-state batteries is limited.[80]

Lithium-ion conductors with calcite structure consist mainly of $Li_{3x}La_{2/3-x}TiO_3$ (LLTO)-type electrolytes. The general formula of calcite is ABO_3, and the A-positions are jointly occupied by lithium and lanthanum. Lanthanum can significantly increase the vacancy concentration at the A-positions; therefore, LLTO electrolytes present very high bulk phase conductivity. The grain boundary resistance of LLTO electrolytes is extremely high, and that causes a decrease in the overall conductivity of the electrolyte. In addition, LATP electrolytes are similar to NASICON electrolytes, and the instability of titanium ions in the presence of lithium metal limits their use.

Lu et al.[81] developed lithium-rich anti-perovskite (LiRAP) electrolytes. These electrolytes, which are difficult to synthesize, consist mainly of Li_3OX (X = F, Cl, Br, I, etc.) species and present the highest lithium concentration of all lithium-ion electrolytes (10^{-3} S/cm). According to the theoretical calculations performed for Li_3OCl,[81] the binding energy of the LiCl Schottky defects is low; moreover, the ion transport mode of Li_xOCl_{1-x} electrolytes consists of defective and lithium-ion hopping conduction. However, LiRAP electrolytes are stable in the presence of lithium metal and present high ionic conductivity; therefore, they present good potential for further development.

The original structure of garnet electrolytes conforms to the general formula of garnet-type ceramics ($A_3B_2C_3O_{12}$; Figure 1.9).[82] The introduction of high-valent ions in the garnet structure can increase the lithium vacancy concentration inside crystals,

which boosts the mobility of lithium ions in the ceramic lattice. $Li_5La_3Ta_2O_{12}$ and $Li_3La_2Nb_2O_{12}$ were designed by Thaangadurai et al.[83] who added pentavalent cations into the ceramic lattice, which increased the conductivity of the ceramics to 10^{-6} S/cm. The most popular garnet-type of lithium-ion electrolyte ($Li_7La_3Zr_2O_{12}$) with a very high ionic conductivity (3×10^{-4} S/cm) was designed by Murugan et al.[84] Garnet electrolytes are more stable than other solid electrolytes in the presence of lithium metal; this is an advantage that renders them attractive to solid-state battery researchers. The studies on LLZO electrolytes mainly focused on elemental doping, sintered second phase,[85] and optimized ceramic sintering process and mechanism,[86-88] and have laid an excellent foundation for their practical applications. In the presence of water, the lithium in LLZO electrolytes reacts with the hydrogen ions in water; this causes the surface of the electrolyte to lose its lithium-ion conductivity. Furthermore, lithium hydroxide, the reaction product, further reacts with CO_2 in the air to form inert lithium carbonate, which is not conducive to the interface modification of solid-state batteries.[89]

Sulfide electrolytes can be considered an extension of oxide solid electrolytes. Oxygen and sulfur are homologues; however, the ionic radius of sulfur is larger than that of oxygen, which facilitates the expansion of the ion channel size inside the lattice. In addition, because the relatively weak electronegativity of sulfur weakens the binding forces on lithium ions, the mobility of lithium ions in sulfide electrolytes is unrestricted. Similarly, the weak bonding forces within the lattice render sulfide electrolytes soft and facilitate their processing. Currently, the main types of sulfide electrolytes are phosphorus-sulfur (thio-super ionic conductor thio-LISICON) and silver germanite sulfide (argyrodite-type) electrolytes.[90] Li_3PS_4 and $Li_7P_3S_{11}$ were first reported by Tachez et al.[91] and Yamane et al.,[92] respectively. The room-temperature ionic conductivity of $Li_7P_3S_{11}$ can reach 3.2×10^{-3} S/cm. Sulfide electrolytes can be prepared

using solid-phase ball-milling[93] and liquid phase synthesis.[94, 95] In 2011, Kamaya et al.[96] reported a major breakthrough in sulfide electrolyte research by synthesizing the $Li_{10}GeP_2S_{12}$ electrolyte (Figure 1.10). The room-temperature ionic conductivity of $Li_{10}GeP_2S_{12}$ can reach 1.2×10^{-2} S/cm, which is much higher than those of liquid electrolytes. In 2016, Kato et al.[97] designed the $Li_{9.54}Si_{1.74}P_{1.44}S_{11.7}Cl_{0.3}$ sulfide electrolyte (Figure 1.11) with a very high room temperature ionic conductivity (2.5×10^{-2} S/cm) and the $Li_{9.6}P_3S_{12}$ sulfide electrolyte, which is stable in the presence of lithium metal. The ionic conductivity and mechanical strength of sulfide electrolytes are higher and lower, respectively, than those of oxide electrolytes, which helps to achieve good interfacial contact. However, sulfide electrolytes are extremely sensitive to water. Furthermore the raw materials required to prepare sulfide electrolytes are expensive and preparation conditions are very strict and include an inert atmosphere. Therefore, the process cost of sulfide electrolytes is high; furthermore, it is currently difficult to produce and use sulfide electrolytes on a large-scale.

1.5.3   Anode materials for all-solid-state lithium−sulfur batteries

The most commonly used anode materials for sulfide solid-state lithium–sulfur batteries include lithium metal, lithium alloys, and graphite. Lithium metal, which presents a very high theoretical capacity of 3860 mAh/g and the lowest chemical potential, is an ideal anode material. However, because lithium metal is very active, the formation of lithium dendrites at the anode is likely to affect battery performance. Numerous studies on liquid battery systems have focused on the modification of the lithium metal anode; however, researchers have not completely solved the safety of lithium anodes yet. The chemical stability at the lithium metal anode–solid electrolyte interface is relatively low, and side reactions occur very easily. However, this problem

can be solved by doping the solid electrolyte to improve stability at the interface. For example, doping P_2O_5 in the $Li_2S–P_2S_5$ solid electrolyte greatly improved the electrochemical stability at the interface,[98] and therefore, improved the electrochemical performance of the battery. Sun et al.[99] reported that oxygen atom doping in $Li_{10}GeP_2S_{12}$ increased the ionic conductivity of the electrolyte and improved the chemical and electrochemical stability of the electrolyte. Kato et al.[100] coated a gold film at the lithium metal–solid electrolyte interface (Figure 1.12), and that improved interfacial stability and the utilization of lithium metal.

Lithium alloys are common anode materials for sulfide all-solid-state lithium–sulfur batteries. Because of the instability at the lithium metal–solid electrolyte interface, lithium alloys, such as Li–In,[101] Li–Al,[102] and Li–Si,[103] are often used to replace lithium metal and improve interface stability. The most commonly used lithium alloys are Li–In alloys, because in these alloys, lithium voltage is constant and stable[104] (0.62 V vs. Li/Li^+). Nagata et al.[105] used a Li–In alloy and sulfur as the anode and cathode, respectively, to construct a cell, which presented a discharge capacity of 1550 mAh/g during the first discharge cycle and excellent cycling performance during subsequent cycles. The use of lithium alloys as anodes for solid-state batteries is a very effective method for hindering the formation of lithium dendrites and improve stability at the anode–electrolyte interface.

Graphite anodes have also been successfully used for commercial liquid batteries, owing to their very low lithium de-embedding voltage plateau (0.2 V vs. Li/Li^+) and high theoretical capacity (372 mAh/g).[106, 107] Graphite is unstable in the presence of some sulfide electrolytes and the can easily undergo reduction, which results in large irreversible capacities. Takada et al.[108] added LiI into the electrolyte of a lithium–sulfur battery and formed a LiI-rich SEI film between the lithium metal anode and electrolyte.

This improved interfacial stability, and LiCoO$_2$ matching preparation of the whole battery shows excellent reversible charge–discharge performance to improve the cycle stability of the entire battery.

1.6   Objective

The rapid development of the electric vehicle industry puts forward higher and higher requirements for the energy density of batteries, and the development of high specific energy cathode materials is the key to improving battery energy density. Lithium-sulfur batteries have received extensive attention from researchers due to their ultra-high theoretical specific capacity and specific energy.

However, the reaction mechanism of sulfur cathode in lithium-sulfur battery is still unclear. Especially, how the polysulfide changes during discharge process at different type of electrolyte system and how size of carbon-support cathode influence the reaction pathway is still unclear, this research used XAFS measurements to reveal the reaction of sulfur cathode in different system, and our research will helpful for researcher to know how the reaction pathway change in different electrolyte and help them to control the reaction pathway by modify electrolyte in both liquid electrolyte and solid-state electrolyte.

Meanwhile, in all-solid-state lithium sulfur battery, the insulating sulfur and lithium sulfide also limit the utilization of active materials and energy density of battery. This research trying to synthesize the novel cathode materials with high electronic and ionic conductivity to improve the performance of all-solid-sate lithium sulfur battery, and the reaction mechanism were also studied by XAFS measurements, these works may helpful for provide the novel strategy and method for developing the newly high energy density all-solid-state battery.

1.7   Thesis outline

This thesis consists of six chapters, which report the reaction mechanisms of cathode materials for liquid and all-solid-state lithium sulfur batteries during charge–discharge and provide new insight into the design of cathode materials for lithium–sulfur batteries.

Chapter 1 briefly outlines the research background and fundamental principle of lithium-ion and lithium–sulfur batteries. Liquid and all-solid-state lithium sulfur batteries are introduced, and the cathode materials, electrolytes, and anode materials of the two types of batteries are discussed in detail.

Chapter 2 describes the changes in electronic structure of sulfur cathodes in conventional liquid, concentrated liquid, and solid-state electrolytes observed using X-ray absorption spectroscopy (XAS). In particular, the *operando* XAS technique was used to examine the changes in electronic structure of sulfur cathodes in conventional and concentrated liquid electrolytes. Moreover, the formation of and changes in polysulfide species during the first discharge process in a sulfur-based all-solid-state-battery were investigated using XAS for the first time.

Chapter 3 focuses on clarifying the reaction mechanism of microporous carbon-supported sulfur cathodes using *operando* soft XAS. The size of the sulfur fragments in microporous carbon supports was smaller than that of sulfur in conventional cathodes. The changes in polysulfides species during discharge were investigated. It was determined that the narrow pores of microporous carbon prevented the dissolution of polysulfides and affected the reaction mechanism of sulfur cathodes.

Chapter 4 addresses the development of novel $Li_2S–V_2S_3–LiI$-based electrode active materials with excellent electronic and ionic conductivity. All-solid-state lithium sulfur battery featuring Li_2S, V_2S_3, and LiI composite electrode layers were fabricated and

characterized to demonstrate their advantages as all-solid-state lithium sulfur battery cathode materials with high electronic and ionic conductivity.

Chapter 5 describes the successful synthesis of Li_3CuS_2 as a new type of all solid-state lithium sulfur battery cathode material. Furthermore, XAS was used to elucidate the reaction mechanism of Li_3CuS_2 during charging. These findings could facilitate the design of new types of cathode materials for all-solid-state lithium sulfur batteries.
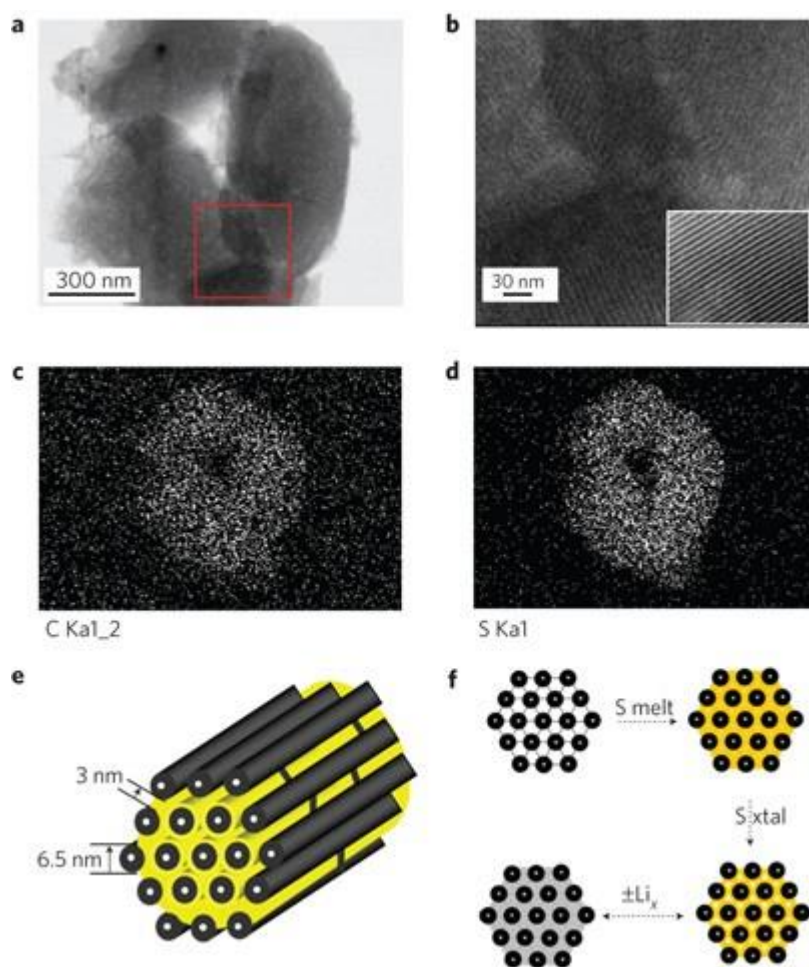
Chapter 6 presents the conclusions of this study and future prospects for lithium–sulfur batteries.
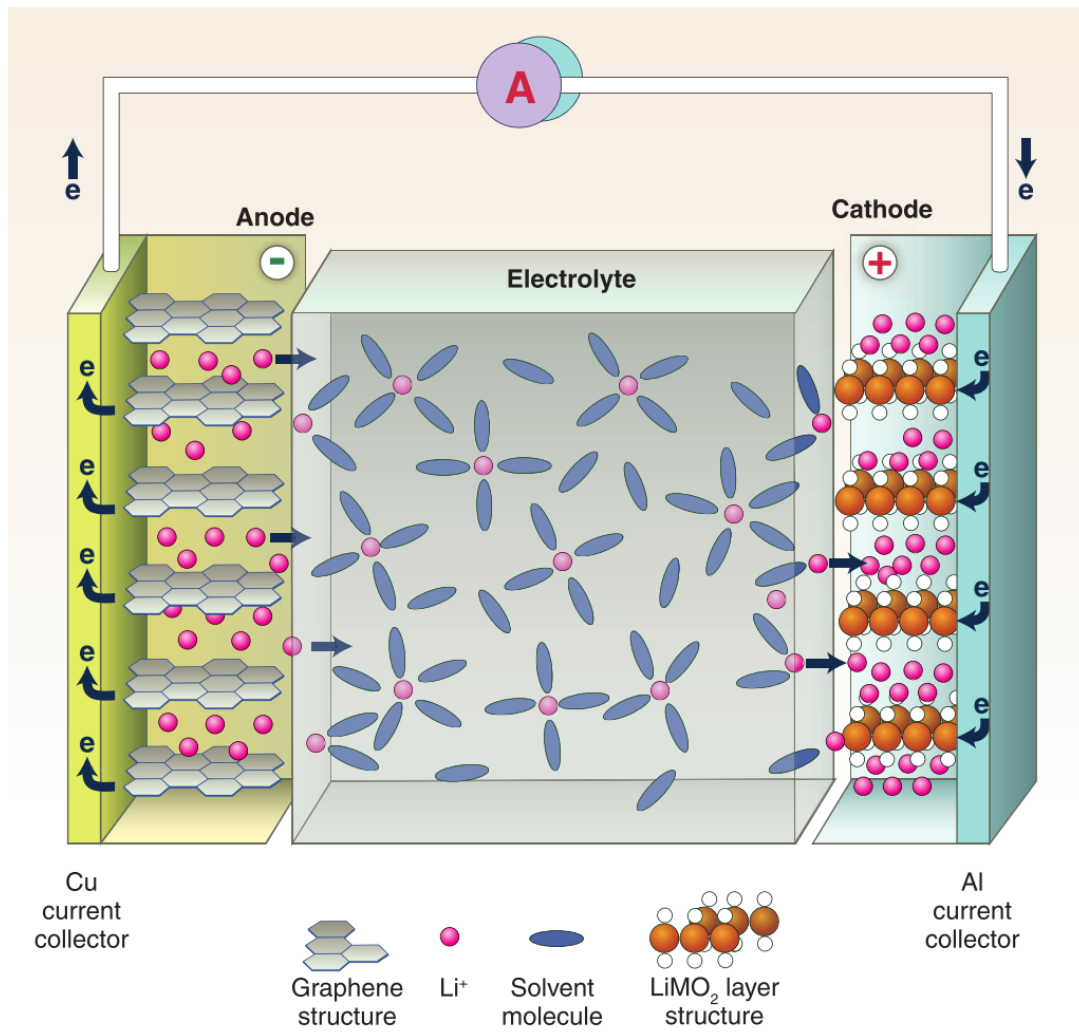
Figure 1.1. Schematic of a lithium ion battery.
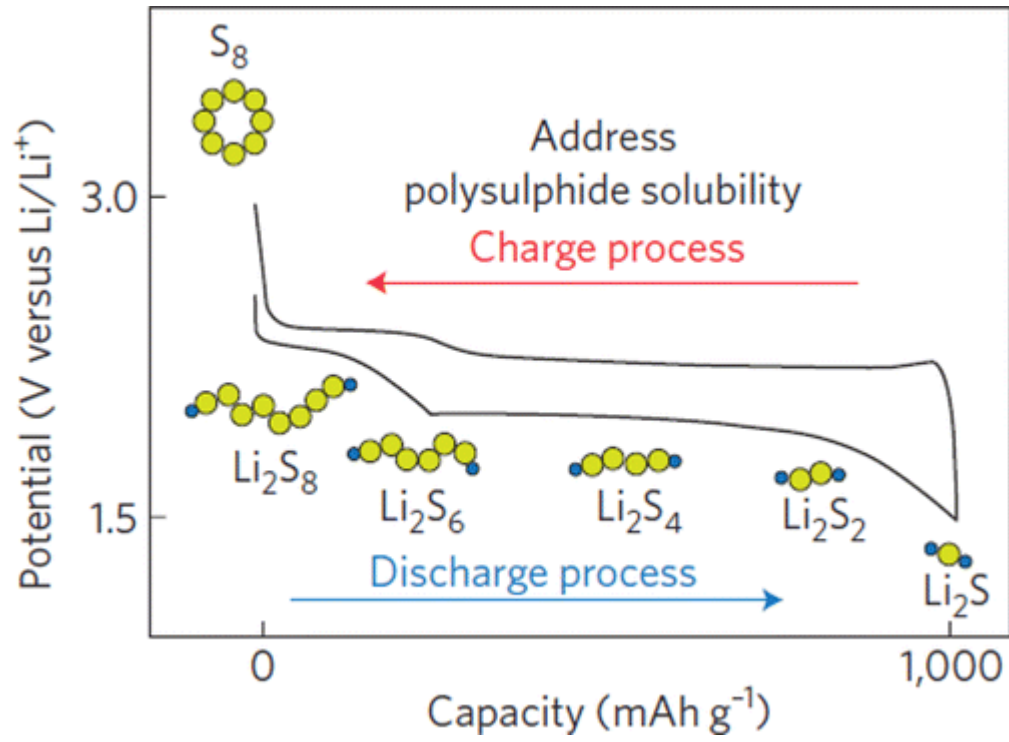
Figure 1.2. Voltage profiles of a Li–S cell.

Figure 1.3. TEM image and elemental maps of a CMK-3/S-155 composite particle and schematic diagrams of the structure and redox processes.
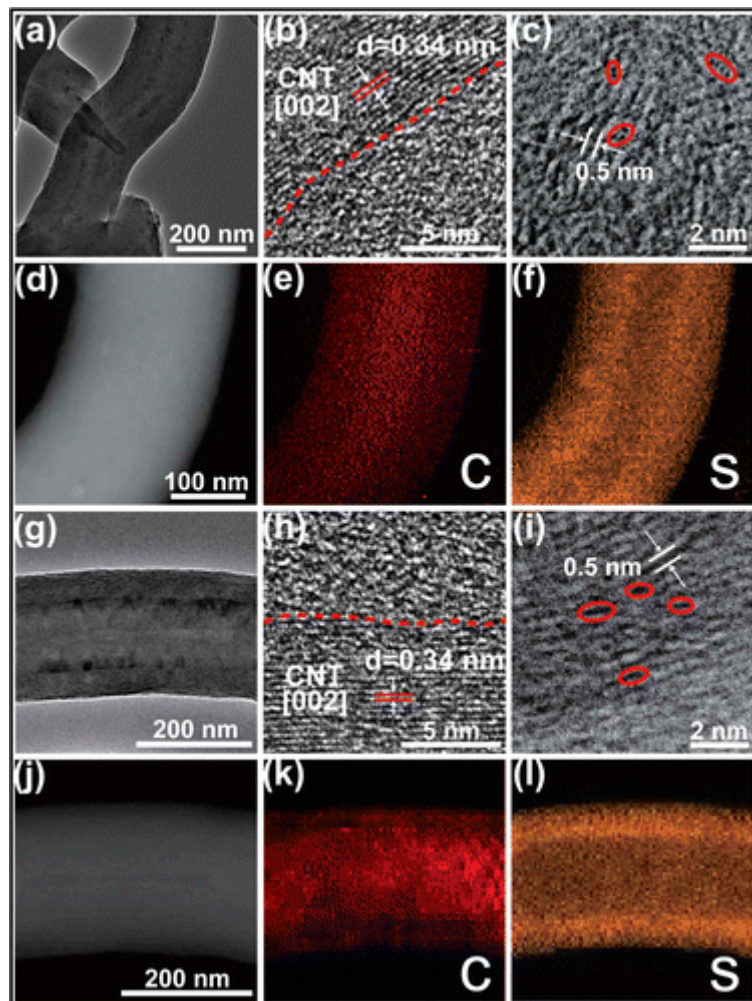
Figure 1.4. Structural characterization of S/(CNT@MPC) before and after 200 cycles at 0.1 C.
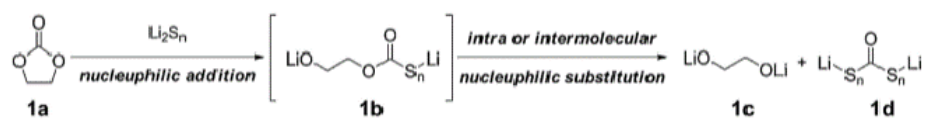
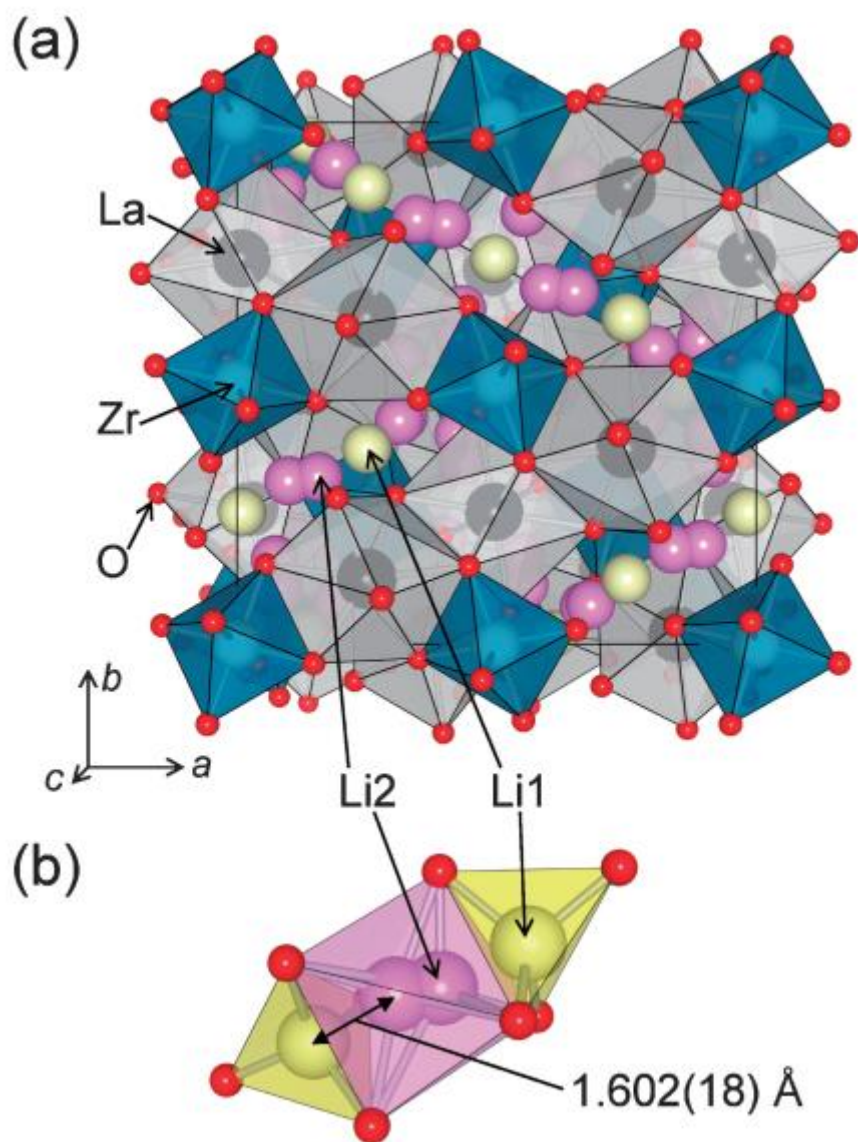**Figure 1.5.** Plausible mechanism for EC and EMC decomposition by polysulfide.
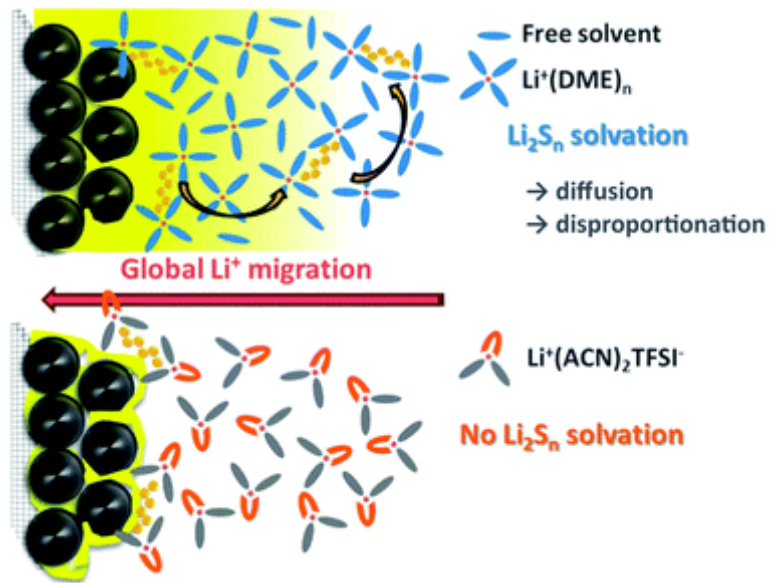
Figure 1.6. Concept of a nonsolvent for polysulphides in a Li–S battery.
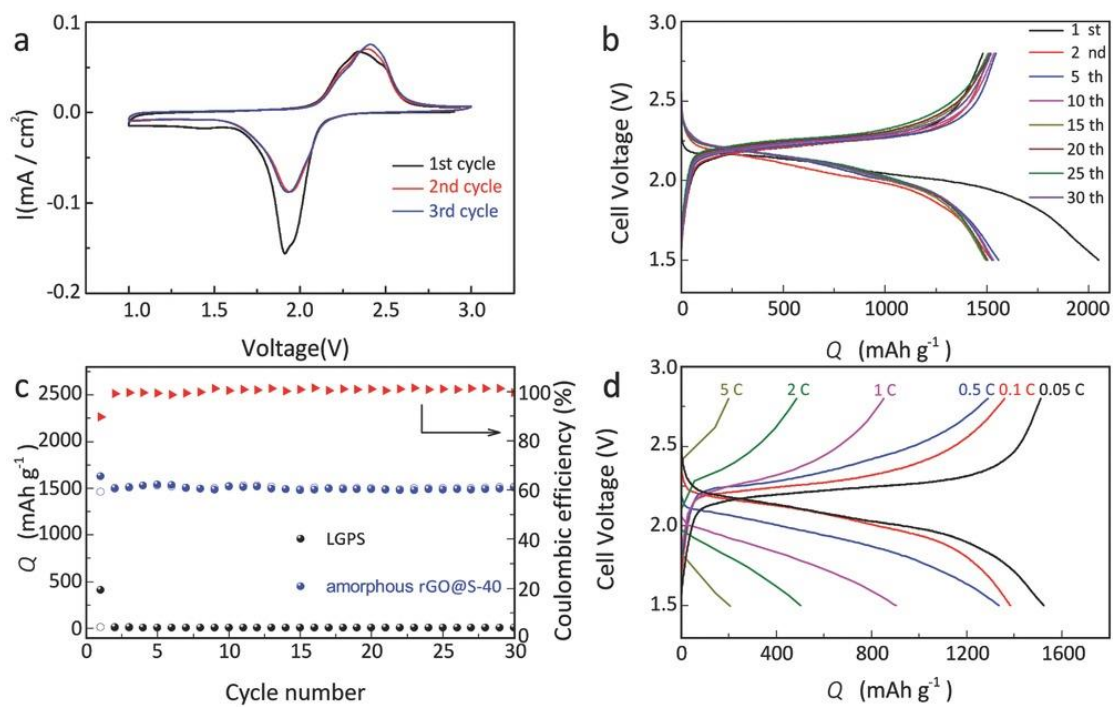
Figure 1.7. Cyclic voltammogram of the amorphous rGO@S-40 composite.
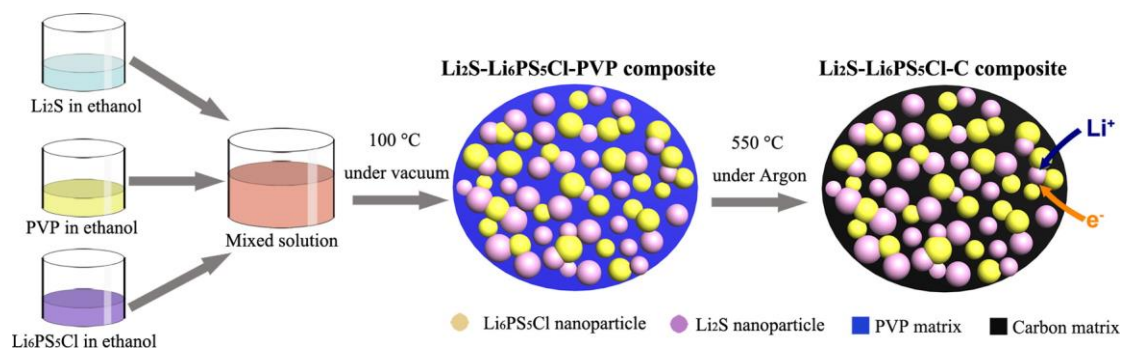
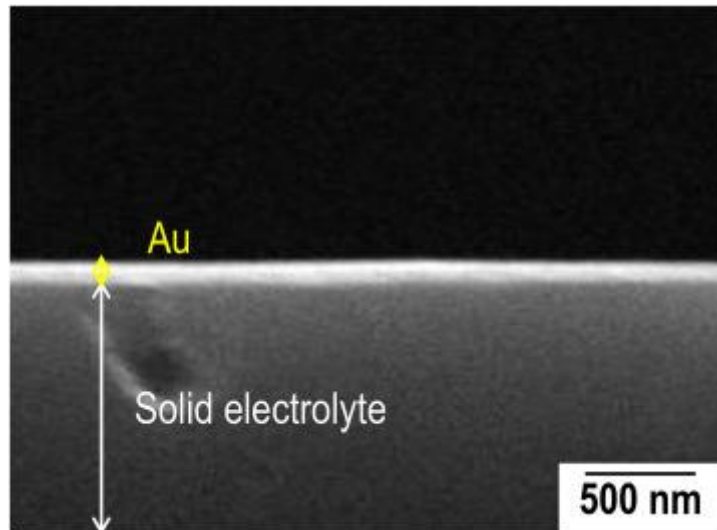**Figure 1.8.** Schematic illustration of the bottom-up synthesis of the mixed conducting Li$_2$S nanocomposite.

Figure 1.9. (a) Crystal structure of cubic $Li_7La_3Zr_2O_{12}$. (b) Coordination polyhedral around the Li1 and Li2 sites.
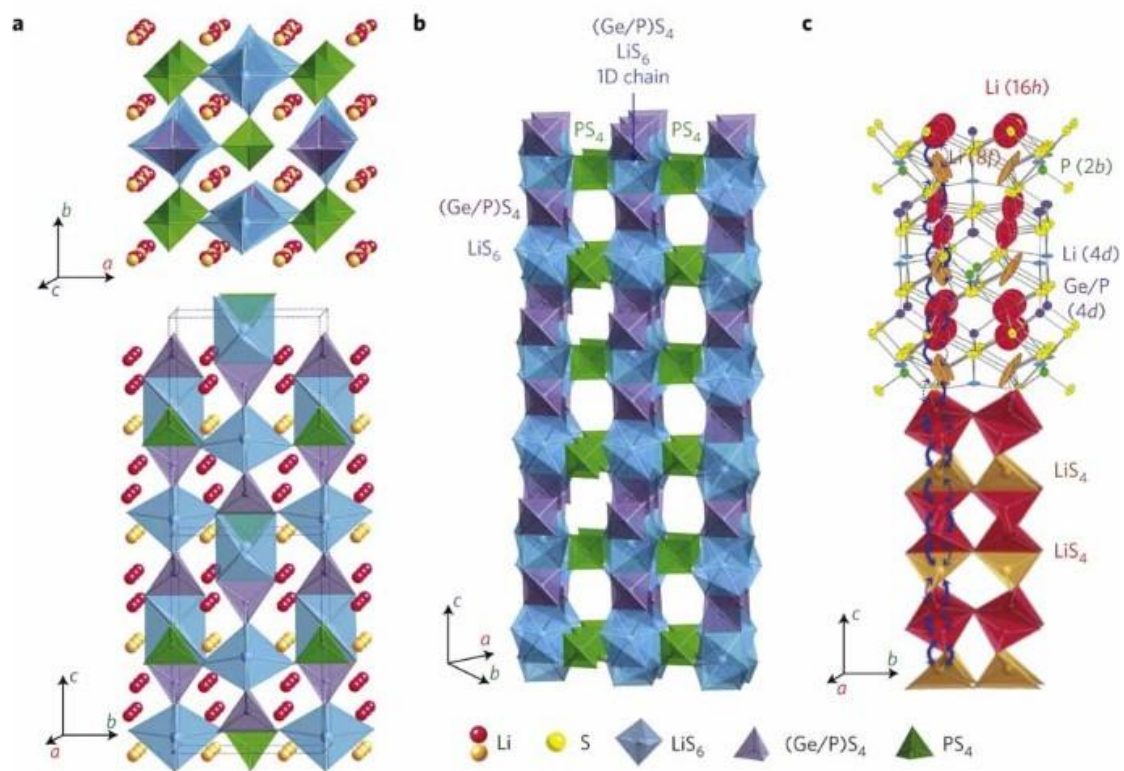
Figure 1.10. Crystal structure of $Li_{10}GeP_2S_{12}$.
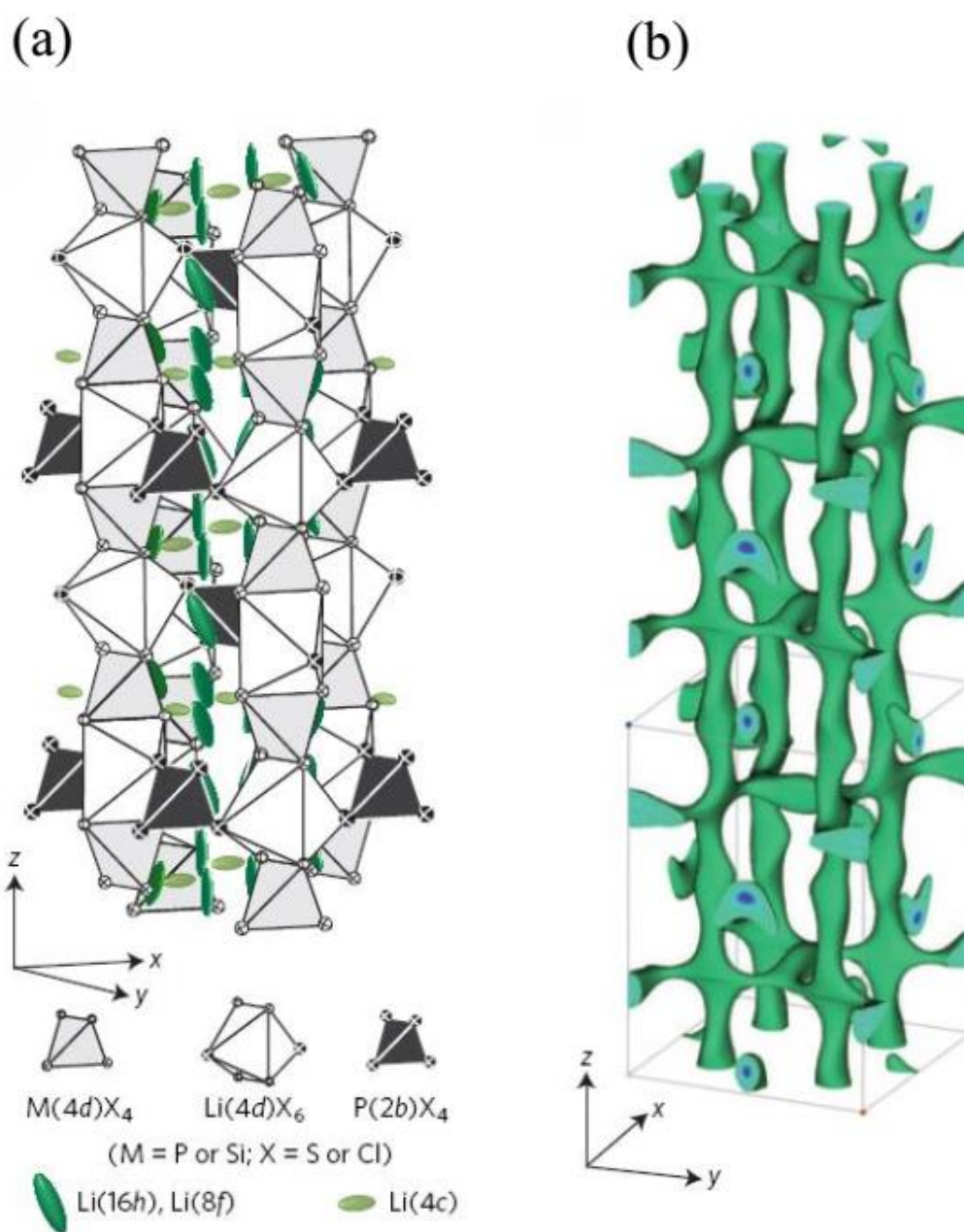
Figure 1.11. Crystal structure of $Li_{9.54}Si_{1.74}P_{1.44}S_{11.7}Cl_{0.3}$.

Figure 1.12. Cross-sectional SEM image of the interface between Au thin films and Li$_2$S-P$_2$S$_5$ solid electrolytes.

Reference

(1)   Bruce, P. G. Energy storage beyond the horizon: Rechargeable lithium batteries. *Solid State Ionics*. **2008**, *179*, 752-760.

(2)   Tarascon, J. M.; Armand, M. Issues and challenges facing rechargeable lithium batteries. *Nature*. **2001**, *414*, 359-367.

(3)   Yang, Z. G.; Zhang, J. L.; Kintner-Meyer, M. C. W.; Lu, X. C.; Choi, D. W.; Lemmon, J. P.; Liu, J. Electrochemical Energy Storage for Green Grid. *Chem. Rev.* **2011**, *111*, 3577-3613.

(4)   Scrosati, B.; Garche, J. Lithium batteries: Status, prospects and future. *J. Power Sources*. **2010**, *195*, 2419-2430.

(5)   Armand, M.; Tarascon, J. M. Building better batteries. *Nature*. **2008**, *451*, 652-657.

(6)   Goodenough, J. B.; Kim, Y. Challenges for Rechargeable Li Batteries. *Chem. Mater.* **2010**, *22*, 587-603.

(7)   Scrosati, B.; Hassoun, J.; Sun, Y. K. Lithium-ion batteries. A look into the future. *Energy Environ. Sci*. **2011**, *4*, 3287-3295.

(8)   Whittingham, M. S. Lithium batteries and cathode materials. *Chem. Rev.* **2004**, *104*, 4271-4301.

(9)   Bruce, P. G.; Freunberger, S. A.; Hardwick, L. J.; Tarascon, J. M. Li-O_2 and Li-S batteries with high energy storage. *Nat. Mater.* **2012**, *11*, 19-29.

(10)   Kang, K. S.; Meng, Y. S.; Breger, J.; Grey, C. P.; Ceder, G. Electrodes with high power and high capacity for rechargeable lithium batteries. *Science*. **2006**, *311*, 977-980.

(11)   Etacheri, V.; Marom, R.; Elazari, R.; Salitra, G.; Aurbach, D. Challenges in the development of advanced Li-ion batteries: a review. *Energy Environ. Sci*. **2011**, *4*, 3243-3262.

(12)   Dunn, B.; Kamath, H.; Tarascon, J. M. Electrical Energy Storage for the Grid: A Battery of Choices. *Science*. **2011**, *334*, 928-935.

(13)   Cho, Y.; Eom, J.; Cho, J. High Performance $LiCoO_2$ Cathode Materials at 60 ºC for Lithium Secondary Batteries Prepared by the Facile Nanoscale Dry-Coating Method. *J. Electrochem. Soc.* **2010**, *157*, A617-A624.

(14)   Thackeray, M. M.; Johnson, P. J.; Depicciotto, L. A.; Bruce, P. G.; Goodenough, J. B. Electrochemical Extraction of Lithium from $LiMn_2O_4$. *Mater. Res. Bull.* **1984**, *19*, 179-187.

(15)   Kim, D. K.; Muralidharan, P.; Lee, H. W.; Ruffo, R.; Yang, Y.; Chan, C. K.; Peng, H.; Huggins, R. A.; Cui, Y. Spinel $LiMn_2O_4$ Nanorods as Lithium Ion Battery Cathodes. *Nano Lett.* **2008**, *8*, 3948-3952.

(16)   Yamada, A.; Chung, S. C.; Hinokuma, K. Optimized $LiFePO_4$ for lithium

battery cathodes. *J. Electrochem. Soc.* **2001**, *148*, A224-A229.

(17)   Padhi, A. K.; Nanjundaswamy, K. S.; Goodenough, J. B. Phospho-olivines as positive-electrode materials for rechargeable lithium batteries. *J. Electrochem. Soc.* **1997**, *144*, 1188-1194.

(18)   Yin, Y.-X.; Xin, S.; Guo, Y.-G.; Wan, L.-J. Lithium-sulfur batteries: electrochemistry, materials, and prospects. *Angew. Chem., Int. Ed.* **2013**, *52*, 13186-200.

(19)   Bruce, P. G.; Freunberger, S. A.; Hardwick, L. J.; Tarascon, J. M. Li-O$_2$ and Li-S batteries with high energy storage. *Nat. Mater.* **2011**, *11*, 19-29.

(20)   Seh, Z. W.; Sun, Y.; Zhang, Q.; Cui, Y. Designing high-energy lithium-sulfur batteries. *Chem. Soc. Rev.* **2016**, *45*, 5605-5634.

(21)   Pang, Q.; Liang, X.; Kwok, C. Y.; Nazar, L. F. Advances in lithium–sulfur batteries based on multifunctional cathodes and electrolytes. *Nat. Energy.* **2016**, *1*, 16132.

(22)   Ellis, B. L.; Lee, K. T.; Nazar, L. F. Positive Electrode Materials for Li-Ion and Li-Batteries†. *Chem. Mater.* **2010**, *22*, 691-714.

(23)   Manthiram, A.; Fu, Y.; Chung, S.-H.; Zu, C.; Su, Y.-S. Rechargeable lithium-sulfur batteries. *Chem. Rev.* **2014**, *114*, 11751-11787.

(24)   Evers, S.; Nazar, L. F. New Approaches for High Energy Density Lithium-Sulfur Battery Cathodes. *Acc. Chem. Res.* **2013**, *46*, 1135-1143.

(25)   Manthiram, A.; Fu, Y. Z.; Chung, S. H.; Zu, C. X.; Su, Y. S. Rechargeable Lithium-Sulfur Batteries. *Chem. Rev.* **2014**, *114*, 11751-11787.

(26)   Yin, Y. X.; Xin, S.; Guo, Y. G.; Wan, L. J. Lithium-Sulfur Batteries: Electrochemistry, Materials, and Prospects. *Angew. Chem., Int. Ed.* **2013**, *52*, 13186-13200.

(27)   Ji, X. L.; Nazar, L. F. Advances in Li-S batteries. *J. Mater. Chem.* **2010**, *20*, 9821-9826.

(28)   Manthiram, A.; Fu, Y. Z.; Su, Y. S. Challenges and Prospects of Lithium-Sulfur Batteries. *Acc. Chem. Res.* **2013**, *46*, 1125-1134.

(29)   Mikhaylik, Y. V.; Akridge, J. R. Polysulfide shuttle study in the Li/S battery system. *J. Electrochem. Soc.* **2004**, *151*, A1969-A1976.

(30)   Ji, X.; Lee, K. T.; Nazar, L. F. A highly ordered nanostructured carbon-sulphur cathode for lithium-sulphur batteries. *Nat. Mater.* **2009**, *8*, 500-6.

(31)   Xin, S.; Gu, L.; Zhao, N. H.; Yin, Y. X.; Zhou, L. J.; Guo, Y. G.; Wan, L. J. Smaller Sulfur Molecules Promise Better Lithium-Sulfur Batteries. *J. Am. Chem. Soc.* **2012**, *134*, 18510-18513.

(32)   Zhao, Q.; Zhu, Q. H.; Miao, J. W.; Guan, Z. X.; Liu, H.; Chen, R. J.; An, Y. B.; Wu, F.; Xu, B. Three-Dimensional Carbon Current Collector Promises Small

Sulfur Molecule Cathode with High Areal Loading for Lithium-Sulfur Batteries. *ACS Appl. Mater. Interfaces*. **2018**, *10*, 10882-10889.

(33)   Han, J. K.; Li, Y.; Li, S. W.; Long, P.; Cao, C.; Cao, Y.; Wang, W. Z.; Feng, Y. Y.; Feng, W. A low cost ultra-microporous carbon scaffold with confined chain-like sulfur molecules as a superior cathode for lithium-sulfur batteries. *Sustainable Energy Fuels*. **2018**, *2*, 2187-2196.

(34)   Sun, L.; Wang, D. T.; Luo, Y. F.; Kong, W. B.; Wu, Y.; Zhang, L. N.; Jiang, K. L.; Li, Q. Q.; Zhang, Y. H.; Wang, J. P.; Fan, S. S. Sulfur Embedded in a Mesoporous Carbon Nanotube Network as a Binder-Free Electrode for High-Performance Lithium Sulfur Batteries. *ACS Nano*. **2016**, *10*, 1300-1308.

(35)   Kim, S.; Song, H.; Jeong, Y. Flexible catholyte@carbon nanotube film electrode for high-performance lithium sulfur battery. *Carbon*. **2017**, *113*, 371-378.

(36)   Li, M. Y.; Carter, R.; Douglas, A.; Oakes, L.; Pint, C. L. Sulfur Vapor-Infiltrated 3D Carbon Nanotube Foam for Binder-Free High Areal Capacity Lithium-Sulfur Battery Composite Cathodes. *ACS Nano*. **2017**, *11*, 4877-4884.

(37)   Zhou, G. M.; Wang, D. W.; Li, F.; Hou, P. X.; Yin, L. C.; Liu, C.; Lu, G. Q.; Gentle, I. R.; Cheng, H. M. A flexible nanostructured sulphur-carbon nanotube cathode with high rate performance for Li-S batteries. *Energy Environ. Sci*. **2012**, *5*, 8901-8906.

(38)   Yuan, Z.; Peng, H. J.; Huang, J. Q.; Liu, X. Y.; Wang, D. W.; Cheng, X. B.; Zhang, Q. Hierarchical Free-Standing Carbon-Nanotube Paper Electrodes with Ultrahigh Sulfur-Loading for Lithium-Sulfur Batteries. *Adv. Funct. Mater.* **2014**, *24*, 6105-6112.

(39)   Ahn, W.; Kim, K. B.; Jung, K. N.; Shin, K. H.; Jin, C. S. Synthesis and electrochemical properties of a sulfur-multi walled carbon nanotubes composite as a cathode material for lithium sulfur batteries. *J. Power Sources*. **2012**, *202*, 394-399.

(40)   Elazari, R.; Salitra, G.; Garsuch, A.; Panchenko, A.; Aurbach, D. Sulfur-Impregnated Activated Carbon Fiber Cloth as a Binder-Free Cathode for Rechargeable Li-S Batteries. *Adv. Mater.* **2011**, *23*, 5641-5644.

(41)   Han, S. C.; Song, M. S.; Lee, H.; Kim, H. S.; Ahn, H. J.; Lee, J. Y. Effect of multiwalled carbon nanotubes on electrochemical properties of lithium sulfur rechargeable batteries. *J. Electrochem. Soc.* **2003**, *150*, A889-A893.

(42)   Guo, J. C.; Xu, Y. H.; Wang, C. S. Sulfur-Impregnated Disordered Carbon Nanotubes Cathode for Lithium-Sulfur Batteries. *Nano Lett.* **2011**, *11*, 4288-4294.

(43)   Yim, T.; Park, M. S.; Yu, J. S.; Kim, K. J.; Im, K. Y.; Kim, J. H.; Jeong, G.; Jo, Y. N.; Woo, S. G.; Kang, K. S.; Lee, I.; Kim, Y. J. Effect of chemical reactivity

of polysulfide toward carbonate-based electrolyte on the electrochemical performance of Li-S batteries. *Electrochim. Acta*. **2013**, *107*, 454-460.

(44)   Wang, J. L.; He, Y. S.; Yang, J. Sulfur-Based Composite Cathode Materials for High-Energy Rechargeable Lithium Batteries. *Adv. Mater.* **2015**, *27*, 569-575.

(45)   Carbone, L.; Gobet, M.; Peng, J.; Devany, M.; Scrosati, B.; Greenbaum, S.; Hassoun, J. Comparative Study of Ether-Based Electrolytes for Application in Lithium-Sulfur Battery. *ACS Appl. Mater. Interfaces*. **2015**, *7*, 13859-13865.

(46)   Gu, S.; Qian, R.; Jin, J.; Wang, Q. S.; Guo, J.; Zhang, S. P.; Zhuo, S. J.; Wen, Z. Y. Suppressing the dissolution of polysulfides with cosolvent fluorinated diether towards high-performance lithium sulfur batteries. *Phys. Chem. Chem. Phys.* **2016**, *18*, 29293-29299.

(47)   Azimi, N.; Xue, Z.; Bloom, I.; Gordin, M. L.; Wang, D. H.; Daniel, T.; Takoudis, C.; Zhang, Z. C. Understanding the Effect of a Fluorinated Ether on the Performance of Lithium-Sulfur Batteries. *ACS Appl. Mater. Interfaces*. **2015**, *7*, 9169-9177.

(48)   Cuisinier, M.; Cabelguen, P. E.; Adams, B. D.; Garsuch, A.; Balasubramanian, M.; Nazar, L. F. Unique behaviour of nonsolvents for polysulphides in lithium-sulphur batteries. *Energy Environ. Sci*. **2014**, *7*, 2697-2705.

(49)   Suo, L. M.; Hu, Y. S.; Li, H.; Armand, M.; Chen, L. Q. A new class of Solvent-in-Salt electrolyte for high-energy rechargeable metallic lithium batteries. *Nat. Commun.* **2013**, *4*, 1481.

(50)   Hart, C. J.; Cuisinier, M.; Liang, X.; Kundu, D.; Garsuch, A.; Nazar, L. F. Rational design of sulphur host materials for Li-S batteries: correlating lithium polysulphide adsorptivity and self-discharge capacity loss. *Chem. Commun.* **2015**, *51*, 2308-2311.

(51)   Wang, L. N.; Liu, J. Y.; Yuan, S. Y.; Wang, Y. G.; Xia, Y. Y. To mitigate self-discharge of lithium-sulfur batteries by optimizing ionic liquid electrolytes. *Energy Environ. Sci.* **2016**, *9*, 224-231.

(52)   Cheng, X. B.; Zhang, R.; Zhao, C. Z.; Zhang, Q. Toward Safe Lithium Metal Anode in Rechargeable Batteries: A Review. *Chem. Rev.* **2017**, *117*, 10403-10473.

(53)   Kim, H.; Jeong, G.; Kim, Y. U.; Kim, J. H.; Park, C. M.; Sohn, H. J. Metallic anodes for next generation secondary batteries. *Chem. Soc. Rev.* **2013**, *42*, 9011-9034.

(54)   Cheng, X. B.; Zhang, R.; Zhao, C. Z.; Wei, F.; Zhang, J. G.; Zhang, Q. A Review of Solid Electrolyte Interphases on Lithium Metal Anode. *Adv. Sci*. **2016**, *3*, 1500213.

(55)   Zhang, X. Q.; Cheng, X. B.; Chen, X.; Yan, C.; Zhang, Q. Fluoroethylene

Carbonate Additives to Render Uniform Li Deposits in Lithium Metal Batteries. *Adv. Funct. Mater.* **2017**, *27*, 1605989.

(56) Cheng, X. B.; Hou, T. Z.; Zhang, R.; Peng, H. J.; Zhao, C. Z.; Huang, J. Q.; Zhang, Q. Dendrite-Free Lithium Deposition Induced by Uniformly Distributed Lithium Ions for Efficient Lithium Metal Batteries. *Adv. Mater.* **2016**, *28*, 2888-2895.

(57) Li, N. W.; Yin, Y. X.; Yang, C. P.; Guo, Y. G. An Artificial Solid Electrolyte Interphase Layer for Stable Lithium Metal Anodes. *Adv. Mater.* **2016**, *28*, 1853-1858.

(58) Ohta, N.; Takada, K.; Sakaguchi, I.; Zhang, L. Q.; Ma, R. Z.; Fukuda, K.; Osada, M.; Sasaki, T. LiNbO3-coated LiCoO2 as cathode material for all solid-state lithium secondary batteries. *Electrochem. Commun.* **2007**, *9*, 1486-1490.

(59) Sakuda, A.; Nakamoto, N.; Kitaura, H.; Hayashi, A.; Tadanaga, K.; Tatsumisago, M. All-solid-state lithium secondary batteries with metal-sulfide-coated LiCoO2 prepared by thermal decomposition of dithiocarbamato complexes. *J. Mater. Chem.* **2012**, *22*, 15247-15254.

(60) Woo, J. H.; Trevey, J. E.; Cavanagh, A. S.; Choi, Y. S.; Kim, S. C.; George, S. M.; Oh, K. H.; Lee, S. H. Nanoscale Interface Modification of LiCoO2 by Al2O3 Atomic Layer Deposition for Solid-State Li Batteries. *J. Electrochem. Soc.* **2012**, *159*, A1120-A1124.

(61) Ohzuku, T.; Makimura, Y. Layered lithium insertion material of LiCo$_{1/3}$Ni$_{1/3}$Mn$_{1/3}$O$_2$ for lithium-ion batteries. *Chem. Lett.* **2001**, 642-643.

(62) Kitaura, H.; Hayashi, A.; Tadanaga, K.; Tatsumisago, M. Electrochemical performance of all-solid-state lithium secondary batteries with Li-Ni-Co-Mn oxide positive electrodes. *Electrochim. Acta.* **2010**, *55*, 8821-8828.

(63) Iwasaki, S.; Hamanaka, T.; Yamakawa, T.; West, W. C.; Yamamoto, K.; Motoyama, M.; Hirayama, T.; Iriyama, Y. Preparation of thick-film LiNi1/3Co1/3Mn1/3O2 electrodes by aerosol deposition and its application to all-solid-state batteries. *J. Power Sources.* **2014**, *272*, 1086-1090.

(64) McCloskey, B. D. Attainable Gravimetric and Volumetric Energy Density of Li-S and Li Ion Battery Cells with Solid Separator-Protected Li Metal Anodes. *J. Phys. Chem. Lett.* **2015**, *6*, 4581-4588.

(65) Yue, J. P.; Yan, M.; Yin, Y. X.; Guo, Y. G. Progress of the Interface Design in All-Solid-State Li-S Batteries. *Adv. Funct. Mater.* **2018**, *28*, 1707533.

(66) Nagao, M.; Hayashi, A.; Tatsumisago, M. Electrochemical Performance of All-Solid-State Li/S Batteries with Sulfur-Based Composite Electrodes Prepared by Mechanical Milling at High Temperature. *Energy Technol.* **2013**, *1*, 186-192.

(67) Yao, X. Y.; Huang, N.; Han, F. D.; Zhang, Q.; Wan, H. L.; Mwizerwa, J. P.;

Wang, C. S.; Xu, X. X. High-Performance All-Solid-State Lithium-Sulfur Batteries Enabled by Amorphous Sulfur-Coated Reduced Graphene Oxide Cathodes. *Adv. Energy Mater*. **2017**, *7*, 1602923.

(68) Han, F. D.; Yue, J.; Fan, X. L.; Gao, T.; Luo, C.; Ma, Z. H.; Suo, L. M.; Wang, C. S. High-Performance All-Solid-State Lithium-Sulfur Battery Enabled by a Mixed-Conductive Li_2S Nanocomposite. *Nano Lett.* **2016**, *16*, 4521-4527.

(69) Nagao, M.; Hayashi, A.; Tatsumisago, M. High-capacity Li2S-nanocarbon composite electrode for all-solid-state rechargeable lithium batteries. *J. Mater. Chem.* **2012**, *22*, 10015-10020.

(70) Matsuyama, T.; Hayashi, A.; Ozaki, T.; Mori, S.; Tatsumisago, M. Electrochemical properties of all-solid-state lithium batteries with amorphous MoS3 electrodes prepared by mechanical milling. *J. Mater. Chem. A*. **2015**, *3*, 14142-14147.

(71) Shin, B. R.; Nam, Y. J.; Kim, J. W.; Lee, Y. G.; Jung, Y. S. Interfacial Architecture for Extra Li^+ Storage in All-Solid-State Lithium Batteries. *Sci. Rep*. **2014**, *4*, 5572.

(72) Chen, M. H.; Yin, X. S.; Reddy, M. V.; Adams, S. All-solid-state $MoS_2/Li_6PS_5Br/In$-Li batteries as a novel type of Li/S battery. *J. Mater. Chem. A*. **2015**, *3*, 10698-10702.

(73) Yao, X. Y.; Liu, D.; Wang, C. S.; Long, P.; Peng, G.; Hu, Y. S.; Li, H.; Chen, L. Q.; Xu, X. X. High-Energy All-Solid-State Lithium Batteries with Ultralong Cycle Life. *Nano Lett.* **2016**, *16*, 7148-7154.

(74) Du, H. P.; Li, S. Z.; Qu, H. T.; Lu, B. Y.; Wang, X. G.; Chai, J. C.; Zhang, H. R.; Ma, J.; Zhang, Z. H.; Cui, G. L. Stable cycling of lithium-sulfur battery enabled by a reliable gel polymer electrolyte rich in ester groups. *J. Membr. Sci.* **2018**, *550*, 399-406.

(75) Gu, S.; Sun, C.; Xu, D.; Lu, Y.; Jin, J.; Wen, Z. Recent Progress in Liquid Electrolyte-Based Li–S Batteries: Shuttle Problem and Solutions. *Electrochem. Energy Rev*. **2018**, *1*, 599-624.

(76) Qu, H. T.; Zhang, J. J.; Du, A. B.; Chen, B. B.; Chai, J. C.; Xue, N.; Wang, L. L.; Qiao, L. X.; Wang, C.; Zang, X.; Yang, J. F.; Wang, X. G.; Cui, G. L. Multifunctional Sandwich-Structured Electrolyte for High-Performance Lithium-Sulfur Batteries. *Adv. Sci*. **2018**, *5*, 1700503.

(77) Meesala, Y.; Jena, A.; Chang, H.; Liu, R. S. Recent Advancements in Li-Ion Conductors for All-Solid-State Li-Ion Batteries. *ACS Energy Lett*. **2017**, *2*, 2734-2751.

(78) Bachman, J. C.; Muy, S.; Grimaud, A.; Chang, H. H.; Pour, N.; Lux, S. F.; Paschos, O.; Maglia, F.; Lupart, S.; Lamp, P.; Giordano, L.; Shao-Horn, Y.

Inorganic Solid-State Electrolytes for Lithium Batteries: Mechanisms and Properties Governing Ion Conduction. *Chem. Rev.* **2016**, *116*, 140-162.

(79) Thangadurai, V.; Weppner, W. Recent progress in solid oxide and lithium ion conducting electrolytes research. *Ionics*. **2006**, *12*, 81-92.

(80) Liu, Y. J.; Li, C.; Li, B. J.; Song, H. C.; Cheng, Z.; Chen, M. R.; He, P.; Zhou, H. S. Germanium Thin Film Protected Lithium Aluminum Germanium Phosphate for Solid-State Li Batteries. *Adv. Energy Mater*. **2018**, *8*, 1702374.

(81) Lu, Z. H.; Chen, C.; Baiyee, Z. M.; Chen, X.; Niu, C. M.; Ciucci, F. Defect chemistry and lithium transport in Li_3OCl anti-perovskite superionic conductors. *Phys. Chem. Chem. Phys.* **2015**, *17*, 32547-32555.

(82) Awaka, J.; Takashima, A.; Kataoka, K.; Kijima, N.; Idemoto, Y.; Akimoto, J. Crystal Structure of Fast Lithium-ion-conducting Cubic $Li_7La_3Zr_2O_{12}$. *Chem. Lett.* **2011**, *40*, 60-62.

(83) Thangadurai, V.; Kaack, H.; Weppner, W. J. F. Novel fast lithium ion conduction in garnet-type $Li_5La_3M_2O_{12}$ (M = Nb, Ta). *J. Am. Ceram. Soc.* **2003**, *86*, 437-440.

(84) Murugan, R.; Thangadurai, V.; Weppner, W. Fast lithium ion conduction in garnet-type $Li_7La_3Zr_2O_{12}$. *Angew. Chem., Int. Ed.* **2007**, *46*, 7778-7781.

(85) Huang, X.; Liu, C.; Lu, Y.; Xiu, T. P.; Jin, J.; Badding, M. E.; Wen, Z. Y. A Li-Garnet composite ceramic electrolyte and its solid-state Li-S battery. *J. Power Sources*. **2018**, *382*, 190-197.

(86) Huang, X.; Lu, Y.; Tin, J.; Gu, S.; Xiu, T. P.; Song, Z.; Badding, M. E.; Wen, Z. Y. Method Using Water-Based Solvent to Prepare $Li_7La_3Zr_2O_{12}$ Solid Electrolytes. *ACS Appl. Mater. Interfaces*. **2018**, *10*, 17147-17155.

(87) Huang, X.; Lu, Y.; Guo, H. J.; Song, Z.; Xiu, T. P.; Badding, M. E.; Wen, Z. Y. None-Mother-Powder Method to Prepare Dense Li-Garnet Solid Electrolytes with High Critical Current Density. *ACS Appl. Energy Mater*. **2018**, *1*, 5355-5365.

(88) Huang, X.; Lu, Y.; Song, Z.; Rui, K.; Wang, Q. S.; Xiu, T. P.; Badding, M. E.; Wen, Z. Y. Manipulating Li_2O atmosphere for sintering dense $Li_7La_3Zr_2O_{12}$ solid electrolyte. *Energy Storage Mater*. **2019**, *22*, 207-217.

(89) Truong, L.; Thangadurai, V. First Total H^+/Li^+ Ion Exchange in Garnet-Type $Li_5La_3Nb_2O_{12}$ Using Organic Acids and Studies on the Effect of Li Stuffing. *Inorg. Chem.* **2012**, *51*, 1222-1224.

(90) Chen, S. J.; Xie, D. J.; Liu, G. Z.; Mwizerwa, J. P.; Zhang, Q.; Zhao, Y. R.; Xu, X. X.; Yao, X. Y. Sulfide solid electrolytes for all-solid-state lithium batteries: Structure, conductivity, stability and application. *Energy Storage Mater*. **2018**, *14*, 58-74.

(91)   Tachez, M.; Malugani, J. P.; Mercier, R.; Robert, G. Ionic-Conductivity of and Phase-Transition in Lithium Thiophosphate Li_3PS_4. *Solid State Ionics*. **1984**, *14*, 181-185.

(92)   Yamane, H.; Shibata, M.; Shimane, Y.; Junke, T.; Seino, Y.; Adams, S.; Minami, K.; Hayashi, A.; Tatsumisago, M. Crystal structure of a superionic conductor, $Li_7P_3S_{11}$. *Solid State Ionics*. **2007**, *178*, 1163-1167.

(93)   Kudu, O. U.; Famprikis, T.; Fleutot, B.; Braida, M. D.; Le Mercier, T.; Islam, M. S.; Masquelier, C. A review of structural properties and synthesis methods of solid electrolyte materials in the Li_2S - P_2S_5 binary system. *J. Power Sources*. **2018**, *407*, 31-43.

(94)   Ito, S.; Nakakita, M.; Aihara, Y.; Uehara, T.; Machida, N. A synthesis of crystalline $Li_7P_3S_{11}$ solid electrolyte from 1,2-dimethoxyethane solvent. *J. Power Sources*. **2014**, *271*, 342-345.

(95)   Liu, Z. C.; Fu, W. J.; Payzant, E. A.; Yu, X.; Wu, Z. L.; Dudney, N. J.; Kiggans, J.; Hong, K. L.; Rondinone, A. J.; Liang, C. D. Anomalous High Ionic Conductivity of Nanoporous beta-Li_3PS_4. *J. Am. Chem. Soc.* **2013**, *135*, 975-978.

(96)   Kamaya, N.; Homma, K.; Yamakawa, Y.; Hirayama, M.; Kanno, R.; Yonemura, M.; Kamiyama, T.; Kato, Y.; Hama, S.; Kawamoto, K.; Mitsui, A. A lithium superionic conductor. *Nat. Mater.* **2011**, *10*, 682-686.

(97)   Kato, Y.; Hori, S.; Saito, T.; Suzuki, K.; Hirayama, M.; Mitsui, A.; Yonemura, M.; Iba, H.; Kanno, R. High-power all-solid-state batteries using sulfide superionic conductors. *Nat. Energy*. **2016**, *1*, 16030.

(98)   Tao, Y. C.; Chen, S. J.; Liu, D.; Peng, G.; Yao, X. Y.; Xu, X. X. Lithium Superionic Conducting Oxysulfide Solid Electrolyte with Excellent Stability against Lithium Metal for All-Solid-State Cells. *J. Electrochem. Soc.* **2016**, *163*, A96-A101.

(99)   Sun, Y. L.; Suzuki, K.; Hara, K.; Hori, S.; Yano, T.; Hara, M.; Hirayama, M.; Kanno, R. Oxygen substitution effects in $Li_{10}GeP_2S_{12}$ solid electrolyte. *J. Power Sources*. **2016**, *324*, 798-803.

(100)   Kato, A.; Hayashi, A.; Tatsumisago, M. Enhancing utilization of lithium metal electrodes in all-solid-state batteries by interface modification with gold thin films. *J. Power Sources*. **2016**, *309*, 27-32.

(101)   Nagata, H.; Chikusa, Y. Activation of sulfur active material in an all-solid-state lithium-sulfur battery. *J. Power Sources*. **2014**, *263*, 141-144.

(102)   Nagao, M.; Imade, Y.; Narisawa, H.; Kobayashi, T.; Watanabe, R.; Yokoi, T.; Tatsumi, T.; Kanno, R. All-solid-state Li-sulfur batteries with mesoporous electrode and thio-LISICON solid electrolyte. *J. Power Sources*. **2013**, *222*,

237-242.

(103) Kinoshita, S.; Okuda, K.; Machida, N.; Naito, M.; Sigematsu, T. All-solid-state lithium battery with sulfur/carbon composites as positive electrode materials. *Solid State Ionics*. **2014**, *256*, 97-102.

(104) Takada, K.; Aotani, N.; Iwamoto, K.; Kondo, S. Solid state lithium battery with oxysulfide glass. *Solid State Ionics*. **1996**, *86-8*, 877-882.

(105) Nagata, H.; Chikusa, Y. All-Solid-State Lithium-Sulfur Battery with High Energy and Power Densities at the Cell Level. *Energy Technol*. **2016**, *4*, 484-489.

(106) Takeuchi, T.; Kageyama, H.; Nakanishi, K.; Ohta, T.; Sakuda, A.; Sakaebe, H.; Kobayashi, H.; Tatsumi, K.; Ogumi, Z. Rapid Preparation of $Li_2S-P_2S_5$ Solid Electrolyte and Its Application for Graphite/Li_2S All-Solid-State Lithium Secondary Battery. *Ecs Electrochem. Lett*. **2014**, *3*, A31-A35.

(107) Takeuchi, T.; Kageyama, H.; Nakanishi, K.; Ohta, T.; Sakuda, A.; Sakai, T.; Kobayashi, H.; Sakaebe, H.; Tatsumi, K.; Ogumi, Z. Application of graphite–solid electrolyte composite anode in all-solid-state lithium secondary battery with Li2S positive electrode. *Solid State Ionics*. **2014**, *262*, 138-142.

(108) Takada, K.; Inada, T.; Kajiyama, A.; Sasaki, H.; Kondo, S.; Watanabe, M.; Murayama, M.; Kanno, R. Solid-state lithium battery with graphite anode. *Solid State Ionics*. **2003**, *158*, 269-274.

Chapter 2 Comparison of sulfur cathode reactions between concentrated liquid electrolyte system and solid-state electrolyte system by soft X-ray absorption spectroscopy

Sulfur is one of the promising next-generation cathode materials because of its low cost and high theoretical gravimetric capacity. However, the reaction mechanism of the sulfur cathode is largely influenced by the electrolyte and the intermediate sulfur species during first discharge process has not been quantitatively explored in different electrolytes. In this study, we elucidated the reaction mechanism of sulfide cathodes by using three different electrolyte systems, viz., a conventional liquid electrolyte (LiPF$_6$/ ethylene carbonate (EC): ethylene-methyl carbonate (EMC)), a concentrated liquid electrolyte (lithium bis(trifluorosulfonyl)amide (LiTFSA)/tetraglyme (G4): 1,1,2,2-tetrafluoroethyl 2,2,3,3-tetrafluoropropyl ether (HFE)), and a solid-state electrolyte (Li$_3$PS$_4$). Soft X-ray absorption spectroscopy was used to examine the reaction mechanism of the sulfur cathode in the liquid and solid-state electrolytes during the first discharge process. In the conventional electrolyte, the sulfur cathode was reduced to long-chain polysulfide (S$_6^{2-}$) during the first discharge process and the polysulfide subsequently dissolved into the electrolyte. In the concentrated electrolyte, the sulfur cathode was reduced to mid-chain polysulfide (S$_4^{2-}$) at the initial stage of the first discharge process, and then reduced to short-chain polysulfide (S$_2^{2-}$) and Li$_2$S followed by the formation of long-chain polysulfide (S$_6^{2-}$). In the solid-state electrolyte, the sulfur cathode was reduced to long-chain polysulfide (S$_6^{2-}$) at the initial stage of the first discharge process and was gradually reduced to mid-chain polysulfide (S$_4^{2-}$), short-chain polysulfide (S$_2^{2-}$), and Li$_2$S. The differences in these reaction pathways govern electrochemical properties such as the difference in discharge voltage.

53

2.1 Introduction

Sulfur is an attractive cathode material having a high theoretical specific capacity of 1672 mAh/g; the other advantages of sulfur include high abundance, environmental friendliness, and low cost.[1-4] Therefore, lithium–sulfur batteries are among the most competitive next-generation electrochemical energy storage devices.[5-8] However, the sulfur-based cathode has a major disadvantage of poor cyclability because the polysulfide generated during the discharge/charge processes, dissolves in the conventional liquid electrolyte, which is essentially an ether/ether mixed solvent.[9]

To solve the problem caused by the high solubility of the polysulfide in the conventional liquid electrolyte, two methods have been proposed by researchers— one involves the use of concentrated liquid electrolytes[10-15] and the other involves the use of solid-state electrolytes.[16-19] In the concentrated liquid electrolyte, the solubility of the polysulfide is significantly low due to the lack of free solvents in the bulk electrolyte, and this suppresses the dissolution of the polysulfide.[10, 11] Similarly, polysulfide dissolution cannot occur in solid-state electrolytes. Although these approaches are effective in suppressing polysulfide dissolution, the sulfur cathode in the two systems shows differences in the electrochemical behavior, especially in the first discharge curve. In the concentrated liquid electrolyte system, the sulfur cathode shows two potential plateaus during the discharge process, similar to the conventional liquid electrolytes, although the potentials of the plateau region are different.[10-12] On the other hand, in the solid-state electrolyte system, the sulfur cathode shows a single plateau during the first discharge.[17-23] To understand the difference in the electrochemical behavior of sulfur cathodes caused by the difference in the electrolyte, it is necessary to understand the reaction mechanism of the sulfur electrode.

Many spectroscopic techniques such as NMR,[24] Raman spectroscopy,[25] UV-vis spectroscopy,[26-28] and X-ray absorption spectroscopy (XAS)[29, 30] have been used to investigate the reaction mechanism in various conventional liquid electrolytes. The results of UV-vis spectroscopy and/or XAS measurements show that the sulfur cathode is reduced to short-chain polysulfide and Li_2S via long-chain or middle-chain polysulfide with disproportionation reaction during the discharge process in conventional liquid electrolyte.[28, 29] There are some qualitative reports on the use of an acetonitrile (ACN)-based solvate electrolyte mixed with 1,1,2,2-tetrafluoroethyl 2,2,3,3-tetrafluoropropyl ether (TTE) (1:1 by volume) as a concentrated liquid electrolyte system,[13] but quantitative studies on the reaction mechanism have not been conducted. Moreover, for the solid-state electrolyte system, there is an example where Takeuchi and co-workers established the final product of the reaction in the Li_2S system by XAS;[31] however, the reaction mechanism of the sulfur cathode has not been clearly established.

In the present study, electronic structure changes of the sulfur cathode in the conventional liquid electrolyte, a concentrated liquid electrolyte, and a solid-state electrolyte were examined by XAS analysis. In particular, we applied the *operando* XAS technique to examine the electronic structure changes of the sulfur cathode in the conventional electrolyte and the concentrated liquid electrolyte because polysulfides have solubility and the sulfur cathode during the discharge process is in a non-equilibrium state.[32-34] Moreover, the formation of and changes in the polysulfide species during the first discharge process in a sulfur-based all-solid-battery were investigated by XAS for the first time.

2.2 Experimental Section
2.2.1 Sample preparation

A sulfur/CNovel composite was prepared by mixing sulfur and mesoporous carbon (CNovel®, Toyo tanso) in a weight ratio of sulfur:CNovel = 65:35. The mixture of sulfur and the CNovel was heated to 155°C for 5 h to allow diffusion of the melted sulfur into the pores of the CNovel. Li_3PS_4 glass powder was prepared by ball milling following a previously reported procedure; typically, Li_2S (Aldrich, 99.9%) and P_2S_5 (Aldrich, 99%) powder in 3:1 mol ratio were mixed with ZrO_2 balls for 30 h at 370 rpm.[35]

2.2.2 Characterization

The surface morphologies of the CNovel and sulfur/CNovel composites were analyzed by transmission electron microscopy (TEM, JEOL JEM-2100F) and scanning electron microscopy (SEM, SU-1500, HITACHI). The amount of sulfur in the sulfur/CNovel composite was examined by thermogravimetric analysis (TGA, DTG-60AH, Shimadzu) under Ar atmosphere at a heating rate of 5 °C min^{-1}. The sulfur/CNovel composite prepared by mixing sulfur and the CNovel was characterized by TGA, as shown in Figure 2.1. The results indicated a weight loss of ~65% above 350 ℃, implying that the sulfur content in the composite was about 65%.

The structure of the prepared Li_3PS_4 powder was examined by X-ray diffraction (XRD) with an X-ray diffractometer (Cu Kα, Ultima IV; Rigaku Corp.). The ionic conductivity of the prepared Li_3PS_4 was measured by electrochemical impedance spectroscopy (EIS) using a Solartron Modulab ECS. The AC amplitude was 20 mV, with the applied frequency ranging from 1 MHz to 10 Hz at 25°C.

2.2.3 Electrochemistry performance in liquid lithium sulfur battery

Electrochemical performances of the sulfur/CNovel composite were investigated in a liquid electrolyte and solid-state electrolyte using a two-electrode cell. The sulfur/CNovel composite cathode for the liquid electrolyte systems was prepared by mixing the sulfur/CNovel composite, acetylene black, carboxymethyl cellulose, and styrene–butadiene rubber in a weight ratio of 90:5:3:2, respectively, and was supported by a carbon paper. Li metal foil was used as the counter electrode. 1 M $LiPF_6$/ ethylene carbonate (EC):ethylene-methyl carbonate (EMC) (3:7 vol%) as the conventional electrolyte and lithium bis(trifluorosulfonyl)amide (LiTFSA):tetraglyme (G4): 1,1,2,2-tetrafluoroethyl 2,2,3,3-tetrafluoropropyl ether (HFE) (10:8:40 mol%) as the concentrated liquid electrolyte were used in a glass fiber membrane separator. The two-electrode cells were assembled in a glove box filled with Ar. A typical charge-discharge cycling test was carried out at a current density of 0.1 C (1 C= 1672 mAh/g) with the cut off voltages of 1.0 V for the discharge and 3.0 V for the charge process at 25 °C.

The prepared Li_3PS_4 powder showed some broad patterns in XRD, which matches with the pattern reported in a previous study[35] (Figure 2.2). Moreover, the ionic conductivity showed a value (2.09×10^{-4} S/cm at 25 °C) similar to that reported in a previous study[35] (Figure 2.3). These results indicate that the prepared Li_3PS_4 glass can be used to measure the electrochemical performance of the sulfur/CNovel composites. The sulfur/CNovel composite cathode for the solid-state electrolyte system was prepared via ball milling technique by mixing the sulfur/CNovel and Li_3PS_4 in a weight ratio of 6:4 at 300 rpm for 15 min with a ZrO_2 ball. The prepared Li_3PS_4 glass was used as a solid electrolyte (SE) layer. The obtained sulfur composite cathode and the SE layer were placed in a polycarbonate tube (diameter of 10 mm) and pressed together under a

pressure of 360 MPa. A Li–In alloy[19, 36] was placed on the surface of the SE layer of the bilayer pellet to function as an anode. Two stainless steel rods were set on the cathode and anode sides by applying a pressure of 120 MPa, and they functioned as current collectors. The three-layered pellet was finally interposed between two stainless-steel rods that served as current collectors. The entire cell preparation processes were carried out in a dry Ar filled glove box. Electrochemical tests were conducted at a current density of 0.25 mA/cm^2 with cutoff voltages of 0.5 V (1.12 V vs. Li)[37] for discharge and 3.0 V (3.62 V vs Li) for charge at 25 °C.

2.2.4 X-ray Absorption Spectroscopy

operando XAS measurement was performed to understand the electronic structure of sulfur compounds in a non-equilibrium state in both the conventional liquid and the concentrated liquid electrolyte. In the liquid electrolytes, *operando* XAS spectra of S *K*-edge for the sulfur/CNovel composite cathode were measured with the partial fluorescence yield (PFY) mode at the beamline of the SPring-8 synchrotron radiation facility (BL27SU) in Hyogo, Japan. A home-made cell was constructed following a previously reported procedure and used for the *operando* XAS[32] measurement. To construct the cell, the sulfur/CNovel composite material was mounted on a polyimide film to serve as the working electrode. 1 M LiPF$_6$/EC: EMC (3: 7 vol%) or LiTFSA/G4: HFE (10:8:40 mol%) was used as the liquid electrolyte, lithium foil was used as the counter electrode, and the glass fiber membrane was used as the separator in the cell. The *operando* cell was assembled in an Ar filled glovebox and transferred into a vacuum chamber, and the XAS measurements were carried out under galvanostatic discharge process at a current density of 0.1 C (1 C= 1672 mAh/g).

In the solid-state electrolyte system, ex situ XAS spectra of S *K*-edge for sulfur

cathode were measured with the total electron yield (TEY) mode at the beamline of the SPring-8 synchrotron radiation facility (BL27SU) in Hyogo, Japan. The electrodes for the ex situ XAS measurement were constructed following the procedure for electrode construction for the galvanostatic discharge measurements. After the discharge measurements, the cells were dissembled in an Ar-filled glove box. The prepared electrodes were transferred to the vacuum chamber without air exposure.

2.3 Result and discussion

The TEM image of mesoporous carbon and SEM image of sulfur/CNovel composite are shown in Figures 2.4a and 2.4b, respectively. However, the TEM image of the sulfur/CNovel composite could not be recorded because the sample was damaged by the electron beam irradiation. The pore size of the CNovel obtained from TEM images was 5-10 nm, and the particle size of the sulfur/CNovel observed in SEM images was 30-100 μm. Next, the electrochemical performance of the sulfur/CNovel cathode was examined in different electrolyte systems. Figure 2.4c shows the first charge-discharge profiles of the sulfur/CNovel cathode in the $LiPF_6$/EC: EMC conventional electrolyte, LiTFSA/G4: HFE concentrated liquid electrolyte, and Li_3PS_4 solid electrolyte. The results demonstrate that the sulfur/CNovel cathode showed different electrochemical performance in different electrolytes. In the conventional liquid electrolyte, the sulfur/CNovel cathode material showed a discharge capacity of 319 mAh/g, with a plateau at 2.4 V, and without any charge capacity. This behavior was similar to previous reports,[38] as the nucleophilic sulfide anions can react with the carbonate solvent. In the concentrated liquid electrolyte, the sulfur/CNovel cathode material showed two plateaus at 2.2 V and 1.8 V with a capacity of 935 mAh/g during the discharge process, and a charge capacity of 692 mAh/g, which was in good agreement with our previous report.[11] In the solid electrolyte, the sulfur/CNovel cathode material showed a discharge capacity of 1211 mAh/g with a plateau at 1.8 V and a charge capacity of 602 mAh/g. The single discharge plateau for sulfur/CNovel in the all-solid-state battery was indicative of the typical electrochemical performance for all-solid-state lithium sulfur batteries.[19] One of the reasons of the irreversible capacity during first cycling could be caused by the decomposition of the Li_3PS_4 as discussed later. After the first cycling, the sulfur/CNovel cathode material shows keep the capacity in the LiTFSA/G4: HFE

concentrated liquid electrolyte, and Li$_3$PS$_4$ solid electrolyte (Figure 2.5).

To further investigate the difference in the electrochemical performance of the sulfur/CNovel composite cathode, XAS measurements were conducted in the conventional liquid electrolyte, concentrated liquid electrolyte, and solid electrolyte. The results of S K-edge XANES in the conventional liquid electrolyte, concentrated liquid electrolyte, and solid electrolyte are shown in Figures 2.6a-c, respectively.

For all the sulfur/CNovel composites, before the discharge process, an absorption peak appeared at 2471.8 eV, which could be attributed to the electron transition from S 1s to S–S π*[39] state of elemental sulfur.[39] In the conventional liquid electrolyte, although a new shoulder peak attributed to linear polysulfide appeared at 2470 eV,[39] peaks attributed to Li$_2$S did not appear at 2472.8 eV and 2475.2 eV[39] during the discharge process. This result indicates that linear polysulfide was formed whereas Li$_2$S was not formed during first discharge process in the conventional liquid electrolyte. In the concentrated liquid electrolyte, a new peak attributed to linear polysulfide appeared at 2470 eV[39] at the early stage of the discharge process. In the subsequent discharge process, new two peaks attributed to Li$_2$S gradually appeared at 2472.8 eV and 2475.2 eV,[39] and the peak intensity increased as the discharge reaction proceeded in the forward direction. This result indicates that sulfur was transformed to Li$_2$S via linear polysulfide during first discharge process in the concentrated liquid electrolyte. In the Li$_3$PS$_4$ solid electrolyte, a new peak attributed to linear polysulfide appeared at 2470 eV[39] at the initial and middle stages of the discharge process. At the final stage of the discharge process, new two peaks attributed to Li$_2$S appeared at 2472.8 eV and 2475.2 eV. In addition, an absorption peak at 2471 eV appeared during the final discharge process. This peak was attributed to the electronic transition from the S 1s orbital to the

61

antibonding S $3p\sigma*$[40] orbital of the Li_3PS_4 solid electrolyte. This result indicates that sulfur was transformed to Li_2S via linear polysulfide during first discharge process in the Li_3PS_4 solid electrolyte.

In order to estimate the amount of the sulfur components during the discharge processes, a linear combination fitting (LCF)[30] analysis was performed. We used the spectra of the elemental sulfur (S_8), long-chain polysulfides S_6^{2-}, mid-long chain lithium polysulfides S_4^{2-}, short-chain polysulfides S_2^{2-}, and Li_2S (Figure 2.7) as reference spectra for the LCF analysis. In particular, the Li_3PS_4 solid electrolyte spectrum was added as the reference spectra for the LCF analysis of the sulfur cathode in the Li_3PS_4 solid electrolyte.

In the Li_3PS_4 solid electrolyte, S_8, S_6^{2-}, S_4^{2-}, S_2^{2-} and Li_2S were used as the stander materials to do the linear combination fitting at first. However, the fitting result can't match well with the XANES spectra data especially for $Li_{1.0}S$ and $Li_{1.2}S$ (Figure 2.8). The absorption peak at 2471 eV may correspond to S K-edge of the Li_3PS_4 (ionic conductor in cathode). At this point, Li_3PS_4 was also used as stander material to do linear combination fitting of XANES spectra of each discharge status. As showed in Figure 2.9, the LCF result can fit well with the XANES spectra of $Li_{1.0}S$ and $Li_{1.2}S$, which means this method can be employed to analysis the polysulfides species changes in all-solid-state battery.

The obtained LCF results are shown in Figure 2.10 and 2.11. In the conventional liquid electrolyte (Figure 2.10a), the amount of S_8 decreased, while that of S_6^{2-} increased, and short-chain polysulfides S_4^{2-}, S_2^{2-}, and Li_2S were not detected during the first discharge process. Lithium content (x in Li_xS) was calculated by the LCF analysis and was compared to the lithium content estimated by the discharge capacity (Figure

2.10b). The lithium content calculated by the LCF analysis was lower than of the lithium content estimated by the electrochemical measurement; this discrepancy arises due to the dissolution of polysulfide in the conventional electrolyte.[38, 41]

In the concentrated liquid electrolyte (Figure 2.10c), the amount of S_8 decreased while that of S_4^{2-} increased at the beginning of discharge process. In the middle of the discharge process, the amounts of S_4^{2-} and S_6^{2-} further increased, while that of S_8 decreased. However, at the end of the discharge process, the amounts of S_4^{2-} and S_6^{2-} decreased, while the amounts of S_2^{2-} and Li_2S increased. The lithium content calculated by the LCF analysis (Figure 2.10d) increased in the range of x=0–0.4, and the value matches well with the value estimated by electrochemical measurement; however, the lithium content estimated by LCF analysis remained constant in the range of x=0.6–1.0, the value being largely lower than the value estimated by electrochemical measurement. Finally, the lithium content rapidly increased at x = 1.2, approaching the value estimated by electrochemical measurement. The lithium content was largely lower than the theoretical value in the middle stage of discharge, and it rapidly approached the theoretical value at the final stage of discharge. This behavior is similar to a previously reported phenomenon[25] in which the S^{2-} ion exists in a supersaturated state at the middle stage of discharge and suddenly precipitates at the electrode as Li_2S at the final stage of discharge. A similar phenomenon might be observed in the concentrated liquid electrolyte because the solubility of short-chain polysulfides is independent of the electrolyte concentration.[11]

In the Li_3PS_4 solid electrolyte (Figure 2.10e), the amount of S_8 decreased whereas that of S_6^{2-} and S_2^{2-} increased at the beginning of the discharge process. In the middle of the discharge process, the amount of S_4^{2-} increased, while that of S_8 decreased, but

the amounts of S_6^{2-} and S_2^{2-} remained almost constant. However, at the end of the discharge process, the amounts of S_6^{2-} and S_4^{2-} decreased, while those of S_2^{2-} and Li_2S increased. The lithium content calculated by the LCF analysis (Figure 2.10f) increased in the range of x=0–1.0, but the value was lower than the value estimated by electrochemical measurement. However, the lithium content rapidly increased at the x = 1.2, exceeding the value estimated by electrochemical measurement. Although the lithium ion content calculated by the LCF analysis was lower than the theoretical value in the middle stage of discharge, it was higher than the theoretical value at the final stage of discharge. This phenomenon can be attributed to the reaction distribution in the composite electrode and the decomposition reaction of Li_3PS_4 solid electrolyte. In all-solid-state battery, reaction proceeds from the solid electrolyte side and the reaction distribution is generated in the depth direction of the composite electrode because ionic conduction is slower than electronic conduction.[42] As the XANES spectra obtained with the TEY mode include mainly the sulfur cathode at the current collector side, the lithium content obtained by the LCF analysis was lower than the theoretical value in the middle stage of discharge. At the final stage of discharge, the reaction distribution along the depth direction of the composite electrode disappeared, and thus, the lithium content obtained by the LCF analysis approached the theoretical value. In addition, the XANES spectra contain information about decomposed product of the Li_3PS_4 solid electrolyte at the final stage of discharge. It has been reported that Li_3PS_4 is reduced to Li_2S and $Li_4P_2S_6$ at 2 V (vs. Li+/Li) by theoretical thermodynamics calculations.[43] In order to examine the reductive decomposition of Li_3PS_4 electrolyte, the Li_3PS_4 was kept at the potential of 0 V (vs. Li^+/Li) and analyzed by using XAS for S and P K-edge (Figure 2.12). XANES for S K-edge shows peaks attributed to Li_2S at 2473 and 2484 eV (Figure 2.12(a)) and XANES for P K-edge shows a broad peak at lower energy around 2144 eV

than the pristine Li_3PS_4 (Figure 2.12(b)), meaning formation of reduced phosphorus species. These XAS results correspond to the theoretical thermodynamics calculations in the previous report.[43] Therefore, the LCF analysis includes the Li_2S formed by the decomposition of the Li_3PS_4, leading to overestimate the lithium content. After first discharge process, the decomposed product suppresses further decomposition of Li_3PS_4 solid electrolyte, reducing significantly the irreversible capacity (Figure 2.5). The disappearance of reaction distribution and the Li_2S formation by the decomposition of the Li_3PS_4 could result in the higher lithium content by LCF analysis than the theoretical value.

Furthermore, we propose the reaction mechanisms for the sulfur/CNovel cathode in different electrolyte systems based on the results of the LCF analysis.

In the conventional liquid electrolyte, the sulfur cathode showed a single plateau and a poor discharge capacity during the first discharge process. The XAS results showed that only the S_6^{2-} content increased but the S_8 content decreased during the discharge process, and the lithium content calculated by the LCF analysis was lower than of the lithium content estimated by the electrochemical result. These results indicate that S_8 was reduced to S_6^{2-} during the discharge process, and S_6^{2-} dissolved in the $LiPF_6$/ EC: EMC conventional electrolyte, which was caused by a chemical reaction between S_6^{2-} and the carbonate solvent.[38, 41] Therefore, the sulfur cathode showed the low capacity, as seen in Figure 2.13a.

In the concentrated liquid electrolyte, the sulfur cathode showed two plateaus at 2.2 V and 1.8 V (vs. Li^+/Li) during the first discharge process. The XAS measurements revealed the conversion of S_8 to S_4^{2-} at the first plateau, formation of S_6^{2-} at the second plateau, and formations of S_2^{2-} and Li_2S after the 2nd plateau. This behavior is largely

different from the conventional electrolyte, where the sulfur was reduced to S_6^{2-} at the initial stage during the first discharge process, as shown in Figure 2.13a. In the concentrated liquid electrolyte, however, the formation of S_6^{2-} was slower because of the low solubility of polysulfide,[11] resulting in the reaction $1/2S_8 + 2Li^+ + 2e- \leftrightarrows Li_2S_4$. In the subsequent discharge process, S_6^{2-} was formed from S_4^{2-} by the following reactions $S_4^{2-} + 1/4S_8 \rightarrow 2 S_3^{\cdot-}$ and $2 S_3^{\cdot-} \leftrightarrows S_6^{2-}$.[28, 30] Finally, S_2^{2-} and Li_2S were formed at the end of the discharge process. The low solubility of polysulfides in the LiTFSA/G4: HFE concentrated liquid electrolyte changed the reaction pathway of the sulfur cathode in the first discharge process as shown in Figure 2.13b.

In the solid electrolyte, the sulfur cathode showed only one discharge plateau around 1.8 V vs Li. The XAS showed that S_8 was reduced to S_6^{2-} and S_2^{2-} at first and then S_6^{2-} was gradually converted to S_4^{2-}, S_2^{2-}, and Li_2S. In liquid electrolyte, the sulfur cathode is reduced to Li_2S with disproportionation reaction between polysulfides and sulfur.[29, 30, 44, 45] However, it's difficult that the polysulfide formed in the discharge process reacts with sulfur in the solid electrolyte because the polysulfide does not dissolve in the solid electrolyte. Therefore, the sulfur cathode undergoes stepwise reduction to Li_2S without the disproportionation reaction. Our results show that the reaction pathway of polysulfides in the solid electrolyte is significantly different from the liquid electrolyte as shown in Figure 2.13c.

2.4   Conclusion

We measured the electrochemical performance of the sulfur cathode in the conventional liquid electrolyte, the concentrated liquid electrolyte, and the solid electrolyte. In the conventional electrolyte, the sulfur cathode showed low capacity and low coulombic efficiency because the long-chain polysulfide (S_6^{2-}) formed in the first discharge process subsequently dissolved into the electrolyte (Figure 2.14a). In the concentrated electrolyte, the sulfur cathode was reduced to mid-chain polysulfide (S_4^{2-}) at the initial stage of the first discharge process (Figure 2.14b), and then reduced to short-chain polysulfide (S_2^{2-}) and Li_2S followed by the formation of long-chain polysulfide (S_6^{2-}). The reaction pathway is largely different from conventional liquid electrolytes, which is attributed to the low solubility of polysulfide in the concentrated electrolyte. In the Li_3PS_4 solid electrolyte, the sulfur cathode was reduced to long-chain polysulfide (S_6^{2-}) at the initial state of the first discharge process (Figure 2.14c) and then subsequently reduced to mid-chain polysulfide (S_4^{2-}), short-chain polysulfide (S_2^{2-}), and Li_2S in a stepwise manner. The disproportionation reaction cannot occur in the solid electrolyte, and hence, the reaction pathway is different from the liquid electrolyte. The reaction pathway difference between concentrated electrolyte and solid electrolyte should influence the morphology of the final product of Li_2S in each electrolyte, leading to the difference of the overpotentials during each charge process. This study investigates the difference in the reaction pathway of sulfur cathode between the liquid and solid electrolyte by using soft X-ray absorption spectroscopy. We believe that these pieces of information about sulfur cathode will help to understand the reaction mechanisms of sulfur cathode and also to design the sulfur cathode with high electrochemical performance.
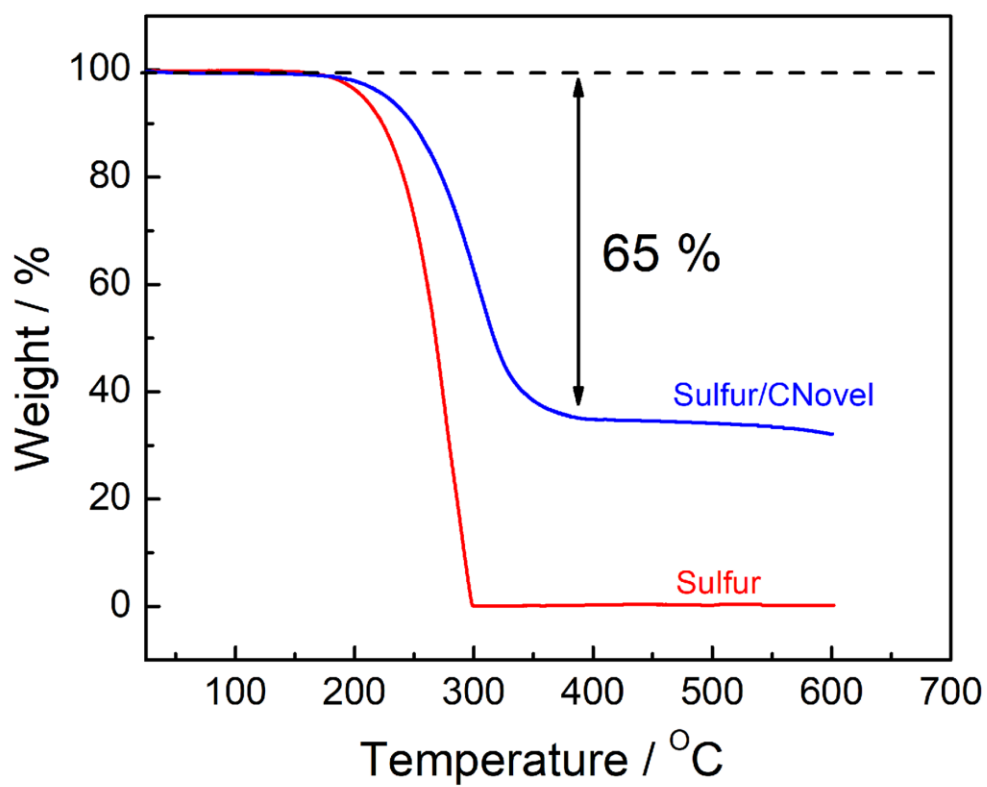
Figure 2.1. Thermo gravimetric analysis curves of sulfur and sulfur/CNovel powder.
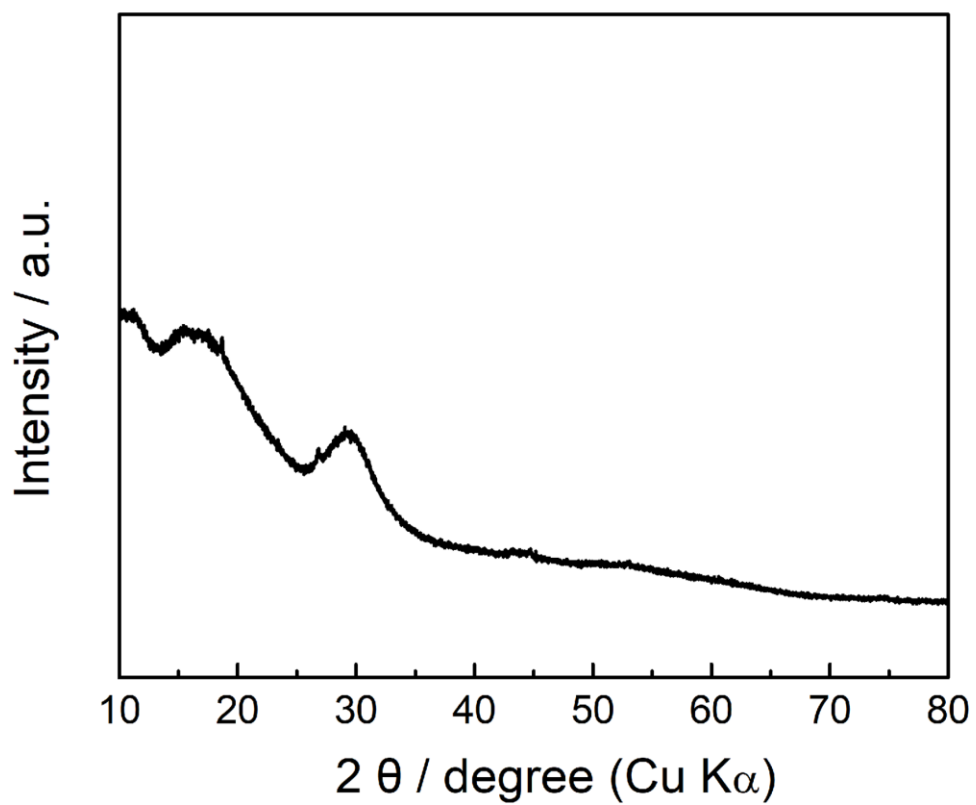
Figure 2.2. XRD pattern of the prepared Li_3PS_4.
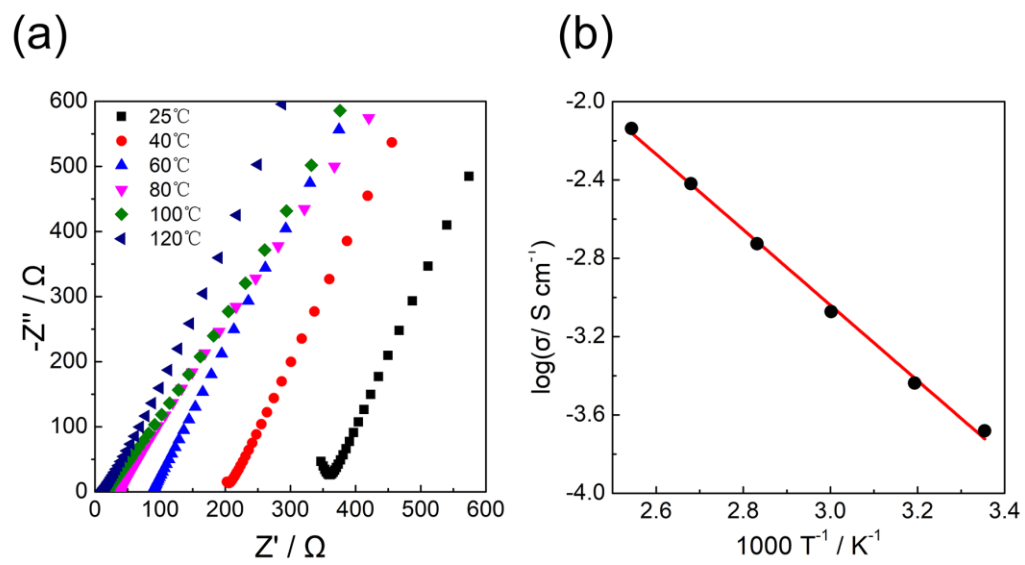
Figure 2.3. (a) Nyquist plots of the prepared Li_3PS_4 at different temperature, (b) Temperature dependence of the ionic conductivity of Li_3PS_4.
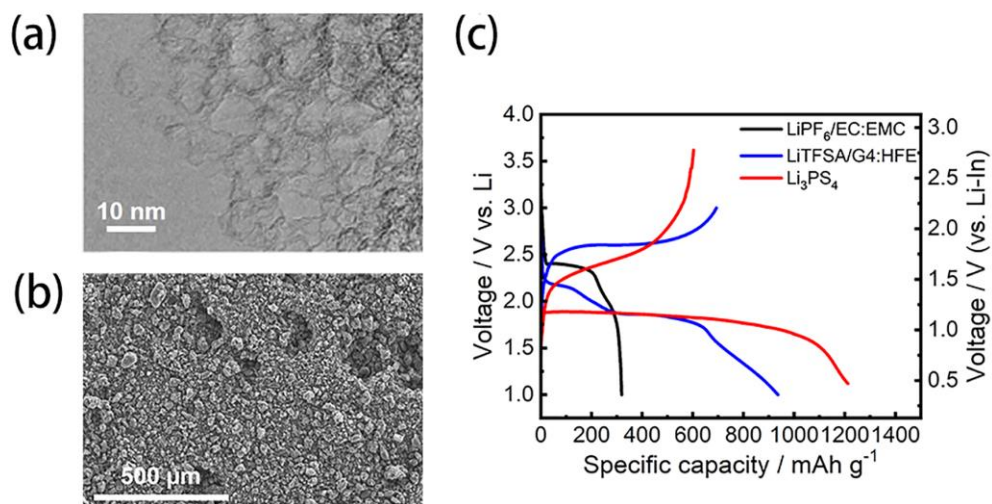
Figure 2.4. (a) TEM image of mesoporous carbon of CNovel, (b) SEM image of sulfur/CNovel, and (c) first charge and discharge profiles of sulfur/CNovel in LiPF$_6$/EC: EMC conventional electrolyte, LiTFSA/G4: HFE concentrated liquid electrolyte and Li$_3$PS$_4$ solid electrolyte.
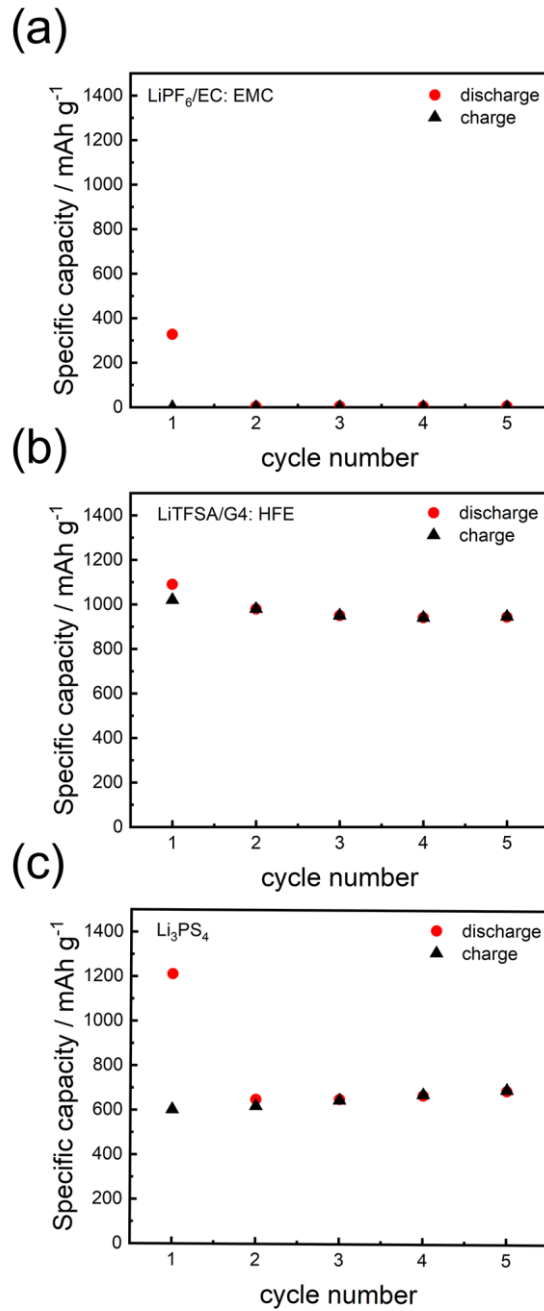
Figure 2.5. Cyclability for sulfur/CNovel cathode at (a) in theLiPF$_6$/EC: EMC conventional liquid electrolyte, (b) in the LiTFSA/G4: HFE concentrated liquid electrolyte, and (c) in the Li$_3$PS$_4$ solid-state electrolyte.
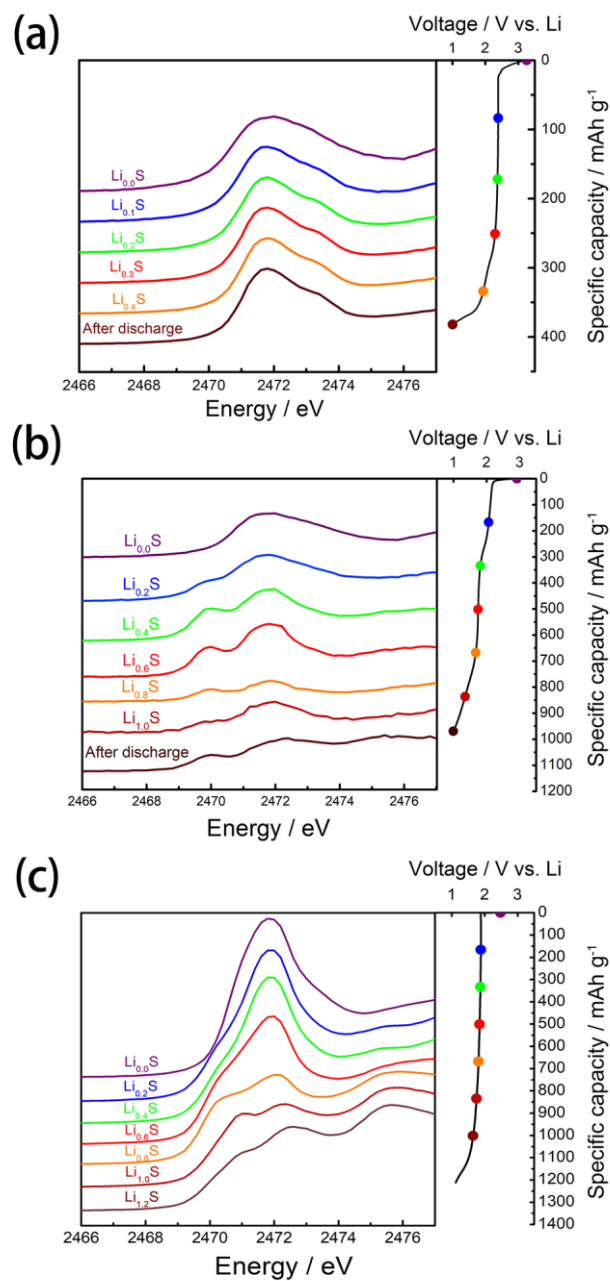
Figure 2.6. (a) S *K*-edge XANES of sulfur/CNovel cathode at different discharge states (a) in the $LiPF_6$/EC: EMC conventional liquid electrolyte, (b) in the LiTFSA/G4: HFE concentrated liquid electrolyte, and (c) in the Li_3PS_4 solid-state electrolyte.
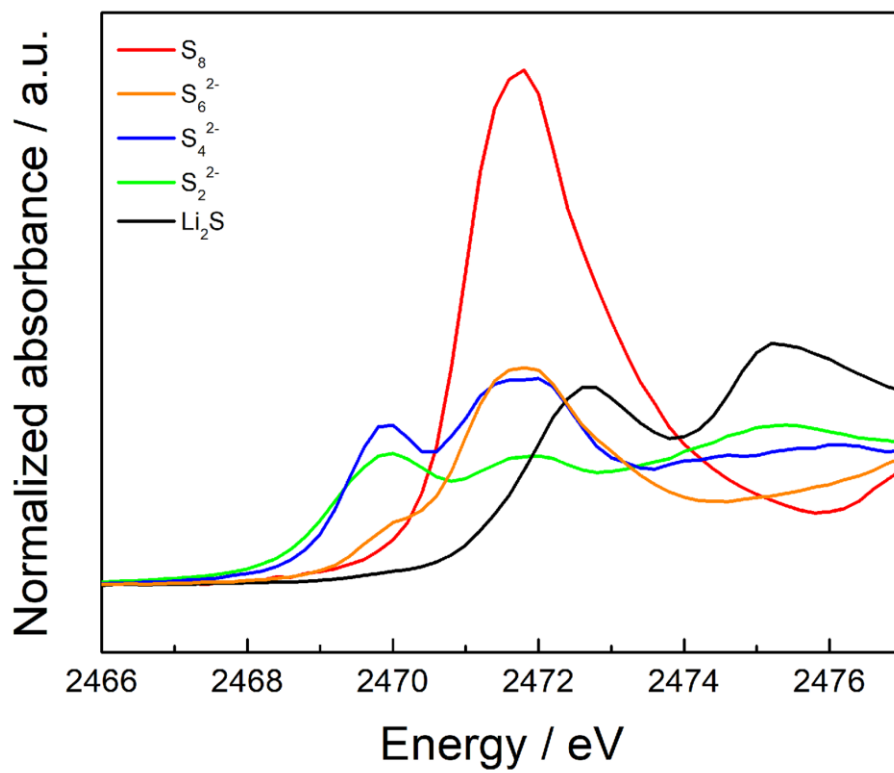
Figure 2.7. Sulfur *K*-edge XANES of standard materials S_8, S_6^{2-}, S_4^{2-}, S_2^{2-} and Li_2S.
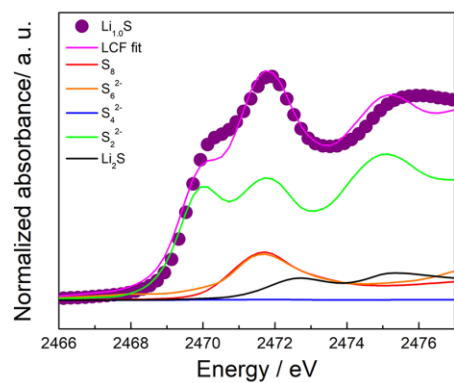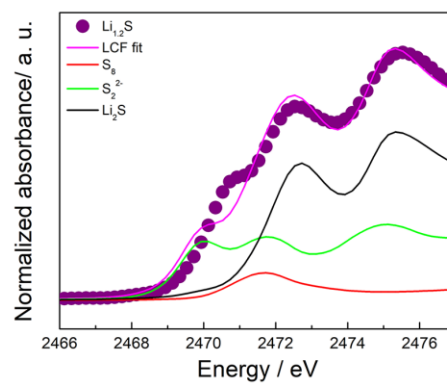
Figure 2.8. Linear combination fitting result of sulfur *K*-edge XANES of sulfur/CNovel cathode in all solid-state lithium sulfur battery by using stander material without Li_3PS_4 at discharge state of (a) $Li_{1.0}S$ and (b) $Li_{1.0}S$.
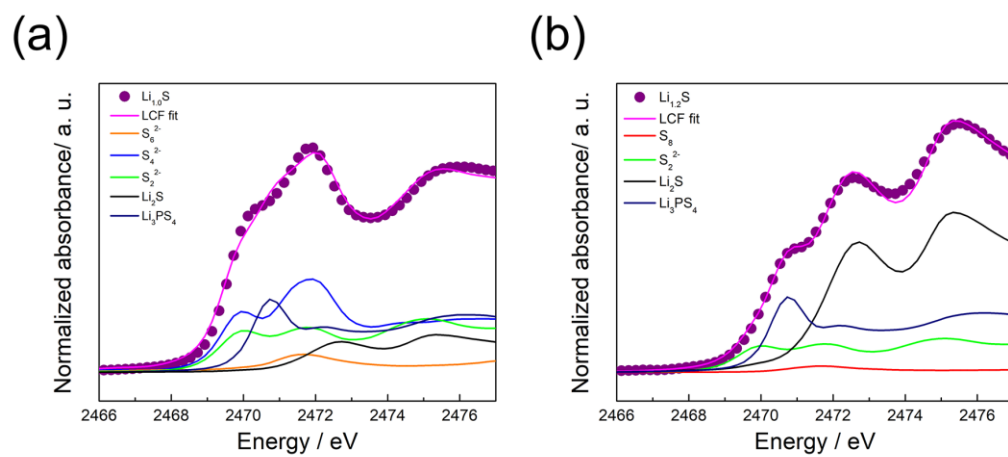
Figure 2.9. Linear combination fitting result of sulfur *K*-edge XANES of sulfur/CNovel cathode in all solid-state lithium sulfur battery by using stander material with Li_3PS_4 at discharge state of (a) $Li_{1.0}S$ and (b) $Li_{1.2}S$.
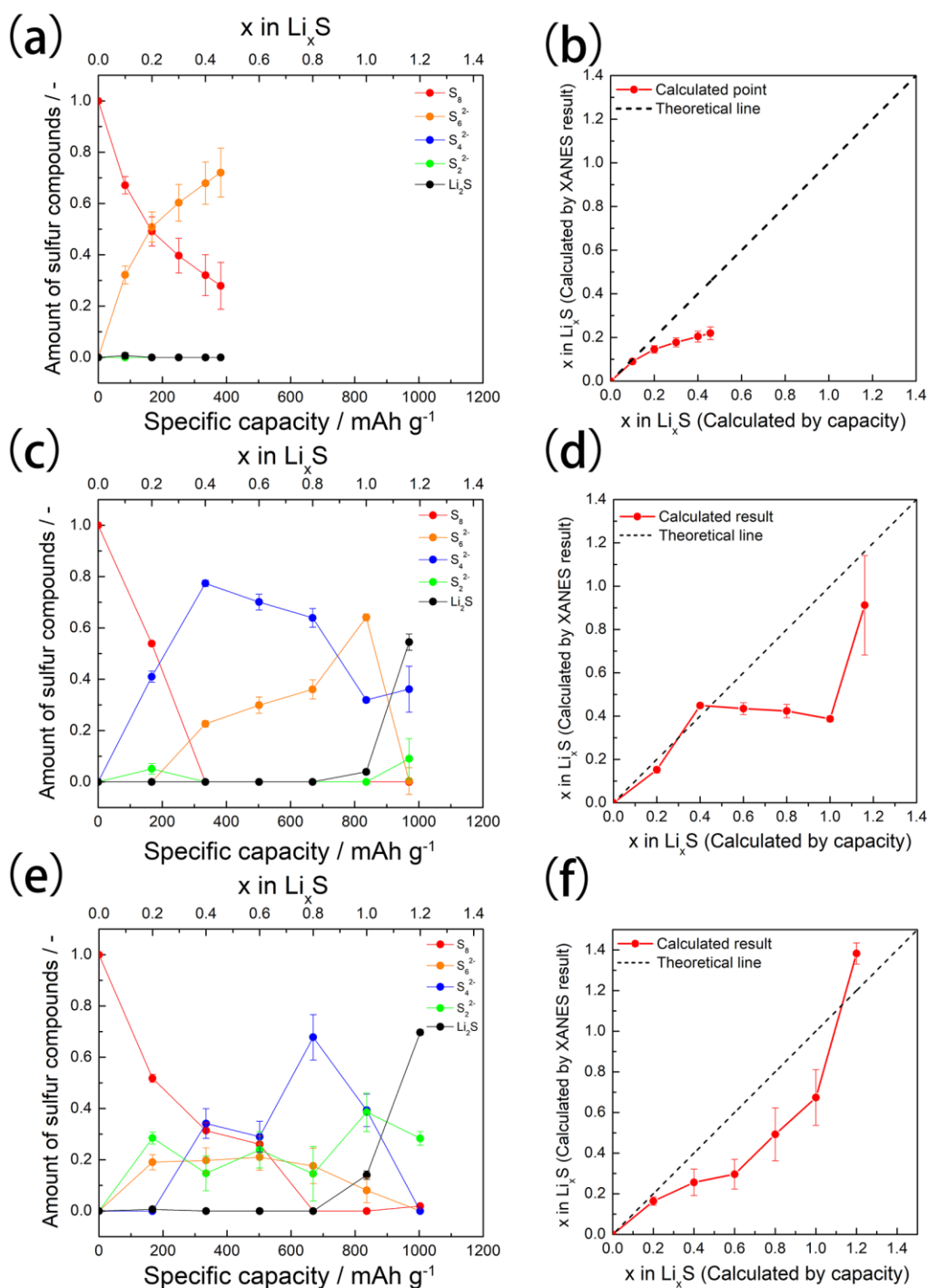
Figure 2.10. Sulfur compound ratio of the sulfur/CNovel cathode during first discharge process calculated by the linear combination fitting (LCF) analysis for the XANES spectra and lithium composition calculated by the LCF analysis and electrochemical capacity; (a), (b) in the $LiPF_6$/EC: EMC conventional liquid electrolyte, (c), (d) in the LiTFSA/G4: HFE concentrated liquid electrolyte, (e), (f) in the Li_3PS_4 solid-state electrolyte.
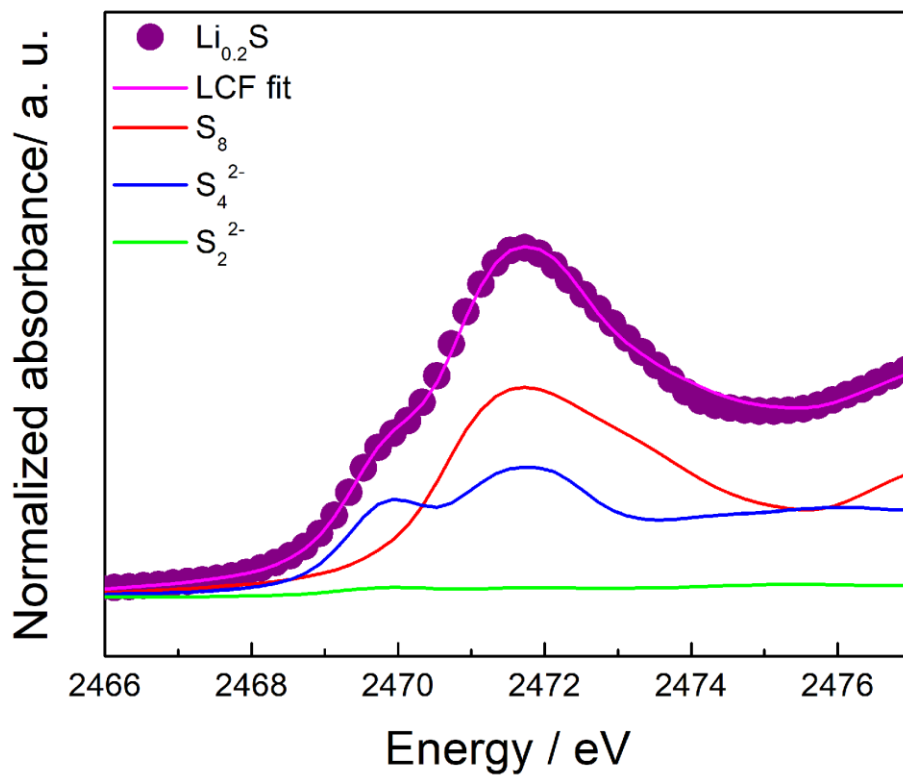
Figure 2.11. Linear combination fitting result of sulfur *K*-edge XANES of sulfur/CNovel cathode in LiTFSA/G4: HFE concentrated liquid electrolyte at discharge state of $Li_{0.2}S$.
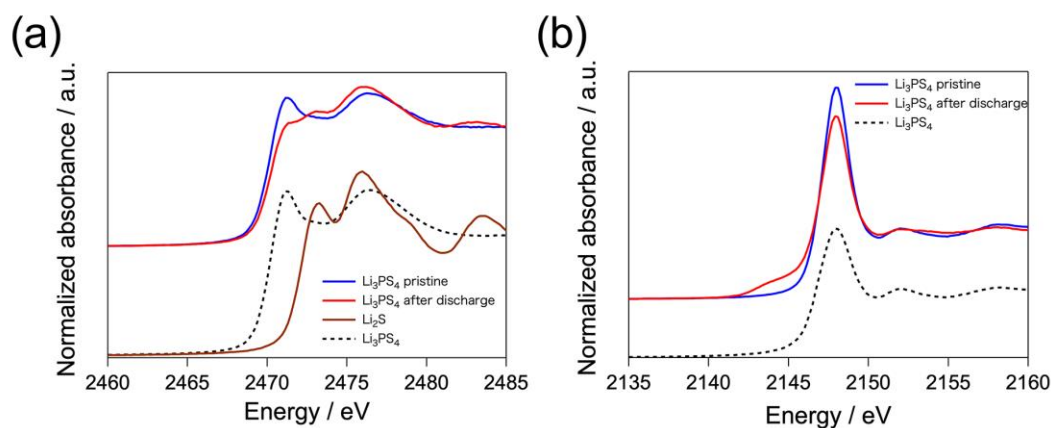
Figure 2.12. X-ray Absorption Near Edge Structure (XANES) for (a) S K-edge and (b) P K-edge of the Li$_3$PS$_4$ electrolyte after kept at the potential of 0 V (vs. Li$^+$/Li). The XANES spectra of the Li$_3$PS$_4$ sample before and after electrochemical measurement were collected with partial fluorescence mode at BL13 in Rits SR, Japan.
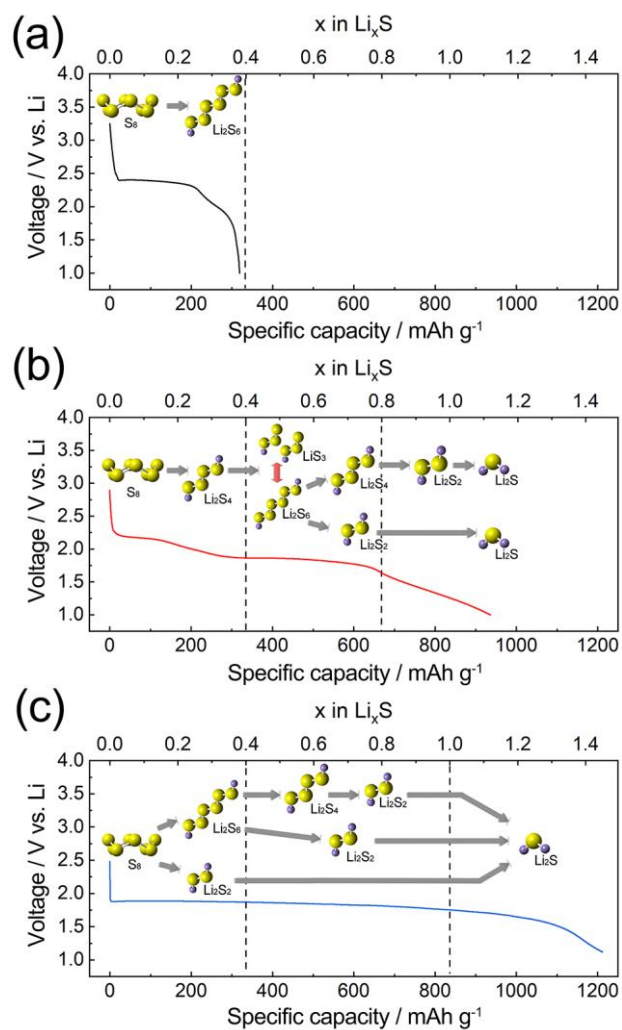
Figure 2.13. Schematics for proposed mechanism of sulfur/CNovel cathodes in (a) LiPF$_6$/EC: EMC conventional liquid electrolyte, (b) LiTFSA/G4: HFE concentrated liquid electrolyte, and (c) Li$_3$PS$_4$ solid-state electrolyte.
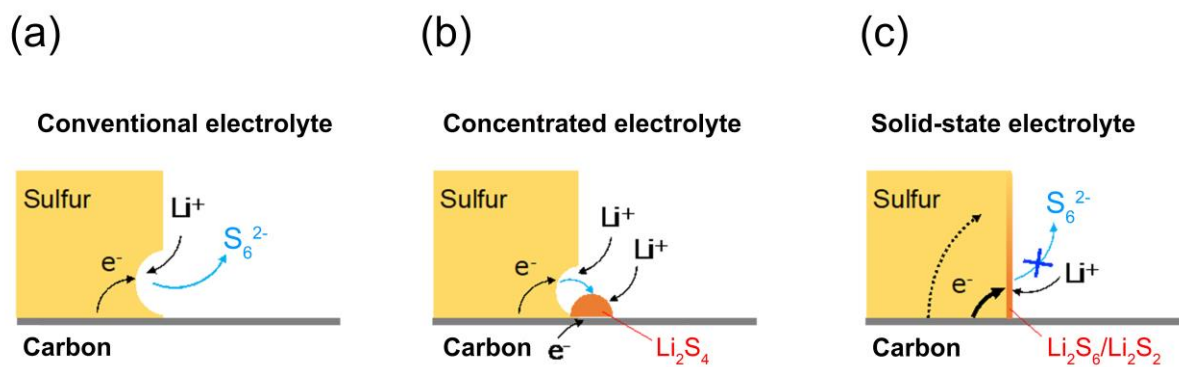
Figure 2.14. Reaction model of sulfur cathodes in (a) conventional electrolyte, (b) concentrated electrolyte and (c) solid-state electrolyte.

Reference

(1)   Zhou, G.; Yin, L.-C.; Wang, D.-W.; Li, L.; Pei, S.-F.; Gentle, I. R.; Li, F.; Cheng, H.-M. Fibrous Hybrid of Graphene and Sulfur Nanocrystals for High-Performance Lithium-Sulfur Batteries. *ACS Nano*. **2013**, *7*, 5367-5375.

(2)   Ellis, B. L.; Lee, K. T.; Nazar, L. F. Positive Electrode Materials for Li-Ion and Li-Batteries†. *Chem. Mater.* **2010**, *22*, 691-714.

(3)   Bruce, P. G.; Freunberger, S. A.; Hardwick, L. J.; Tarascon, J. M. Li-O_2 and Li-S batteries with high energy storage. *Nat. Mater.* **2011**, *11*, 19-29.

(4)   Evers, S.; Nazar, L. F. New Approaches for High Energy Density Lithium-Sulfur Battery Cathodes. *Acc. Chem. Res.* **2013**, *46*, 1135-1143.

(5)   Yin, Y.-X.; Xin, S.; Guo, Y.-G.; Wan, L.-J. Lithium-sulfur batteries: electrochemistry, materials, and prospects. *Angew. Chem., Int. Ed.* **2013**, *52*, 13186-200.

(6)   Manthiram, A.; Fu, Y.; Chung, S.-H.; Zu, C.; Su, Y.-S. Rechargeable lithium-sulfur batteries. *Chem. Rev.* **2014**, *114*, 11751-11787.

(7)   Pang, Q.; Liang, X.; Kwok, C. Y.; Nazar, L. F. Advances in lithium–sulfur batteries based on multifunctional cathodes and electrolytes. *Nat. Energy*. **2016**, *1*, 16132.

(8)   Seh, Z. W.; Sun, Y.; Zhang, Q.; Cui, Y. Designing high-energy lithium-sulfur batteries. *Chem. Soc. Rev.* **2016**, *45*, 5605-5634.

(9)   Zhang, S. S. Liquid electrolyte lithium/sulfur battery: Fundamental chemistry, problems, and solutions. *J. Power Sources*. **2013**, *231*, 153-162.

(10)   Ueno, K.; Park, J.-W.; Yamazaki, A.; Mandai, T.; Tachikawa, N.; Dokko, K.; Watanabe, M. Anionic Effects on Solvate Ionic Liquid Electrolytes in Rechargeable Lithium–Sulfur Batteries. *J. Phys. Chem. C*. **2013**, *117*, 20509-20516.

(11)   Dokko, K.; Tachikawa, N.; Yamauchi, K.; Tsuchiya, M.; Yamazaki, A.; Takashima, E.; Park, J. W.; Ueno, K.; Seki, S.; Serizawa, N.; Watanabe, M. Solvate Ionic Liquid Electrolyte for Li-S Batteries. *J. Electrochem. Soc.* **2013**, *160*, A1304-A1310.

(12)   Yanagi, M.; Ueno, K.; Ando, A.; Li, S. L.; Matsumae, Y.; Liu, J. L.; Dokko, K.; Watanabe, M. Effects of Polysulfide Solubility and Li Ion Transport on Performance of Li-S Batteries Using Sparingly Solvating Electrolytes. *J. Electrochem. Soc.* **2020**, *167*, 070531.

(13)   Lee, C. W.; Pang, Q.; Ha, S.; Cheng, L.; Han, S. D.; Zavadil, K. R.; Gallagher, K. G.; Nazar, L. F.; Balasubramanian, M. Directing the Lithium-Sulfur Reaction Pathway via Sparingly Solvating Electrolytes for High Energy Density Batteries. *ACS Cent. Sci*. **2017**, *3*, 605-613.

(14) Shin, E. S.; Kim, K.; Oh, S. H.; Cho, W. I. Polysulfide dissolution control: the common ion effect. *Chem. Commun.* **2013**, *49*, 2004-2006.

(15) Cuisinier, M.; Cabelguen, P. E.; Adams, B. D.; Garsuch, A.; Balasubramanian, M.; Nazar, L. F. Unique behaviour of nonsolvents for polysulphides in lithium-sulphur batteries. *Energy Environ. Sci.* **2014**, *7*, 2697-2705.

(16) Yue, J.; Yan, M.; Yin, Y.-X.; Guo, Y.-G. Progress of the Interface Design in All-Solid-State Li-S Batteries. *Adv. Funct. Mater.* **2018**, *28*, 1707533.

(17) Nagata, H.; Chikusa, Y. A lithium sulfur battery with high power density. *J. Power Sources.* **2014**, *264*, 206-210.

(18) Yao, X.; Huang, N.; Han, F.; Zhang, Q.; Wan, H.; Mwizerwa, J. P.; Wang, C.; Xu, X. High-Performance All-Solid-State Lithium-Sulfur Batteries Enabled by Amorphous Sulfur-Coated Reduced Graphene Oxide Cathodes. *Adv. Energy Mater.* **2017**, *7*, 1602923.

(19) Nagao, M.; Hayashi, A.; Tatsumisago, M. Sulfur–carbon composite electrode for all-solid-state Li/S battery with $Li_2S–P_2S_5$ solid electrolyte. *Electrochim. Acta.* **2011**, *56*, 6055-6059.

(20) Zhang, Q.; Huang, N.; Huang, Z.; Cai, L. T.; Wu, J. H.; Yao, X. Y. CNTs@S composite as cathode for all-solid-state lithium-sulfur batteries with ultralong cycle life. *Journal of Energy Chemistry.* **2020**, *40*, 151-155.

(21) Sakuda, A.; Sato, Y.; Hayashi, A.; Tatsumisago, M. Sulfur-Based Composite Electrode with Interconnected Mesoporous Carbon for All-Solid-State Lithium-Sulfur Batteries. *Energy Technol.* **2019**, *7*, 1900077.

(22) Yi, J. G.; Chen, L.; Liu, Y. C.; Geng, H. X.; Fan, L. Z. High Capacity and Superior Cyclic Performances of All-Solid-State Lithium-Sulfur Batteries Enabled by a High-Conductivity $Li_{10}SnP_2S_{12}$ Solid Electrolyte. *ACS Appl. Mater. Interfaces.* **2019**, *11*, 36774-36781.

(23) Suzuki, K.; Kato, D.; Hara, K.; Yano, T. A.; Hirayama, M.; Hara, M.; Kanno, R. Composite Sulfur Electrode Prepared by High-Temperature Mechanical Milling for use in an All-Solid-State Lithium-Sulfur Battery with a $Li_{3.25}Ge_{0.25}P_{0.75}S_4$ Electrolyte. *Electrochim. Acta.* **2017**, *258*, 110-115.

(24) Wang, H.; Sa, N. Y.; He, M. N.; Liang, X.; Nazar, L. F.; Balasubramanian, M.; Gallagher, K. G.; Key, B. In Situ NMR Observation of the Temporal Speciation of Lithium Sulfur Batteries during Electrochemical Cycling. *J. Phys. Chem. C.* **2017**, *121*, 6011-6017.

(25) Wu, H. L.; Huff, L. A.; Gewirth, A. A. In Situ Raman Spectroscopy of Sulfur Speciation in Lithium-Sulfur Batteries. *ACS Appl. Mater. Interfaces.* **2015**, *7*, 1709-1719.

(26) Zou, Q. L.; Lu, Y. C. Solvent-Dictated Lithium Sulfur Redox Reactions: An

Operando UV-vis Spectroscopic Study. *J. Phys. Chem. Lett.* **2016**, *7*, 1518-1525.

(27)   He, Q.; Freiberg, A. T. S.; Patel, M. U. M.; Qian, S.; Gasteiger, H. A. Operando Identification of Liquid Intermediates in Lithium-Sulfur Batteries via Transmission UV-vis Spectroscopy. *J. Electrochem. Soc.* **2020**, *167*, 080508.

(28)   Barchasz, C.; Molton, F.; Duboc, C.; Lepretre, J. C.; Patoux, S.; Alloin, F. Lithium/Sulfur Cell Discharge Mechanism: An Original Approach for Intermediate Species Identification. *Anal. Chem.* **2012**, *84*, 3973-3980.

(29)   Cuisinier, M.; Cabelguen, P.-E.; Evers, S.; He, G.; Kolbeck, M.; Garsuch, A.; Bolin, T.; Balasubramanian, M.; Nazar, L. F. Sulfur Speciation in Li–S Batteries Determined by Operando X-ray Absorption Spectroscopy. *J. Phys. Chem. Lett.* **2013**, *4*, 3227-3232.

(30)   Cuisinier, M.; Hart, C.; Balasubramanian, M.; Garsuch, A.; Nazar, L. F. Radical or Not Radical: Revisiting Lithium-Sulfur Electrochemistry in Nonaqueous Electrolytes. *Adv. Energy Mater*. **2015**, *5*, 1401801.

(31)   Takeuchi, T.; Kageyama, H.; Nakanishi, K.; Tabuchi, M.; Sakaebe, H.; Ohta, T.; Senoh, H.; Sakai, T.; Tatsumi, K. All-Solid-State Lithium Secondary Battery with Li_2S–C Composite Positive Electrode Prepared by Spark-Plasma-Sintering Process. *J. Electrochem. Soc.* **2010**, *157*, A1196.

(32)   Yamamoto, K.; Zhou, Y.; Yabuuchi, N.; Nakanishi, K.; Yoshinari, T.; Kobayashi, T.; Kobayashi, Y.; Yamamoto, R.; Watanabe, A.; Orikasa, Y.; Tsuruta, K.; Park, J.; Byon, H. R.; Tamenori, Y.; Ohta, T.; Uchimoto, Y. Charge Compensation Mechanism of Lithium-Excess Metal Oxides with Different Covalent and Ionic Characters Revealed by Operando Soft and Hard X-ray Absorption Spectroscopy. *Chem. Mater.* **2020**, *32*, 139-147.

(33)   Xu, R.; Lu, J.; Amine, K. Progress in Mechanistic Understanding and Characterization Techniques of Li-S Batteries. *Adv. Energy Mater*. **2015**, *5*, 1500408.

(34)   Zhang, L.; Qian, T.; Zhu, X. Y.; Hu, Z. L.; Wang, M. F.; Zhang, L. Y.; Jiang, T.; Tian, J. H.; Yan, C. L. In situ optical spectroscopy characterization for optimal design of lithium-sulfur batteries. *Chem. Soc. Rev.* **2019**, *48*, 5432-5453.

(35)   Hayashi, A.; Hama, S.; Morimoto, H.; Tatsumisago, M.; Minami, T. Preparation of Li_2S-P_2S_5 amorphous solid electrolytes by mechanical milling. *J. Am. Ceram. Soc.* **2001**, *84*, 477-479.

(36)   Santhosha, A. L.; Medenbach, L.; Buchheim, J. R.; Adelhelm, P. The Indium-Lithium Electrode in Solid-State Lithium-Ion Batteries: Phase Formation, Redox Potentials, and Interface Stability. *Batteries & Supercaps*. **2019**, *2*, 524-529.

(37)   Takada, K.; Aotani, N.; Iwamoto, K.; Kondo, S. Solid state lithium battery with

oxysulfide glass. *Solid State Ionics*. **1996**, *86-8*, 877-882.

(38)   Gao, J.; Lowe, M. A.; Kiya, Y.; Abruna, H. D. Effects of Liquid Electrolytes on the Charge-Discharge Performance of Rechargeable Lithium/Sulfur Batteries: Electrochemical and in-Situ X-ray Absorption Spectroscopic Studies. *J. Phys. Chem. C*. **2011**, *115*, 25132-25137.

(39)   Li, X.; Banis, M.; Lushington, A.; Yang, X. F.; Sun, Q.; Zhao, Y.; Liu, C. Q.; Li, Q. Z.; Wang, B. Q.; Xiao, W.; Wang, C. H.; Li, M. S.; Liang, J. W.; Li, R. Y.; Hu, Y. F.; Goncharova, L.; Zhang, H. M.; Sham, T. K.; Sun, X. L. A high-energy sulfur cathode in carbonate electrolyte by eliminating polysulfides via solid-phase lithium-sulfur transformation. *Nat. Commun.* **2018**, *9*, 4509.

(40)   Hakari, T.; Deguchi, M.; Mitsuhara, K.; Ohta, T.; Saita, K.; Orikasa, Y.; Uchimoto, Y.; Kowada, Y.; Hayashi, A.; Tatsumisago, M. Structural and Electronic-State Changes of a Sulfide Solid Electrolyte during the Li Deinsertion-Insertion Processes. *Chem. Mater.* **2017**, *29*, 4768-4774.

(41)   Yim, T.; Park, M. S.; Yu, J. S.; Kim, K. J.; Im, K. Y.; Kim, J. H.; Jeong, G.; Jo, Y. N.; Woo, S. G.; Kang, K. S.; Lee, I.; Kim, Y. J. Effect of chemical reactivity of polysulfide toward carbonate-based electrolyte on the electrochemical performance of Li-S batteries. *Electrochim. Acta*. **2013**, *107*, 454-46 0.

(42)   Chen, K.; Shinjo, S.; Sakuda, A.; Yamamoto, K.; Uchiyama, T.; Kuratani, K.; Takeuchi, T.; Orikasa, Y.; Hayashi, A.; Tatsumisago, M.; Kimura, Y.; Nakamura, T.; Amezawa, K.; Uchimoto, Y. Morphological Effect on Reaction Distribution Influenced by Binder Materials in Composite Electrodes for Sheet-type All-Solid-State Lithium-Ion Batteries with the Sulfide-based Solid Electrolyte. *J. Phys. Chem. C*. **2019**, *123*, 3292-3298.

(43)   Richards, W. D.; Miara, L. J.; Wang, Y.; Kim, J. C.; Ceder, G. Interface Stability in Solid-State Batteries. *Chem. Mater.* **2016**, *28*, 266-273.

(44)   Barchasz, C.; Lepretre, J. C.; Patoux, S.; Alloin, F. Electrochemical properties of ether-based electrolytes for lithium/sulfur rechargeable batteries. *Electrochim. Acta*. **2013**, *89*, 737-743.

(45)   Li, G. R.; Wang, S.; Zhang, Y. N.; Li, M.; Chen, Z. W.; Lu, J. Revisiting the Role of Polysulfides in Lithium-Sulfur Batteries. *Adv. Mater.* **2018**, *30*, 1705590.

Chapter 3 Reaction mechanism of microporous carbon-supported sulfur cathodes revealed by *operando* soft X-ray absorption spectroscopy

Sulfur is a promising material for next-generation cathodes, owing to its high energy and low cost. However, sulfur cathodes have the disadvantage of serious cyclability issues due to the dissolution of polysulfides that form as an intermediate product during discharge/charge cycling. Filling sulfur into the micropores of porous carbon is an effective method to suppress its dissolution. Although microporous carbon-supported sulfur cathodes show an electrochemical behavior different from that of the conventional sulfur ones, the corresponding reaction mechanism is not clearly understood. In this study, we focused on clarifying the reaction mechanism of microporous carbon-supported sulfur cathodes by *operando* soft X-ray absorption spectroscopy. In the microporous carbon support, sulfur was present as smaller fragments compared to conventional sulfur. During the first discharge process, the sulfur species in the microporous carbon were initially reduced to S_6^{2-} and S_2^{2-} and then to Li_2S. The S_6^{2-} and S_2^{2-} species were observed first, with S_2^{2-} being the main polysulfide species during the discharge process, while Li_2S was produced in the final discharge process. The narrow pores of microporous carbon prevent the dissolution of polysulfides and influence the reaction mechanism of sulfur cathodes.

3.1 Introduction

With the rapid development of electronic equipment and energy-storage devices, the demand for high-energy storage systems has become increasingly urgent and important. Sulfur cathodes have received much attention because of their high theoretical specific capacity (1672 mAh/g), low cost, high availability, and environment-friendliness.[1-4] Therefore, sulfur cathodes are considered as promising components of next-generation energy-storage systems.[5-8] However, current sulfur cathodes possess many disadvantages that prevent their rapid development. One of the most serious disadvantages is the high solubility of lithium polysulfides (Li_2S_n, n = 4–8) formed during the charging and discharging processes.[9-11] The dissolution of polysulfides leads to a low coulombic efficiency and rapid capacity degradation of batteries.[12-14]

Filling sulfur into microporous carbon is a promising method to overcome the dissolution problem caused by the high solubility of the polysulfide species in liquid electrolytes.[15-20] In the microporous carbon-supported sulfur cathode, the dissolution of polysulfides is suppressed because the solvent does not come into contact with sulfur.[21-23] Although this approach is effective in suppressing the polysulfide dissolution, the microporous carbon-supported sulfur cathodes show an electrochemical behavior different from that of their conventional sulfur counterparts, especially in the first discharge process.[15, 17] The conventional sulfur cathode shows two plateaus at approximately 2.4 and 2.1 V vs. Li/Li+ during the first discharge process.[11, 16] During the first discharge plateau, the cyclic S_8 molecules are reduced to long-chain lithium polysulfides (Li_2S_n, $4 \leq n < 8$) through a disproportionation reaction, and the latter species are further reduced to short-chain lithium polysulfides (Li_2S_n, $1 < n < 4$) and Li_2S during the

second longer discharge plateau.[24-27] In contrast to the conventional sulfur cathode, the microporous carbon-supported sulfur cathode shows a single discharge plateau (~1.8 V vs. Li/Li+) during the first discharge process.[15, 18] To design a microporous carbon-supported sulfur cathode with high electrochemical performance, it is necessary to understand the reaction mechanism of the corresponding electrodes.

Various spectroscopic techniques such as X-ray photoemission spectroscopy (XPS)[28] and X-ray absorption spectroscopy[29] (XAS) have been employed to investigate the reaction mechanism of microporous carbon-supported sulfur cathodes. Helen et al. showed that on the surface and subsurface for the microporous carbon-supported sulfur cathode during first discharge by XPS, long-chain polysulfide could not be detected and only Li_2S_2 and Li_2S could be detected.[28] They proposed a direct transformation from sulfur to Li_2S_2/Li_2S during first discharge in the system.[28] On the other hand, Dominko et al. observed that a mixture of long chain polysulfide (S_8^{2-} and S_6^{2-}) and a mixture of short chain polysulfides (S_4^{2-} and S_2^{2-}) by operando XAS and suggested the transformation from the long-chain polysulfide to short-chain polysulfides and Li_2S.[29] However, thus far, no quantitative studies of the reaction mechanism have been reported. In this study, the reaction pathway of the microporous-supported sulfur cathodes was examined by the *operando* XAS analysis, which is a powerful technique to quantitatively evaluate the sulfur species formed during discharge/charge processes.[30, 31]

3.2 Experimental Section

3.2.1 Materials

A microporous carbon-supported cathode was prepared using the procedure reported previously.[32] After mixing sulfur (Wako Co.) and microporous carbon (Toyobo Co.), the mixture was heated to 155 °C for approximately 5 h to allow sulfur to diffuse into the microporous carbon. Finally, the temperature was increased to 300 °C and maintained for 2 h to sublime the extra sulfur on the outer surface of the microporous carbon. Sulfur, Li_2S_6, Na_2S_4, Na_2S_2 and Li_2S were used for the references of XAS. Li_2S_6 was synthesized through the previously reported procedure.[26] Stoichiometric ratio of sulfur and 1 M lithium triethylborohydride / tetrahydrofuran (3:1mol%) was stirred for 1 hour and then the solvent was removed under vacuum inside Ar-filled glovebox. Na_2S_4 and Na_2S_2 were purchased from Dojindo Molecular Technologies Inc. Sulfur and Li_2S were purchased from Aldrich Co.

3.2.2 Characterizations

The particle morphology of the microporous carbon was observed by transmission electron microscopy (TEM, JEM-2100F, JEOL) and scanning electron microscopy (SEM, SU-1500, Hitachi). The amount of sulfur in the microporous carbon was determined by thermogravimetric analysis (TGA) (DTG-60AH, Shimadzu) under an Ar atmosphere at a heating rate of 5 °C/min. N_2 adsorption and desorption isotherms were measured at -196 °C using Autosorbμ-iQ (Quantachrome).

3.2.3 Electrochemical testing

The electrochemical performance of the microporous carbon-supported sulfur cathode was examined using a two-electrode cell. A composite cathode was prepared by mixing the microporous carbon-supported sulfur cathode, acetylene

black, and alginic acid binder in 90:5:5 weight ratio, supported by carbon paper. Li foil was used as the counter electrode. 1 M lithium bis(trifluorosulfonyl)amide (LiTFSA) / fluoroethylene carbonate (FEC):1,1,2,2-tetrafluoroethyl-2,2,3,3 tetrafluoropropyl ether (hydrofluoroether, HFE), in which the ratio of FEC to HFE was 1:1 vol% and the quantity of the electrolyte was 700 μL, was used as the electrolyte in a glass fiber membrane separator. The two-electrode cells were assembled in a glovebox filled with Ar. Galvanostatic charge/discharge measurements were carried out at a current density of 0.1 C (1 C = 1672 mAh/g) with cut-off voltages of 1.0 V for the discharge and 3.0 V for the charge process at 25 °C.

3.2.4 XAFS measurements

S K-edge *operando* XAS spectra of the microporous carbon-supported sulfur cathode were observed in the partial fluorescence yield (PFY) mode at the BL27SU beamline of the SPring-8 synchrotron radiation facility at Hyogo, Japan. A homemade cell[33] was used for the *operando* XAS. The microporous carbon-supported sulfur cathode composite material was mounted on a polyimide film to serve as the working electrode. LiTFSA/FEC:HFE was used in a glass fiber membrane as the electrolyte solution, and Li foil was used as the counter electrode. The *operando* cell was assembled in an argon-filled glovebox and transferred into a chamber for the XAS measurements under ultrahigh vacuum. The *operando* XAS measurements were performed under galvanostatic discharge at 0.1 C.

3.3 Result and discussion

The SEM and TEM images of microporous carbon are shown in Figure 3.1 (a) and (b), respectively. The SEM image showed the particle size was 1-2 µm and the TEM image showed that the microporous carbon has amorphous structure with pore of ~ 1 nm. The polar size distribution of the microporous carbon support was also confirmed by N_2 adsorption measurements, as shown in Figure 3.2, which showed a pore size of ~ 1 nm. The TGA (Figure 3.3) showed a weight loss of approximately 24% at ~ 450 °C for the microporous carbon-supported sulfur, indicating that the sulfur content was ~ 24%.

The microporous carbon-supported sulfur cathode showed a discharge capacity of 2380 mAh/g, with a long single plateau at a voltage of ~ 1.4 V in the first discharge process and a charge capacity of 900 mAh/g (Figure. 3.4a). After the first discharge/charge cycle, the microporous carbon-supported sulfur cathode showed a different discharge curve, with a reversible capacity of 900 mAh/g and a high coulombic efficiency (Figure. 3.4b). A large irreversible discharge capacity, exceeding the theoretical capacity of sulfur (1672 mAh/g), was also observed in previous reports.[17, 21, 28, 32, 34] This phenomenon is due to the formation of a solid electrolyte interphase (SEI) layer on the electrode composite.[23, 35]

To examine the electronic structure of the pristine microporous-supported sulfur cathode, we performed ex situ S K-edge XAS measurements for the microporous carbon-supported sulfur and ring-like sulfur cathodes. The S K-edge XANES and EXAFS results are presented in Figure. 3.5a and 3.5b, respectively. The two sulfur samples showed an absorption feature at 2471.8 eV, which was attributed to the S 1s to S–S π*[36] state transition of elemental sulfur (Figure. 3.5a). However, the absorption

peak intensity of the microporous carbon-supported sulfur cathode was lower than that of conventional sulfur, indicating that the transition from S 1s to S–S π* was reduced in the former sample. In the Fourier-transformed EXAFS spectra (Figure. 3.5b), the intensity of the peak at 1.6 Å, attributed to the S–S bonds, was lower for the microporous carbon-supported sulfur cathode than that for the conventional sulfur sample. This result indicates a decrease in the coordination number of S–S bonds in the microporous carbon-supported sulfur sample compared to that in conventional sulfur. Since sulfur in microporous carbons has been reported by X-ray photo emission spectroscopy[17] and electron energy loss spectroscopy[21] to be present in a chain rather than a ring structure, the present XAS results imply that sulfur changed from a ring to a chain structure after melting into the microporous carbon.

Operando XAS measurements were conducted to examine the electrochemical structural changes of the microporous carbon-supported sulfur cathode (Figure. 3.6a). Before the discharge process, absorption peaks were observed at 2472 and 2480 eV. The peak at 2472 eV is attributed to sulfur, as observed in Figure. 3.5, whereas that at 2480 eV corresponds to the sulfur component of the LiTFSA compound in the electrolyte.[25, 37] During the discharge process, an absorption peak attributed to linear polysulfides appeared at 2470 eV;[36] then, two new peaks attributed to Li_2S were observed at 2472.8 and 2475.2 eV.

Linear combination fitting (LCF)[26] was performed to estimate the ratio of the sulfur components during the discharge process (Figure. 3.6b). The spectra of pristine microporous carbon-supported sulfur S_8, long-chain polysulfides S_6^{2-}, medium/long-chain lithium polysulfides S_4^{2-}, short-chain polysulfides S_2^{2-}, and Li_2S were used as references for the LCF analysis. The obtained fitting results were shown in Figure. 3.7. Although these references were not exactly corresponding to polysulfide species

forming during discharge process, they are useful to discuss the ratio change of polysulfide species.[25, 26] The polysulfide species S_6^{2-} and S_2^{2-} were formed in the initial stage, with a corresponding decrease in the amount of S_8 species, whereas in the intermediate stage, the amounts of S_2^{2-} and Li_2S increased and those of S_8 and S_6^{2-} decreased. In the final stage, the analysis showed an increase in the Li_2S amount and a decrease in the amounts of S_8 and S_2^{2-}. Unreacted S_8 and S_2^{2-} species were present even in the discharge state, that is, above the theoretical capacity of sulfur (1672 mAh/g).

The lithium content calculated by the LCF analysis (Figure. 3.6c) increased in the x range of 0–3.0, but its value was lesser than that estimated by electrochemical measurements, and it was lesser than 2.0 even in the final discharge state (x = 3.0). These results indicate the decomposition of the electrolyte and the presence of unreacted sulfur species. It has been reported that the FEC solvent undergoes decomposition at 1.5 V[35] on the surface of the microporous carbon. In the microporous carbon-supported sulfur cathode, lithium-ion transport to the sulfur is sluggish compared to conventional sulfur cathode because the electrolyte cannot enter the micropores.[17] Therefore, lithium-ion conduction becomes the rate-limiting step, and the sulfur species located deep inside the micropores remain unreacted. A similar reaction distribution was observed in all-solid-state battery systems,[38] in which the reaction proceeds from the solid electrolyte side because ionic conduction is slower than electronic conduction.

The reaction mechanism of the microporous carbon-supported sulfur cathode during discharge is illustrated in Figure. 3.8. In the initial stage, sulfur forms chain structures inside the micropores. In the intermediate stage of discharge, S_6^{2-} and S_2^{2-} polysulfides are formed because the solvent cannot enter the micropores, and these polysulfides do not dissolve in the liquid electrolyte. In the final discharge process, Li_2S is the main

sulfide species, with residual amounts of S_2^{2-} and long-chain S_8 species inside the micropores.

The microporous carbon can prevent the dissolution of polysulfides in the liquid electrolyte, resulting in a change in the sulfur cathode reaction pathway. This change leads to a single plateau at approximately 1.4 V during the first discharge, as observed in the solid electrolyte.

3.4 Conclusions

In this study, the reaction mechanism of the sulfur cathode in the microporous carbon during discharge was observed by operando XAS. The sulfur cathode was reduced to long-chain (S_6^{2-}) and short-chain (S_2^{2-}) polysulfide species during the initial discharge, while the short-chain S_2^{2-} units were the main polysulfide species in the subsequent discharge; large amounts of Li_2S were formed during the final discharge. The reaction mechanism of the microporous carbon-supported sulfur cathode is different from that of a conventional sulfur cathode, as the microporous carbon support prevents the dissolution of polysulfides. This study elucidated the reaction mechanism of sulfur cathodes in microporous carbon by operando soft XAS. We believe that our results can provide further insights into the deeper understanding of the behavior of sulfur in carbon-supported cathodes, and it will be helpful for designing new cathodes with high performance.
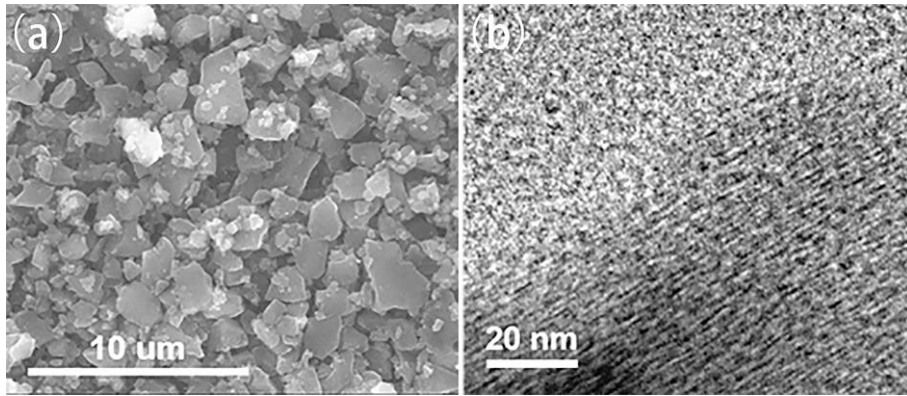
Figure 3.1. (a) SEM and (b) TEM images of microporous carbon.
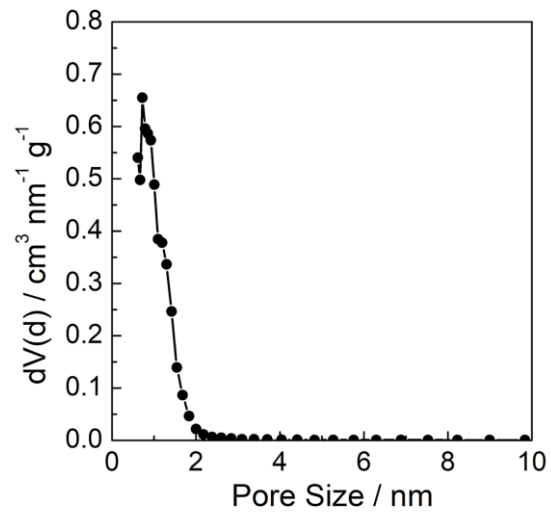
Figure 3.2. Pore size distribution of the microporous carbon obtained by N_2 adsorption isotherm measurement at -196 °C.
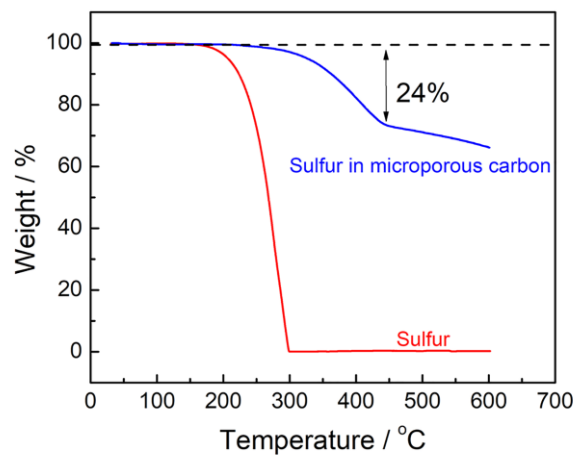
Figure 3.3. Thermogravimetric analysis curves of sulfur and microporous carbon-supported sulfur under an Ar atmosphere at a heating rate of 5 °C/min.
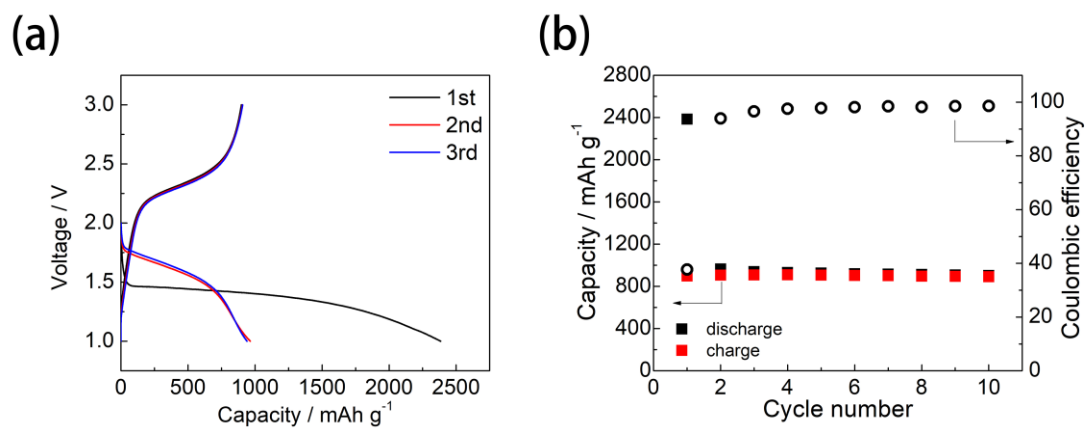
Figure 3.4. Charge/discharge profile (a) and cycle performance (b) of the microporous carbon-supported sulfur cathode.
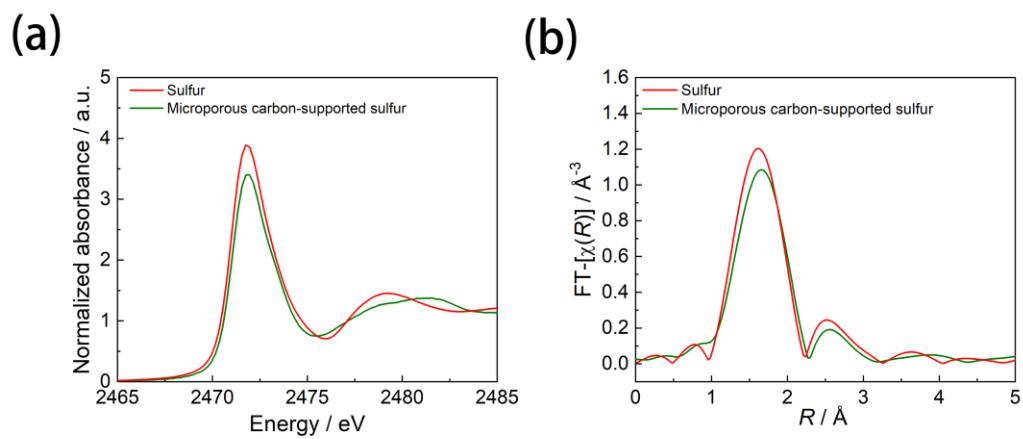
Figure 3.5. (a) S K-edge XANES profiles and (b) S K-edge Fourier-transformed EXAFS profiles obtained from XAS measurements for sulfur and microporous carbon-supported sulfur cathodes.
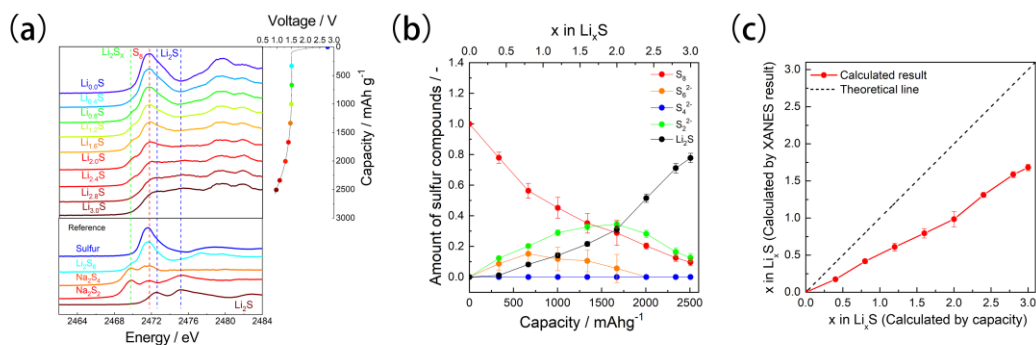
Figure 3.6. (a) Sulfur K-edge XANES spectra obtained from the operando XAS measurements of the microporous carbon-supported sulfur cathode. (b) Sulfur compound ratio of the microporous carbon-supported sulfur cathode during the first discharge, calculated by the linear combination fitting (LCF) analysis of XANES spectra. (c) Lithium compositions calculated from the LCF analysis and electrochemical capacity data.
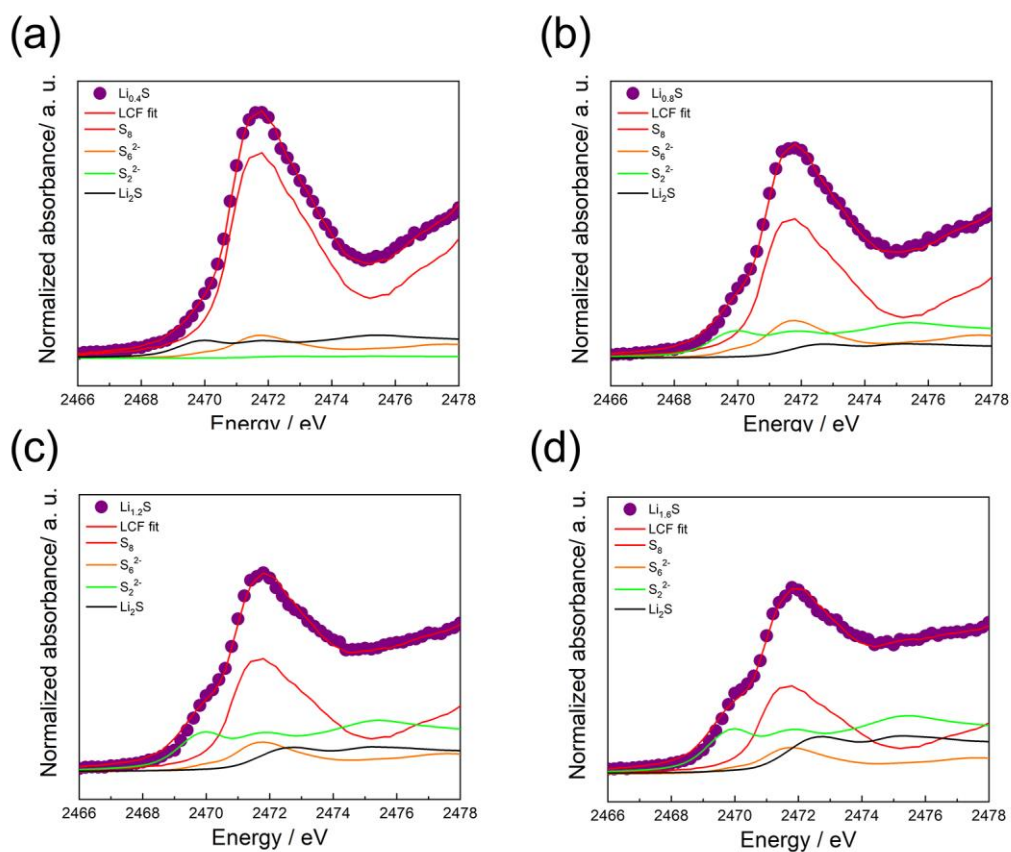
Figure 3.7. Linear combination fitting result of sulfur *K*-edge XANES of microporous carbon-supported sulfur cathode at discharge state of $Li_{0.4}S$, $Li_{0.8}S$, $Li_{1.2}S$ and $Li_{1.6}S$.
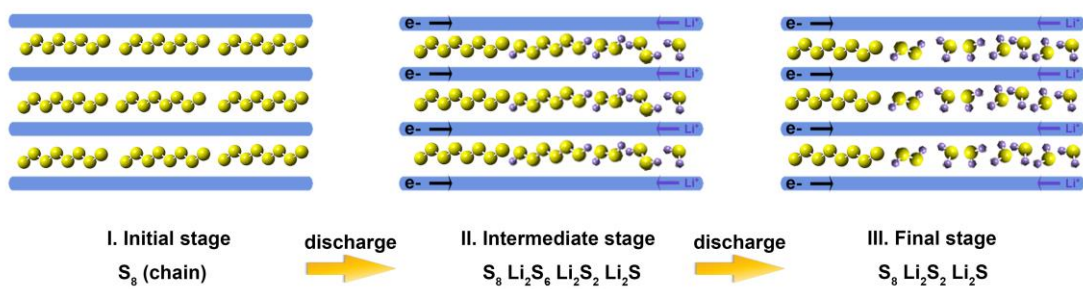
Figure 3.8. Reaction model for the microporous carbon-supported sulfur cathodes.

Reference

(1)   Zhou, G.; Yin, L.-C.; Wang, D.-W.; Li, L.; Pei, S.-F.; Gentle, I. R.; Li, F.; Cheng, H.-M. Fibrous Hybrid of Graphene and Sulfur Nanocrystals for High-Performance Lithium-Sulfur Batteries. *ACS Nano*. **2013**, *7*, 5367-5375.

(2)   Ellis, B. L.; Lee, K. T.; Nazar, L. F. Positive Electrode Materials for Li-Ion and Li-Batteries†. *Chem. Mater.* **2010**, *22*, 691-714.

(3)   Bruce, P. G.; Freunberger, S. A.; Hardwick, L. J.; Tarascon, J. M. Li-O_2 and Li-S batteries with high energy storage. *Nat. Mater.* **2011**, *11*, 19-29.

(4)   Evers, S.; Nazar, L. F. New Approaches for High Energy Density Lithium-Sulfur Battery Cathodes. *Acc. Chem. Res.* **2013**, *46*, 1135-1143.

(5)   Yin, Y.-X.; Xin, S.; Guo, Y.-G.; Wan, L.-J. Lithium-sulfur batteries: electrochemistry, materials, and prospects. *Angew. Chem., Int. Ed.* **2013**, *52*, 13186-200.

(6)   Manthiram, A.; Fu, Y.; Chung, S.-H.; Zu, C.; Su, Y.-S. Rechargeable lithium-sulfur batteries. *Chem. Rev.* **2014**, *114*, 11751-11787.

(7)   Pang, Q.; Liang, X.; Kwok, C. Y.; Nazar, L. F. Advances in lithium–sulfur batteries based on multifunctional cathodes and electrolytes. *Nat. Energy*. **2016**, *1*, 16132.

(8)   Seh, Z. W.; Sun, Y.; Zhang, Q.; Cui, Y. Designing high-energy lithium-sulfur batteries. *Chem. Soc. Rev.* **2016**, *45*, 5605-5634.

(9)   Vijayakumar, M.; Govind, N.; Walter, E.; Burton, S. D.; Shukla, A.; Devaraj, A.; Xiao, J.; Liu, J.; Wang, C.; Karim, A.; Thevuthasan, S. Molecular structure and stability of dissolved lithium polysulfide species. *Phys. Chem. Chem. Phys.* **2014**, *16*, 10923-32.

(10)   Zhang, S. S. Liquid electrolyte lithium/sulfur battery: Fundamental chemistry, problems, and solutions. *J. Power Sources*. **2013**, *231*, 153-162.

(11)   Lin, Z.; Liang, C. Lithium–sulfur batteries: from liquid to solid cells. *J. Mater. Chem. A*. **2015**, *3*, 936-958.

(12)   Zheng, G. Y.; Yang, Y.; Cha, J. J.; Hong, S. S.; Cui, Y. Hollow Carbon Nanofiber-Encapsulated Sulfur Cathodes for High Specific Capacity Rechargeable Lithium Batteries. *Nano Lett.* **2011**, *11*, 4462-4467.

(13)   Ji, X. L.; Nazar, L. F. Advances in Li-S batteries. *J. Mater. Chem.* **2010**, *20*, 9821-9826.

(14)   Ji, X. L.; Evers, S.; Black, R.; Nazar, L. F. Stabilizing lithium-sulphur cathodes using polysulphide reservoirs. *Nat. Commun.* **2011**, *2*.

(15)   Zhang, B.; Qin, X.; Li, G. R.; Gao, X. P. Enhancement of long stability of sulfur cathode by encapsulating sulfur into micropores of carbon spheres. *Energy*

Environ. Sci. **2010**, *3*, 1531-1537.

(16) Xin, S.; Gu, L.; Zhao, N. H.; Yin, Y. X.; Zhou, L. J.; Guo, Y. G.; Wan, L. J. Smaller Sulfur Molecules Promise Better Lithium-Sulfur Batteries. *J. Am. Chem. Soc.* **2012**, *134*, 18510-18513.

(17) Li, Z.; Yuan, L. X.; Yi, Z. Q.; Sun, Y. M.; Liu, Y.; Jiang, Y.; Shen, Y.; Xin, Y.; Zhang, Z. L.; Huang, Y. H. Insight into the Electrode Mechanism in Lithium-Sulfur Batteries with Ordered Microporous Carbon Confined Sulfur as the Cathode. *Adv. Energy Mater.* **2014**, *4*, 1301473.

(18) Li, Z.; Jiang, Y.; Yuan, L. X.; Yi, Z. Q.; Wu, C.; Liu, Y.; Strasser, P.; Huang, Y. H. A Highly Ordered Meso@Microporous Carbon-Supported Sulfur@Smaller Sulfur Core-Shell Structured Cathode for Li-S Batteries. *ACS Nano*. **2014**, *8*, 9295-9303.

(19) Peng, Z. H.; Fang, W. Y.; Zhao, H. B.; Fang, J. H.; Cheng, H. W.; Doan, T. N. L.; Xu, J. Q.; Chen, P. Graphene-based ultrathin microporous carbon with smaller sulfur molecules for excellent rate performance of lithium-sulfur cathode. *J. Power Sources*. **2015**, *282*, 70-78.

(20) Xu, Y. H.; Wen, Y.; Zhu, Y. J.; Gaskell, K.; Cychosz, K. A.; Eichhorn, B.; Xu, K.; Wang, C. S. Confined Sulfur in Microporous Carbon Renders Superior Cycling Stability in Li/S Batteries. *Adv. Funct. Mater.* **2015**, *25*, 4312-4320.

(21) Helen, M.; Diemant, T.; Schindler, S.; Behm, R. J.; Danzer, M.; Kaiser, U.; Fichtner, M.; Reddy, M. A. Insight into Sulfur Confined in Ultramicroporous Carbon. *ACS Omega*. **2018**, *3*, 11290-11299.

(22) Niu, S. Z.; Zhou, G. M.; Lv, W.; Shi, H. F.; Luo, C.; He, Y. B.; Li, B. H.; Yang, Q. H.; Kang, F. Y. Sulfur confined in nitrogen-doped microporous carbon used in a carbonate-based electrolyte for long-life, safe lithium-sulfur batteries. *Carbon*. **2016**, *109*, 1-6.

(23) Markevich, E.; Salitra, G.; Rosenman, A.; Talyosef, Y.; Chesneau, F.; Aurbach, D. The effect of a solid electrolyte interphase on the mechanism of operation of lithium-sulfur batteries. *J. Mater. Chem. A*. **2015**, *3*, 19873-19883.

(24) Zheng, D.; Wang, G.; Liu, D.; Si, J.; Ding, T.; Qu, D.; Yang, X.; Qu, D. The Progress of Li-S Batteries-Understanding of the Sulfur Redox Mechanism: Dissolved Polysulfide Ions in the Electrolytes. *Adv. Mater. Technol*. **2018**, *3*, 1700233.

(25) Cuisinier, M.; Cabelguen, P.-E.; Evers, S.; He, G.; Kolbeck, M.; Garsuch, A.; Bolin, T.; Balasubramanian, M.; Nazar, L. F. Sulfur Speciation in Li–S Batteries Determined by Operando X-ray Absorption Spectroscopy. *J. Phys. Chem. Lett.* **2013**, *4*, 3227-3232.

(26) Cuisinier, M.; Hart, C.; Balasubramanian, M.; Garsuch, A.; Nazar, L. F. Radical

or Not Radical: Revisiting Lithium-Sulfur Electrochemistry in Nonaqueous Electrolytes. *Adv. Energy Mater*. **2015**, *5*, 1401801.

(27) Li, G. R.; Wang, S.; Zhang, Y. N.; Li, M.; Chen, Z. W.; Lu, J. Revisiting the Role of Polysulfides in Lithium-Sulfur Batteries. *Adv. Mater.* **2018**, *30*, 1705590.

(28) Helen, M.; Reddy, M. A.; Diemant, T.; Golla-Schindler, U.; Behm, R. J.; Kaiser, U.; Fichtner, M. Single step transformation of sulphur to Li_2S_2/Li_2S in Li-S batteries. *Sci. Rep.* **2015**, *5*, 12146.

(29) Dominko, R.; Vizintin, A.; Aquilanti, G.; Stievano, L.; Helen, M. J.; Munnangi, A. R.; Fichtner, M.; Arcon, I. Polysulfides Formation in Different Electrolytes from the Perspective of X-ray Absorption Spectroscopy. *J. Electrochem. Soc.* **2018**, *165*, A5014-A5019.

(30) Xu, R.; Lu, J.; Amine, K. Progress in Mechanistic Understanding and Characterization Techniques of Li-S Batteries. *Adv. Energy Mater*. **2015**, *5*, 1500408.

(31) Zhang, L.; Qian, T.; Zhu, X. Y.; Hu, Z. L.; Wang, M. F.; Zhang, L. Y.; Jiang, T.; Tian, J. H.; Yan, C. L. In situ optical spectroscopy characterization for optimal design of lithium-sulfur batteries. *Chem. Soc. Rev.* **2019**, *48*, 5432-5453.

(32) Takahashi, T.; Yamagata, M.; Ishikawa, M. A sulfur-microporous carbon composite positive electrode for lithium/sulfur and silicon/sulfur rechargeble batteries. *Prog. Nat. Sci.: Mater. Int.* **2015**, *25*, 612-621.

(33) Yamamoto, K.; Zhou, Y. Y.; Yabuuchi, N.; Nakanishi, K.; Yoshinari, T.; Kobayashi, T.; Kobayashi, Y.; Yamamoto, R.; Watanabe, A.; Orikasa, Y.; Tsuruta, K.; Park, J.; Byon, H. R.; Tamenori, Y.; Ohta, T.; Uchimoto, Y. Charge Compensation Mechanism of Lithium-Excess Metal Oxides with Different Covalent and Ionic Characters Revealed by Operando Soft and Hard X-ray Absorption Spectroscopy. *Chem. Mater.* **2020**, *32*, 139-147.

(34) Zhang, W. H.; Qiao, D.; Pan, J. X.; Cao, Y. L.; Yang, H. X.; Ai, X. P. A Li+-conductive microporous carbon-sulfur composite for Li-S batteries. *Electrochim. Acta*. **2013**, *87*, 497-502.

(35) Markevich, E.; Salitra, G.; Rosenman, A.; Talyosef, Y.; Chesneau, F.; Aurbach, D. Fluoroethylene carbonate as an important component in organic carbonate electrolyte solutions for lithium sulfur batteries. *Electrochem. Commun.* **2015**, *60*, 42-46.

(36) Li, X.; Banis, M.; Lushington, A.; Yang, X. F.; Sun, Q.; Zhao, Y.; Liu, C. Q.; Li, Q. Z.; Wang, B. Q.; Xiao, W.; Wang, C. H.; Li, M. S.; Liang, J. W.; Li, R. Y.; Hu, Y. F.; Goncharova, L.; Zhang, H. M.; Sham, T. K.; Sun, X. L. A high-energy sulfur cathode in carbonate electrolyte by eliminating polysulfides via solid-phase lithium-sulfur transformation. *Nat. Commun.* **2018**, *9*, 4509.

(37)   Lee, C. W.; Pang, Q.; Ha, S.; Cheng, L.; Han, S. D.; Zavadil, K. R.; Gallagher, K. G.; Nazar, L. F.; Balasubramanian, M. Directing the Lithium-Sulfur Reaction Pathway via Sparingly Solvating Electrolytes for High Energy Density Batteries. *ACS Cent. Sci*. **2017**, *3*, 605-613.

(38)   Chen, K.; Shinjo, S.; Sakuda, A.; Yamamoto, K.; Uchiyama, T.; Kuratani, K.; Takeuchi, T.; Orikasa, Y.; Hayashi, A.; Tatsumisago, M.; Kimura, Y.; Nakamura, T.; Amezawa, K.; Uchimoto, Y. Morphological Effect on Reaction Distribution Influenced by Binder Materials in Composite Electrodes for Sheet-type All-Solid-State Lithium-Ion Batteries with the Sulfide-based Solid Electrolyte. *J. Phys. Chem. C*. **2019**, *123*, 3292-3298.

Chapter 4 Li₂S-V₂S₃-LiI as electrode active materials with high ionic and electronic conductivities for all-solid-state Li-S batteries

Composite electrodes consisting of active materials, carbon, solid electrolytes (SEs), and binders are widely used for all-solid-state lithium batteries to achieve a more efficient reaction site and improve storage capacity for practical use. The fraction of active material in all-solid-state batteries is small because the amount of added SE required to form a ion conduction pathway in composite electrodes is large. This leads to a decrease in pack density of the active material, which, subsequently, reduces the energy density of the battery. The Li₂S–V₂S₃–LiI electrode active materials doped with different LiI amounts developed in this study presented a high charge-discharge capacity in the absence of an SE and carbon in the electrode. Moreover, the Li₂S–V₂S₃–LiI electrode active materials presented high electronic conductivity, and their ionic conductivity increased with increasing LiI doping amount. The optimized 90 mol% (0.75Li₂S–0.25V₂S₃)–10 mol% LiI cathode presented the highest discharge capacity of 526 mAh g^{-1} of all cathodes in this study. The reaction mechanism of the electrode active materials was elucidated using a combination of analytical methods, such as electrochemical measurements, soft X-ray absorption spectroscopy(XAS) of the V L-edge and S K-edge, and X-ray computed tomography (CT). Potential step

measurements revealed that LiI doping amounts above 10 mol% largely increased the ionic conductivity of the Li_2S–V_2S_3–LiI cathodes during charging. The soft XAS results indicated that hole formed in the S-3p orbital during the entire charge process and in the V-3d orbital in the potential range of 0-1.5 V after the first charge cycle. The X-ray CT results demonstrated that LiI rich domain formed from the Li_2S–V_2S_3–LiI cathode during charging because the lithium content of the cathode material changed. These results indicated that self-forming LiI rich domain served as an ionic conduction pathway in the cathode matrix during the first charge cycle and improved the electrochemical performance of the cathode materials.

4.1 Introduction

All-solid-state lithium-ion secondary batteries using sulfide solid electrolytes (SEs) are very safe because liquid leakage is eliminated; moreover, they have possibility to present high charge–discharge rates.[1-6] Several oxides and sulfides have been studied as cathode active materials for all-solid-state lithium-ion secondary batteries.[7-15] Among them, transition metal sulfides, such as SeS,[15] FeS,[14] CuS,[16] Li$_2$S-Cu,[13] and Li$_2$TiS$_3$[17] have attracted increasing attention as cathode materials because of their high capacity and low reactivity with sulfide SEs.[17-20] In addition, these cathode materials present higher electronic conductivity than sulfur and Li$_2$S; moreover, they do not require a large amount of carbon as conductive material for composite electrodes, which results in a high weight energy density.

To improve the energy density of all-solid-state batteries it is important to improve the capacity of the active material and the packing density of the active material in the composite electrode. Because in the composite electrodes of all-solid-state batteries when ordinary transition metal oxides or sulfides are used as active materials, ionic rather than electronic conduction is the rate-limiting factor,[21] and a large amount of SE should be added to the composite electrode to ensure that a sufficient ionic pathway exists in the active material.[22] The large amount of SE required to form the ionic

pathway results in the low weight energy density of the composite electrode. Two approaches have been used to reduce the amount of the electrolyte in and improve the weight energy density of composite electrodes: (1) improving the ionic conductivity of the SE[23-25] and (2) controlling the dispersion of the SE in the composite electrode.[26, 27] Several SE with high ionic conductivity, such as Li_3PS_4,[28] $Li_{3.25}Ge_{0.25}P_{0.75}S_4$,[29] $Li_7P_3S_{11}$,[30] $Li_{10}GeP_2S_{12}$,[31] and $Li_{9.54}Si_{1.74}P_{1.44}S_{11.7}Cl_{0.3}$[5] have been developed, and different techniques have been used to fabricate composite electrodes using a liquid phase to control the dispersion state of the SE in the composite electrode.[32-36] However, these approaches have not allowed to significantly reduce the amount of SE in the composite electrode.

In this study, we demonstrated that Li_2S–V_2S_3–LiI electrode active materials presented excellent capacity ionic conductivity and rate performance even when no SE was added to the composite electrode. The charge compensation mechanism of Li_2S–V_2S_3–LiI was analyzed using soft X-ray absorption spectroscopy (XAS). In addition, by analyzing the morphology of the electrode material after charging using X-ray computed tomography (CT), it was determined that a high ionic conduction phase containing LiI with high-rate characteristics was formed in the electrode. This material design based on the self-formation of an ion conduction pathway in the composite electrode during charging can provide a guideline for designing high-packing-density

electrodes for all-solid-state batteries in the future.

4.2 Experimental Section

4.2.1   Preparation of samples

The $(100-x)(0.75Li_2S–0.25V_2S_3)–xLiI$ (x = 0, 5, 10, and 20) samples in this study were prepared using ball milling. Stoichiometric amounts of Li_2S (99% purity, Mitsuwa), V_2S_3 (99% purity, Kojundo), and LiI (99% purity, Aldrich) were hand-mixed in a mortar for 30 min, followed by mechanical mixing with ZrO_2 balls at 530 rpm for 80 h. The Li_3PS_4 glass powder used to fabricate the SE was prepared via ball milling using a previously reported procedure, as follows. Li_2S (99% purity, Aldrich) and P_2S_5 (99% purity, Aldrich) powders with a 3:1 molar ratio were mechanically mixed using ZrO_2 balls at 370 rpm for 30 h.[37] All experiments were performed in a dry Ar-filled glovebox.

4.2.2   Characterization

The synchrotron X-ray diffraction (XRD) profiles of the as-prepared $(100-x)(0.75Li2S–0.25V2S3)–xLiI$ (x = 0, 5, 10, and 20) cathode materials were obtained at the BL5S2 beamline of the Aichi Synchrotron Radiation Center, Japan. The scanning electron microscopy (SEM) images and energy dispersive X-ray spectroscopy (EDX) profiles of the as-prepared $(100-x)(0.75Li_2S–0.25V_2S_3)–xLiI$ (x = 0, 5, 10, and 20) were recorded using a JSM-6610A (JEOL) field-emission scanning electron microscopy

device.

The XAS spectra of the S K-edge and V L-edge of the cathode materials were recorded at the BL6N1 beamline of the Aichi Synchrotron Radiation Center, Japan and BL27SU beamline of the SPring-8 Synchrotron Radiation Facility, Hyogo, Japan, respectively. X-ray CT analysis of the cathode materials was performed using a transmission X-ray microscope at the BL20XU beamline of the SPring-8 Synchrotron Radiation Facility, Hyogo, Japan. The voxel size of the reconstructed images was 62.4 nm. XAS and CT analyses were performed after the cells were disassembled in a dry Ar-filled glovebox following galvanostatic measurements without exposing the cathode materials to air.

4.2.3   Electrochemistry measurement

The electrochemical performance of the $(100-x)(0.75Li_2S–0.25V_2S_3)–xLiI$ cathode materials was analyzed using a two-electrode cell with a SE. The $(100-x)(0.75Li_2S–0.25V_2S_3)–xLiI$ composites were used as cathode materials without adding conductive materials and SE to them, and the prepared Li_3PS_4 was used as the SE of the cell. The $(100-x)(0.75Li_2S–0.25V_2S_3)–xLiI$ cathode and the SE layer were placed in a polycarbonate tube with a diameter of 10 mm and were pressed together under a pressure of 360 MPa. A Li−In alloy layer[11, 38] was placed on the surface of the SE layer

of the bilayer pellet and served as the anode. Two stainless-steel rods, which were added to the cathode and anode sides by applying a pressure of 120 MPa, were used as current collectors. Cell assembly was performed in a dry Ar-filled glovebox. Electrochemical tests were performed at a current density of 0.13 mA cm^{-2} with discharge and charge cutoff voltages of 0 and 3.0 V, respectively, at 25 °C. To measure the lithium ion diffusion coefficient of the (100-x)(0.75Li$_2$S–0.25V$_2$S$_3$)–xLiI cathode materials, we used a potential step method. A constant potential of 3.0 V was applied to the cells, and the time dependence of the current was monitored using the Solartron Modulab XM ECS. The apparent diffusion coefficients of the composites cathode materials were calculated using the Cottrell equation:

$$i = \frac{nFAD^{1/2}C}{\sqrt{\pi t}},$$

where i is the current, n is the number of electrons, F is the Faraday constant, A is the geometric area, D is the diffusion coefficient, C is the lithium ion concentration, and t is the time. The apparent ionic conductivity of the (100-x)(0.75Li$_2$S–0.25V$_2$S$_3$)–xLiI composites during the potential step was estimated using the Nernst−Einstein equation:

$$\sigma = \frac{CZ^2F^2D}{RT},$$

where σ is the ionic conductivity, Z is the charge valence, R is the gas constant, and T is the absolute temperature.

To measure the electronic and ionic conductivities of the $(100-x)(0.75Li_2S-0.25V_2S_3)-xLiI$ composites, two types of symmetric blocking cells were used, as previously reported.[39] The ion-blocking cell used for electronic conductivity measurements was fabricated by pressing $(100-x)(0.75Li_2S-0.25V_2S_3)-xLiI$ into pellets under a pressure of 360 MPa and setting the pellet between two stainless-steel current collector plates. The electron-blocking cell used for ionic conductivity measurements was fabricated by sandwiching $(100-x)(0.75Li_2S-0.25V_2S_3)-xLiI$ with Li_3PS_4 SE and Li–In alloy (Li–In|SE|$(100-x)(0.75Li_2S-0.25V_2S_3)-xLiI$|SE|Li–In). The alternating current (AC) impedance technique and Solartron Modulab XM ECS were used to measure the electronic and ionic conductivities of the $(100-x)(0.75Li_2S-0.25V_2S_3)-xLiI$ composites. The AC amplitude was 10 mV, and the applied frequency ranged between 1 MHz and 0.1 Hz.

114

4.3 Result and discussion

The crystal structure of the prepared $(100-x)(0.75Li_2S-0.25V_2S_3)-xLiI$ (x = 0, 5, 10, and 20) composites was analyzed using synchrotron X-ray diffraction (XRD), and the results are presented in Figure 4.1a. The peaks in the XRD profiles of the $(100-x)(0.75Li_2S-0.25V_2S_3)-xLiI$ (x = 0, 5, and 10) composites were indexed to Li_2S and V_2S_3 through Le Bail analysis (Fiugre 4.2). A small additional shoulder peak at approximately 10.2°, which was attributed to LiI was observed in the XRD profile of $80(0.75Li_2S-0.25V_2S_3)-20LiI$. The estimated lattice constants of V_2S_3 in the $(100-x)(0.75Li_2S-0.25V_2S_3)-xLiI$ composites remained unchanged with increasing LiI content from x = 0 to 20 (Figure 4.3). Conversely, the estimated lattice constants of Li_2S in the $(100-x)(0.75Li_2S-0.25V_2S_3)-xLiI$ composites increased with increasing LiI content from x = 0 to 10; however, the lattice constants did not further change with increasing LiI content from x = 10 to 20 (Figure 4.1b). The unchanged lattice constant of V_2S_3 with increasing LiI content indicated that I^- ions were not doped into V_2S_3, whereas the increase in lattice constant of Li_2S indicated that I^- ions were doped into Li_2S because the ionic radius of I^- (2.20 Å) was larger than that of S^{2-} (1.84 Å).[40] The unchanged lattice constant of Li_2S with increasing LiI content from x = 10 to x = 20 indicated that the solid solution amount of I^- ions in Li_2S reached the solid solubility limit at x = 10. The SEM images of the composites revealed that the secondary particles

115

of the prepared (100-x)(0.75Li$_2$S–0.25V$_2$S$_3$)–xLiI (x = 0, 5, 10, and 20) composites

were a few micrometers in size (Figure 4.4). The EDX map of the 90(0.75Li$_2$S–

0.25V$_2$S$_3$)–10LiI composite illustrated that sulfur, vanadium, and iodine were

uniformly distributed in the composite (Figure 4.5). The ionic conductivities of the

(100-x)(0.75Li$_2$S–0.25V$_2$S$_3$)–xLiI (x = 0, 5, 10, and 20) composites at 25 °C are

presented in Figures 4.1c and 4.6. The ionic conductivity of the (100-x)(0.75Li$_2$S–

0.25V$_2$S$_3$)–xLiI composites gradually increased from 9.5 × 10^{-5} S cm^{-1} at x = 0 to 8.0 ×

10^{-4} S cm^{-1} at x = 10, and remained unchanged when x was further increased from 10

to 20. The ionic conductivity of the prepared cathode materials was comparable to that

of other SEs, such as Li$_3$PS$_4$.[37, 41] The unchanged ionic conductivity from x = 10 to x =

20 should be attributed to solid solution limit of LiI as shown in Figure 4.1a, b. The

electronic conductivity of the (100-x)(0.75Li$_2$S–0.25V$_2$S$_3$)–xLiI composite at 25 °C

was higher than 0.1 S cm^{-1} (Figures 4.1d and 4.7), which was significantly higher than

the ionic conductivity of the (100-x)(0.75Li$_2$S–0.25V$_2$S$_3$)–xLiI composite.

The electrochemical performance of the prepared (100-x)(0.75Li$_2$S–0.25V$_2$S$_3$)–xLiI

cathodes was measured using galvanostatic charge–discharge measurments(Figures

4.8a and b and S6). The charge–discharge curves of the 100(0.75Li$_2$S–0.25V$_2$S$_3$) and

90(0.75Li$_2$S–0.25V$_2$S$_3$)–10LiI cathodes during the first and second cycles are presented

in Figure 4.8a. The discharge capacities of the (100-x)(0.75Li$_2$S–0.25V$_2$S$_3$)–xLiI (x =

0, 5, 10, and 20) cathodes at different current densities are presented in Figure 4.8b. The charge–discharge curves during the first cycle and the discharge capacity during cycling at different current densities of the (100-x)(0.75Li$_2$S–0.25V$_2$S$_3$)–xLiI (x = 0, 5, 10, and 20) cathodes are illustrated in Figure 4.9. The charge capacity of the 100(0.75Li$_2$S–0.25V$_2$S$_3$) cathode during the first charge process was 135 mAh g^{-1} with a plateau at approximately 1.6 V, and the discharge capacity of the 100(0.75Li$_2$S–0.25V$_2$S$_3$) cathode was 340 mAh g^{-1} with two plateaus at approximately 1.4 and 0.2 V (Figure 4.8a). During the second charge process, the charge capacity of the 100(0.75Li$_2$S–0.25V$_2$S$_3$) cathode was 298 mAh g^{-1} with two plateaus at approximately 0.5 and 1.6 V, which was different from the behavior observed during the first charge. During the second discharge, the charge capacity of the 100(0.75Li$_2$S-0.25V$_2$S$_3$) cathode was 319 mAh g^{-1} with two plateaus at approximately 1.4 and 0.2 V, which was similar to the behavior observed during the first discharge process (Figure 4.8a). Increasing LiI doping from x = 0 to x = 10 improved the electrochemical performance of the (100-x)(0.75Li$_2$S–0.25V$_2$S$_3$)–xLiI cathodes. During the first charge–discharge cycle, the polarization and capacity of the 90(0.75Li$_2$S-0.25V$_2$S$_3$)-10LiI cathode were smaller and larger, respectively, than those of the 100(0.75Li$_2$S-0.25V$_2$S$_3$) cathode (Figure 4.8a). In the second charge process, 90(0.75Li$_2$S-0.25V$_2$S$_3$)-10LiI cathode showed different behavior from first charge process, which is similar to the

100($0.75Li_2S$-$0.25V_2S_3$ cathode, and showed smaller polarization and larger capacity than the 100($0.75Li_2S$-$0.25V_2S_3$) cathode (Figure 4.8a).

The discharge capacity retention of the $(100-x)(0.75Li_2S–0.25V_2S_3)–xLiI$ cathodes at different current densities is illustrated in Figure 4.8b. The discharge capacity of the $(100-x)(0.75Li_2S–0.25V_2S_3)–xLiI$ cathodes increased with increasing LiI content from $x = 0$ to $x = 10$, particularly at higher current densities. Conversely, when the LiI content was further increased from $x = 10$ to $x = 20$, the discharge capacity decreased. This occurred because as the LiI content increased, the contents of Li_2S and V_2S_3 active materials decreased.

The apparent ionic conductivity of the $(100-x)(0.75Li_2S–0.25V_2S_3)–xLiI$ cathodes was measured using a potential step method combined with the Cottrell and Nernst−Einstein equations. The Cottrell plots and apparent ionic conductivities at 25 °C are illustrated in Figures 4.10 and 4.8c, respectively. The apparent ionic conductivity of the $(100-x)(0.75Li_2S–0.25V_2S_3)xLiI$ ($x = 0$, 5, 10, and 20) obtained by potential step was lower than the ionic conductivity of the pristine $(100-x)(0.75Li_2S–0.25V_2S_3)–xLiI$ ($x = 0$, 5, 10, 20) composites. This was attributed to the lithium concentration during the potential step became smaller than that of the pristine state. The apparent ionic conductivity increased with the LiI content, especially increased largely above $x = 10$, which is different tendency from the ionic conductivity at the pristine state. The

118

materials containing LiI exhibits relatively high apparent ionic conductivity even in the charged state with lithium ions extracted, which is the reason why it exhibits high rate-capability even without adding a solid electrolyte in the composite electrode. The question is whether the ion conduction path is formed in the charged state.

Before discussing the ion conduction path, the charge compensation mechanism of this material must be clarified. In this study, we focused on the $90(0.75Li_2S-0.25V_2S_3)-10LiI$ cathode, which presented the highest discharge capacity of all of the $(100-x)(0.75Li_2S-0.25V_2S_3)-xLiI$ ($x = 0$, 5, 10, and 20) cathodes. The electronic structure of the pristine $100(0.75Li_2S-0.25V_2S_3)$ and $90(0.75Li_2S-0.25V_2S_3)-10LiI$ cathodes was examined using XAS of the V L-edge and S K-edge (Figure 4.11). The V L-edge X-ray absorption near edge structure (XANES) spectra of the $90(0.75Li_2S-0.25V_2S_3)-10LiI$ and $100(0.75Li_2S-0.25V_2S_3)$ cathodes were similar, whereas the peak intensity in the S K-edge XANES spectrum of the $90(0.75Li_2S-0.25V_2S_3)-10LiI$ cathode was lower than that of the $100(0.75Li_2S-0.25V_2S_3)$ cathode. These results indicated that electrons were doped into the S 3p orbitals.

Moreover, the changes in the electronic structure of the $100(0.75Li_2S-0.25V_2S_3)$ and $90(0.75Li_2S-0.25V_2S_3)-10LiI$ cathodes during the first charging process were examined using XAS of the V L-edge and S K-edge (Figure 4.12). No peak shifts were observed in the V L-edge XANES spectra of the $100(0.75Li_2S-0.25V_2S_3)$ and

90(0.75Li$_2$S–0.25V$_2$S$_3$)–10LiI cathodes (Figures 4.11a and c, respectively); however, the intensity of the peak at 2470 eV in the S K-edge XANES spectra of the 100(0.75Li$_2$S–0.25V$_2$S$_3$) and 90(0.75Li$_2$S–0.25V$_2$S$_3$)–10LiI cathodes increased during the first charge process (Figures 4.11b and d, respectively). The intensities of the peaks in the S K-edge XANES spectrum of the 90(0.75Li$_2$S-0.25V$_2$S$_3$)-10LiI cathode were higher than those of the 100(0.75Li$_2$S–0.25V$_2$S$_3$) cathode, which was reflected in the charge capacities of these cathodes (Figure 4.8a). These results indicated that charge compensation during the first charge process of the 100(0.75Li$_2$S–0.25V$_2$S$_3$) and 90(0.75Li$_2$S–0.25V$_2$S$_3$)–10LiI cathodes was attributed to sulfur oxidation and not to vanadium oxidation.

X-ray CT was used to clarify the ion conduction path during the first charge of 90(0.75Li$_2$S–0.25V$_2$S$_3$)–10LiI (Figure 4.13). A dark areas of contrast was observed in the 3D and cross-sectional views of the 90(0.75Li$_2$S–0.25V$_2$S$_3$)–10LiI cathode before charging (Figures 4.13a and c, respectively). The dark area was associated with regions of low density and indicated the presence of a void in the 90(0.75Li$_2$S–0.25V$_2$S$_3$)–10LiI cathode. The dark areas of contrast (voids) in the 3D and cross-sectional views of the 90(0.75Li$_2$S–0.25V$_2$S$_3$)–10LiI cathode after charging (Figures 4.13d and f, respectively) were smaller than those observed before charging (Figures 4.13a and c, respectively); moreover some bright particles with high density were observed in the

X-ray CT images of the $90(0.75Li_2S–0.25V_2S_3)–10LiI$ cathode after charging. The decrease in the size of the voids was attributed to the structural change of Li_2S during charging. Figure 4.13b, e present the results of extracting the bright areas of contrast from Figure 4.13a, d and displaying them in three dimensions. A region of high density was not observed in the X-ray CT image of the $90(0.75Li_2S–0.25V_2S_3)–10LiI$ cathode before charging (Figure 4.13b). Conversely, the high density area was uniformly distributed in the X-ray CT image of the $90(0.75Li_2S–0.25V_2S_3)–10LiI$ cathode after charging (Figure 4.13e). Because vanadium, sulfur, and iodine were uniformly dispersed in as-prepared $90(0.75Li_2S–0.25V_2S_3)–10LiI$ (Figure 4.5), and LiI-doped Li_2S underwent a structural change during charging (Figure 4.11d), the region of high density was attributed to the precipitation of LiI rich domain that was dissolved in Li_2S.

To analyze the charge compensation of the $100(0.75Li_2S–0.25V_2S_3)$ and $90(0.75Li_2S–0.25V_2S_3)–10LiI$ cathodes during the second charge process, the changes in electronic structure of these cathodes were examined using XAS of the V L-edge and S K-edge (Figures 4.14 and 4.15). The peak top energy of the V L-edge XAS profile of the $100(0.75Li_2S-0.25V_2S_3)$ cathode shifted toward higher energy when the charge capacity was lower than 100 mAh g^{-1} and remained unchanged in the charge capacity range of 100-200 mAh g^{-1}. These results indicated that vanadium oxidation occurred when the charge capacity during the second charge process was lower than 100 mAh g^{-}

1. The relative peak areas of the S K-edge XAS profile were estimated by integrating the XAS curves in Figures 4.16 and 4.17, and the results are illustrated in Figure 4.14. The relative peak area of the S K-edge XAS profile increased when the charge capacity increased up to 100 mAh g^{-1} and further increased when the charge capacity increased from 100 to 200 mAh g^{-1}. The increase in relative peak area with increasing charge capacity up to 100 mAh g^{-1} was attributed to the increase in hybridization between the S-3p and V-3d orbitals caused by vanadium oxidation,[42] and the increase in peak area with increasing charge capacity from 100 to 200 mAh g^{-1} was ascribed to the formation of holes in the S-3p orbitals.[43] The charge compensation process of the 90(0.75Li$_2$S–0.25V$_2$S$_3$)–10LiI cathode during the second charge process was similar to that of the 100(0.75Li$_2$S–0.25V$_2$S$_3$) cathode. The peak top energy of the V L-edge XAS profiles shifted toward higher energies at charge capacities of up to 200 mAh g^{-1} and remained unchanged in the charge capacity range of 200-450 mAh g^{-1}. These results indicated that during the second charge process, vanadium oxidation occurred at charge capacities of up to 200 mAh g^{-1}. The relative peak areas of the S K-edge XAS profiles increased at charge capacities of up to 200 mAh g^{-1} and further increased in the charge capacity range of 200-450 mAh g^{-1}. The increase in relative peak area with increasing charge capacity up to 200 mAh g^{-1} was attributed to the increasing hybridization between the S-3p and V-3d orbitals caVused by vanadium oxidation,[42] and the increase in the

122

relative peak area with increasing charge capacity from 200 to 450 mAh g^{-1} was ascribed to the formation of holes in the S-3p orbitals.[43] More holes were formed in the $90(0.75Li_2S–0.25V_2S_3)–10LiI$ cathode than in the $100(0.75Li_2S–0.25V_2S_3)$ cathode, and that was reflected in the capacity of the $90(0.75Li_2S–0.25V_2S_3)–10LiI$ cathode being higher than that of the $100(0.75Li_2S–0.25V_2S_3)$ cathode.

The ionic conduction mechanism of the $Li_2S–V_2S_3–LiI$ cathode is illustrated in Figure 4.18. The changes in lithium composition of the $Li_2S–V_2S_3–LiI$ cathode during the first charge process caused the formation of LiI in the cathode matrix. The amount of LiI formed in the cathode was sufficient to provide a lithium ion pathway and contributed to the high ionic conductivity of the cathode during charge and the high rate performance of the cathode. In this study, we demonstrated that the LiI rich domain that self-formed during charging served as an ionic conductive pathway in the cathode. This material design using a self-forming ionic conduction pathway in the composite electrode is a useful strategy for designing high-packing-density electrodes.

In this study, the electrochemical properties of $Li_2S–V_2S_3–LiI$ cathode materials were analyzed, and the reaction mechanism was elucidated using a combination of analytical methods, such as electrochemical measurements, soft XAS of the V *L*-edge and S *K*-edge, and X-ray CT. The optimized $90(0.75Li_2S–0.25V_2S_3)–10LiI$ cathode presented the highest charge and discharge capacities of all analyzed cathodes. Potential step

measurements revealed that when LiI doping exceeded 10 mol% the ionic conductivity of the Li_2S–V_2S_3–LiI cathodes during charging increased significantly. The soft XAS results demonstrated that holes formed in the S-3p orbitals during the entire charge process, whereas holes formed in the V-3d orbitals only in the potential range of 0-1.5 V after the first charge process. X-ray CT images of the Li_2S–V_2S_3–LiI cathodes revealed that LiI rich domain self-formed from the Li_2S–V_2S_3–LiI cathode materials during charging because the lithium composition changed. These results demonstrated that self-forming LiI served as an ionic conduction pathway in the cathode matrix during the first charge process and improved the electrochemical performance of the cathode. We believe that this material design strategy using self-forming ionic conduction pathways in composite electrodes is useful for designing high-packing-density electrodes for all-solid-state batteries.
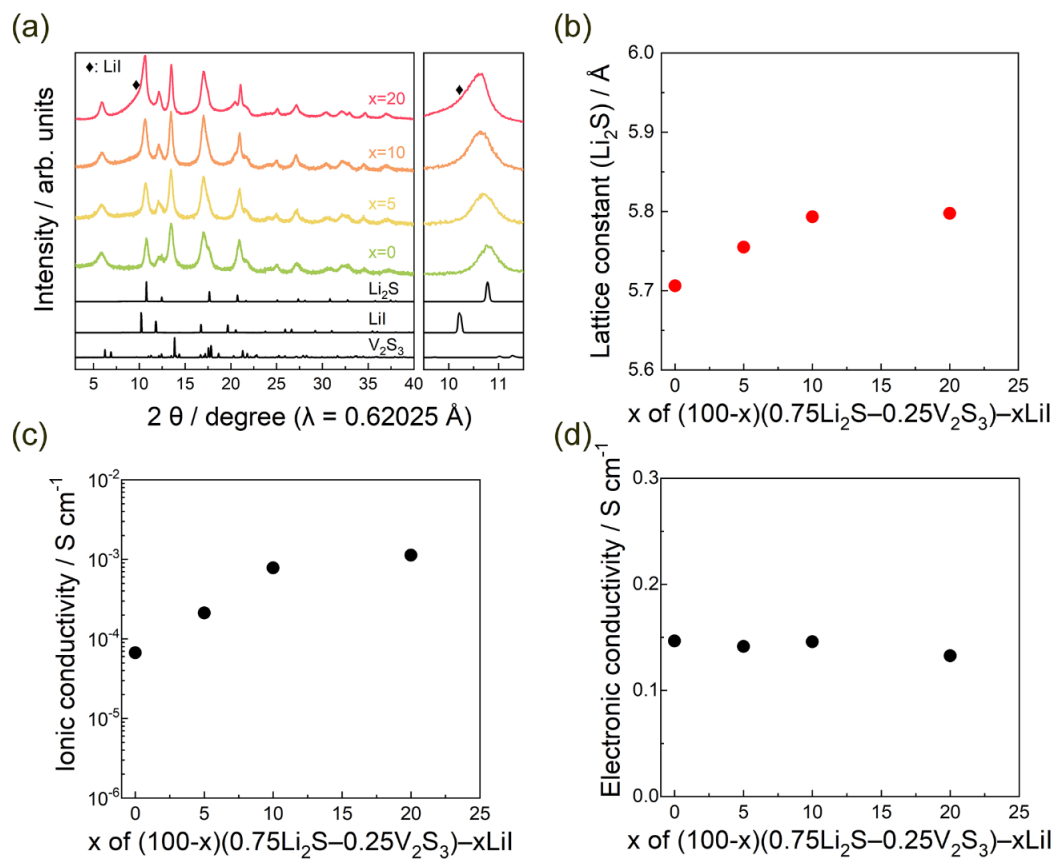
Figure 4.1. (a) X-ray diffraction patterns of (100-x)(0.75Li$_2$S–0.25V$_2$S$_3$)–xLiI (x = 0, 5, 10, and 20) composites, (b) lattice constant of Li$_2$S in (100-x)(0.75Li$_2$S–0.25V$_2$S$_3$)–xLiI (x = 0, 5, 10, and 20) composites, and (c) and (d) ionic and electronic conductivities, respectively, of (100-x)(0.75Li$_2$S–0.25V$_2$S$_3$)–xLiI (x = 0, 5, 10, and 20) composites at 25 °C.
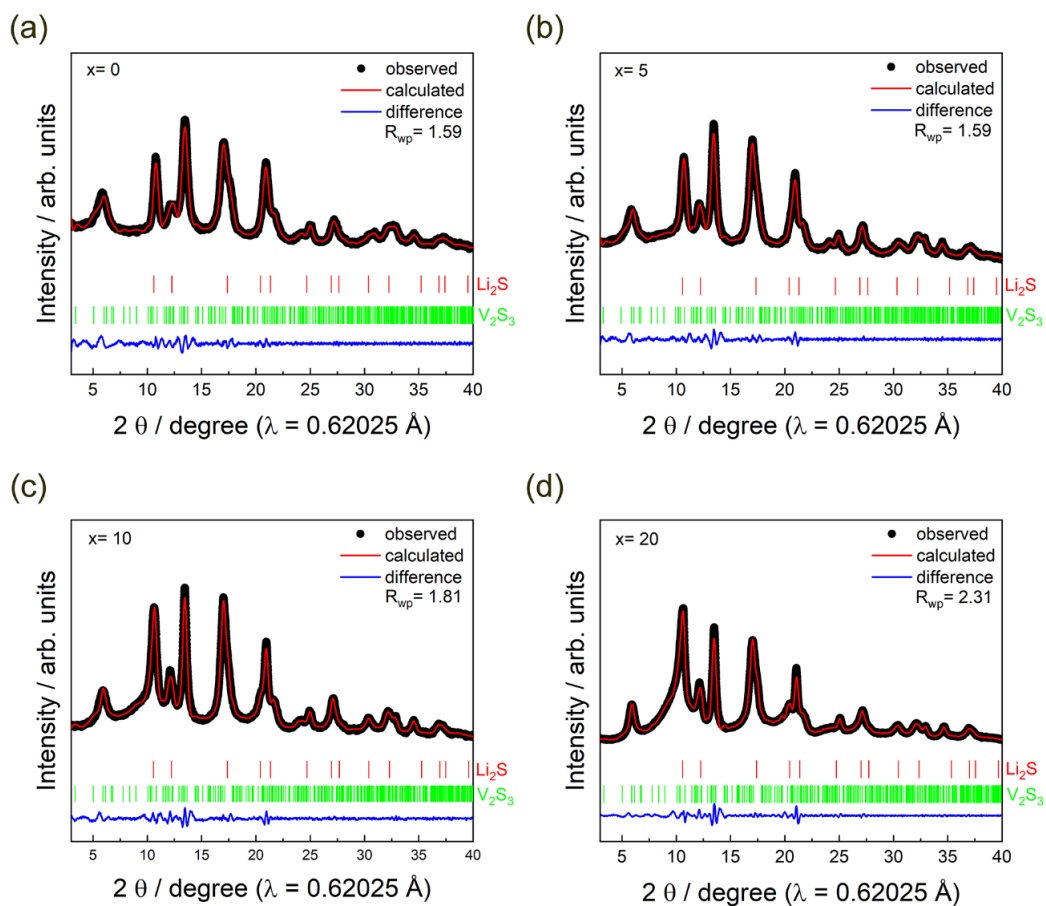
Figure 4.2. XRD pattern and Le Bail analytical fitting profile of (100-x)(0.75Li$_2$S–0.25V$_2$S$_3$)–xLiI (a) x=0, (b) x=5, (c) x=10, and (d) x=20.

(a)   (b)
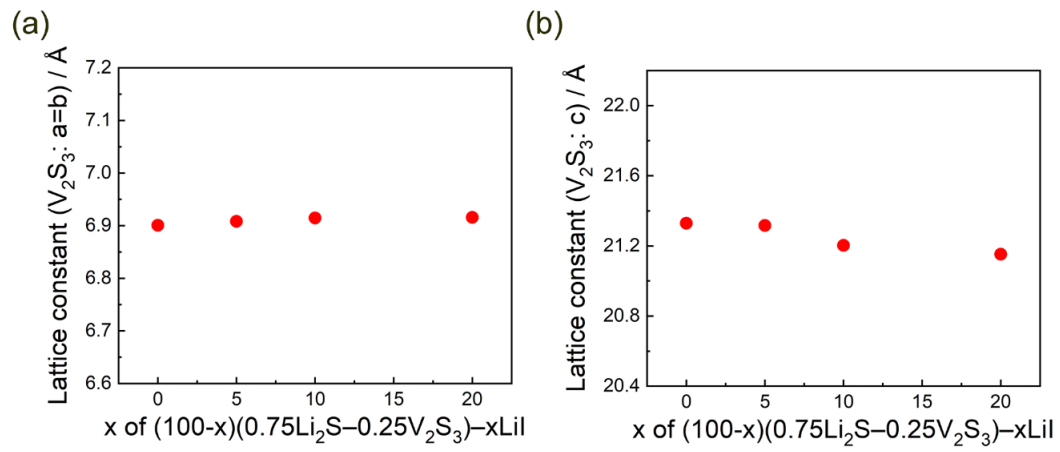
Figure 4.3. lattice constant of V_2S_3 in $(100-x)(0.75Li_2S–0.25V_2S_3)–xLiI$ (x = 0, 5, 10, and 20) composites (a) a and b axis (b) c axis.
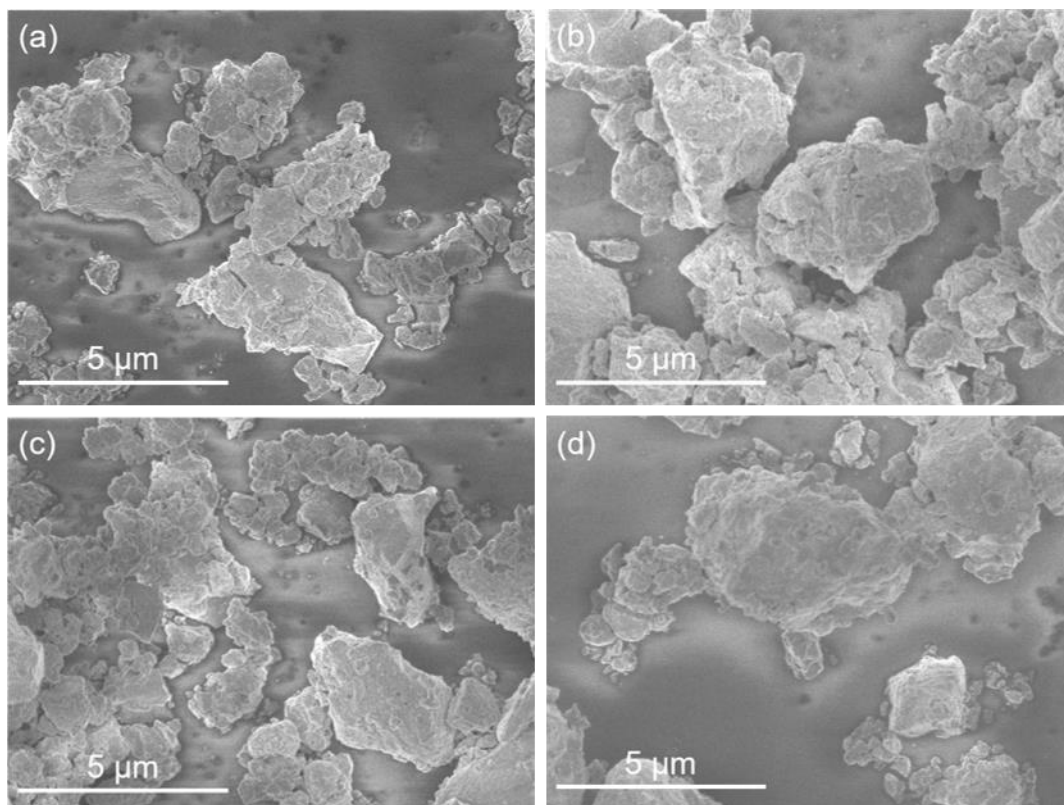
Figure 4.4. SEM images of (a) $100(0.75Li_2S–0.25V_2S_3)$, (b)$95(0.75Li_2S–0.25V_2S_3)$–

$5LiI$, (c) $90(0.75Li_2S–0.25V_2S_3)$–$10LiI$, and (d)$80(0.75Li_2S–0.25V_2S_3)$–$20LiI$ cathodes.
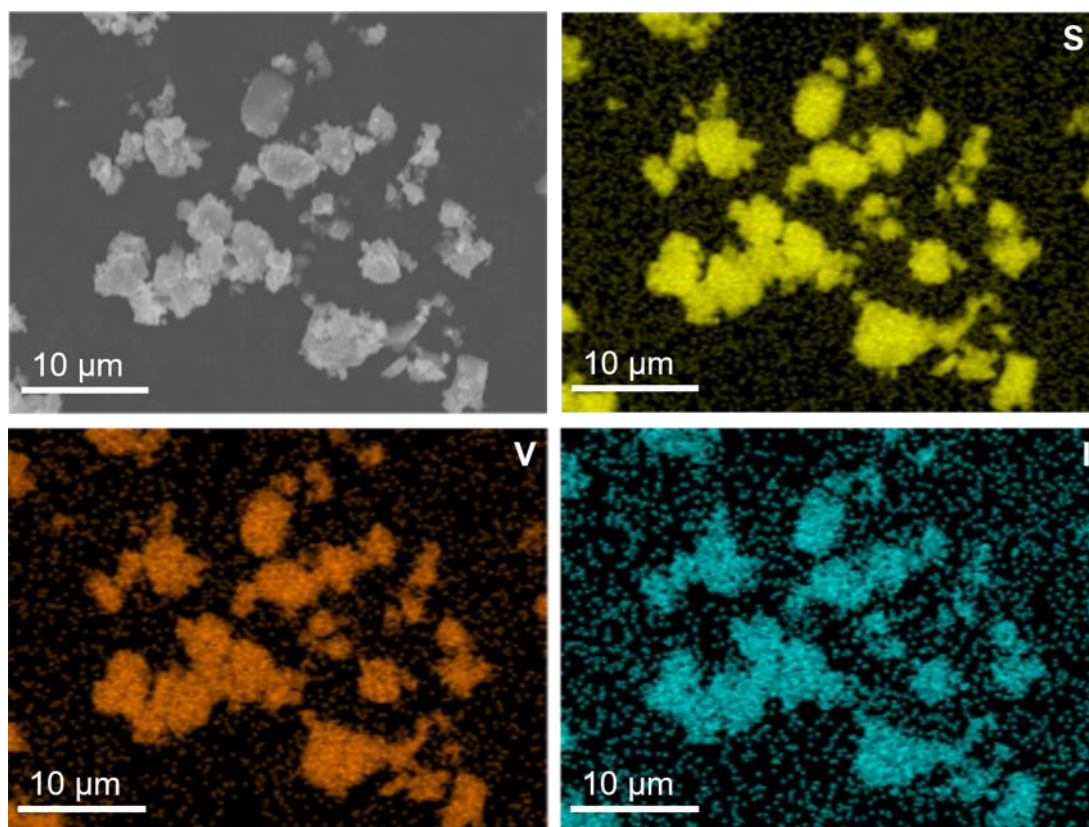
Figure 4.5. SEM-EDX mapping of 90(0.75Li$_2$S–0.25V$_2$S$_3$)–10LiI cathode.
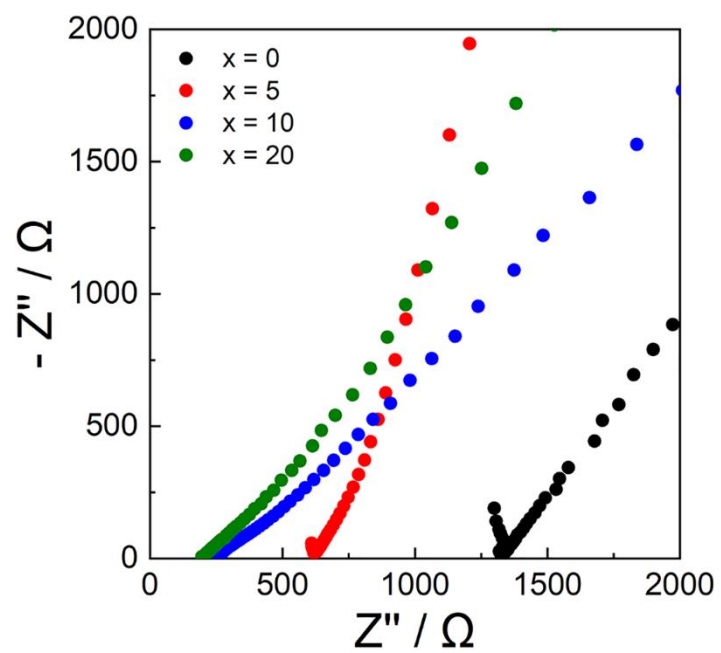
Figure 4.6. Nyquist plots of (100-x)(0.75Li$_2$S–0.25V$_2$S$_3$)–xLiI cathode with x = 0, 5, 10, 20 obtained by using electron-blocking cell at 25°C.
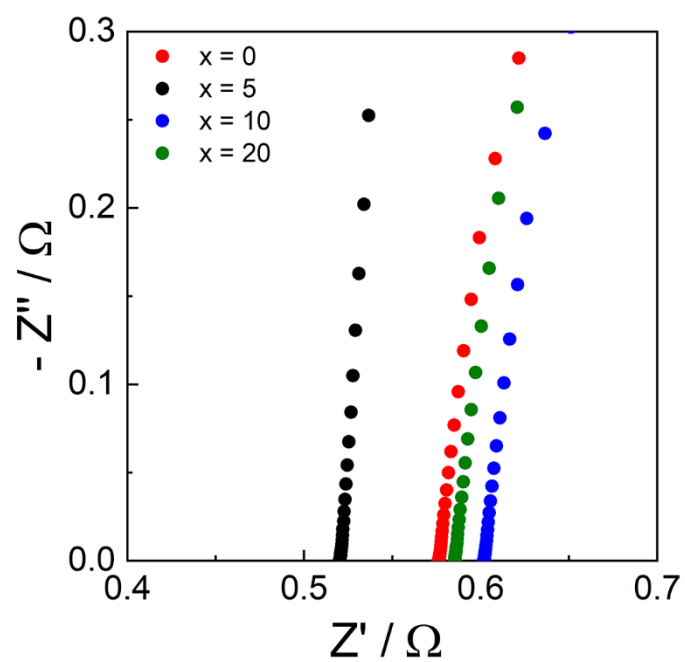
Fugure 4.7. Nyquist plots of (100-x)(0.75Li$_2$S–0.25V$_2$S$_3$)–xLiI cathode with x = 0, 5, 10, 20 obtained by using ion-blocking cell at 25°C.
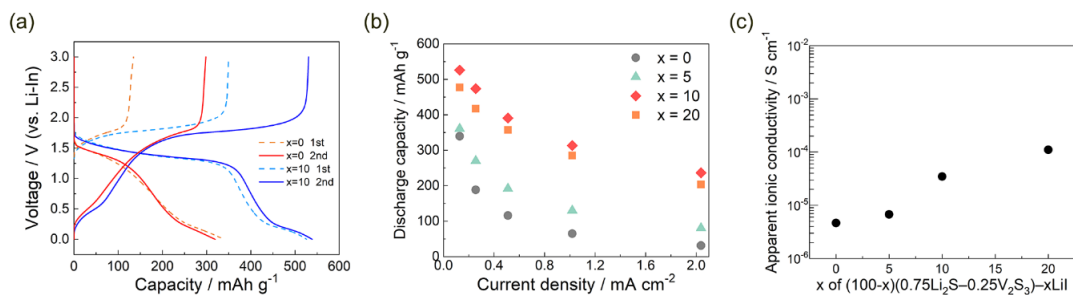
Figure 4.8. (a) Charge–discharge curves of the $100(0.75Li_2S–0.25V_2S_3)$ and $90(0.75Li_2S–0.25V_2S_3)–10LiI$ cathodes during the first and second charge–discharge cycles. (b) Discharge capacity of the $(100-x)(0.75Li_2S–0.25V_2S_3)–xLiI$ cathode at different current densities. (c) Apparent diffusion coefficient of the $(100-x)(0.75Li_2S–0.25V_2S_3)–xLiI$ cathode at 25 °C.
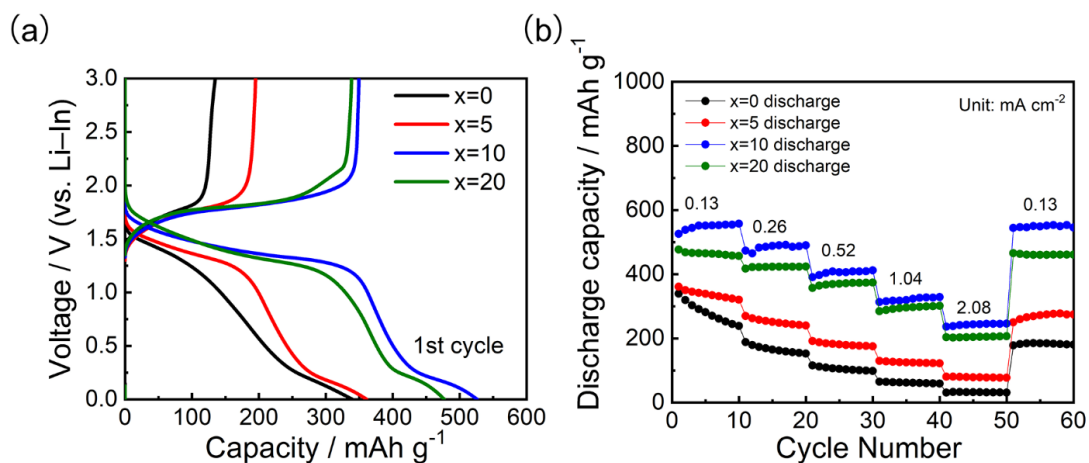
Figure 4.9. (a) the first charge/discharge curves of $(100-x)(0.75Li_2S-0.25V_2S_3)-xLiI$ with $x = 0, 5, 10, 20$, (b) discharge capacity at different current density of $(100-x)(0.75Li_2S-0.25V_2S_3)-xLiI$ with $x = 0, 5, 10, 20$.
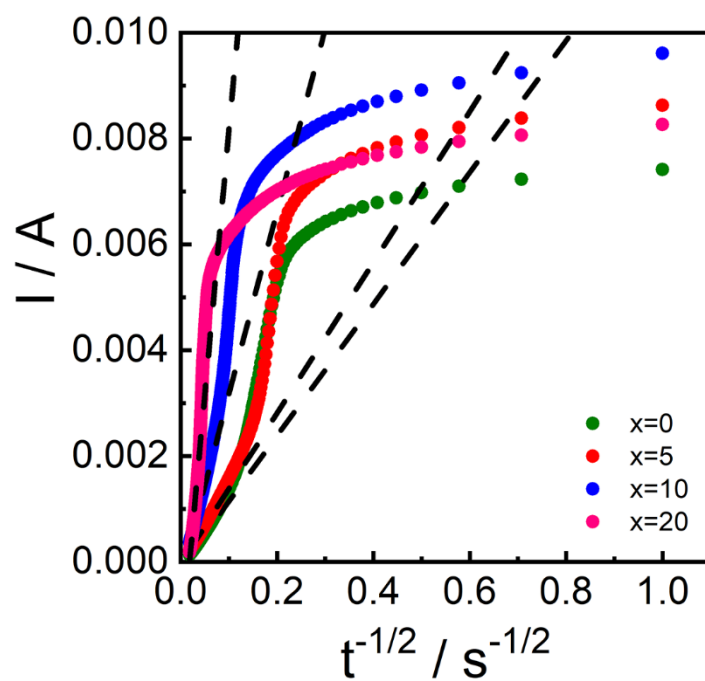
Figure 4.10. Cottrell plots of 100-x(0.75Li$_2$S–0.25V$_2$S$_3$)–xLiI with X=0, 5, 10, 20.
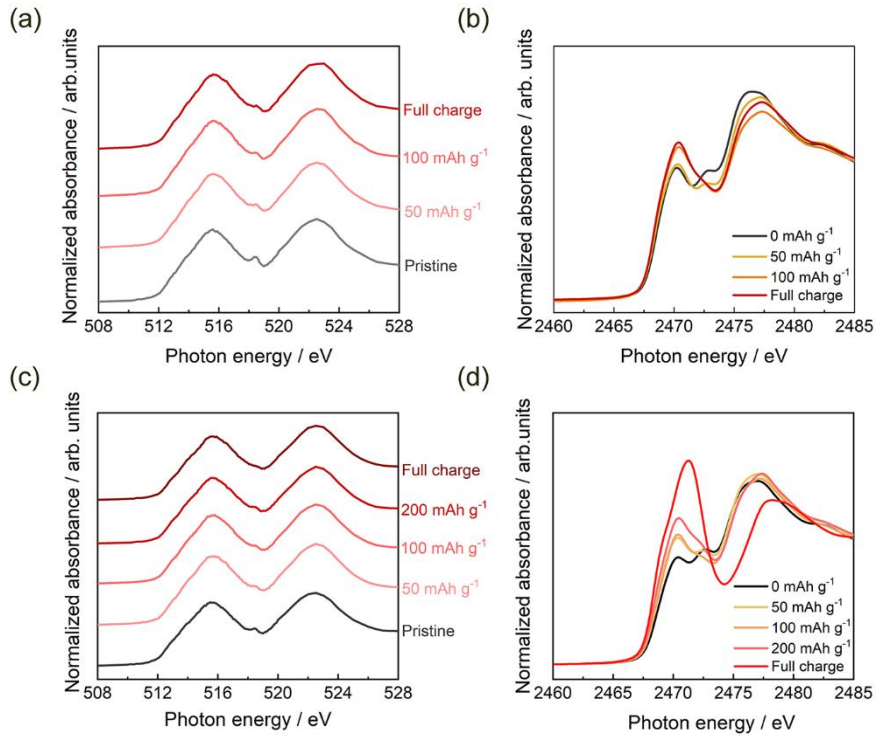
Figure 4.11. (a) V *L*-edge and (b) S *K*-edge X-ray absorption near edge structure spectra of the $100(0.75Li_2S–0.25V_2S_3)$ cathode during the first charge process at different charge states (pristine, 50 mAh g^{-1}, 100 mAh g^{-1}, and full charge), (c) V *L*-edge, and (d) S *K*-edge X-ray absorption near edge structure spectra of the $90(0.75Li_2S–0.25V_2S_3)–10LiI$ cathode during the first charge process at different charge states (pristine, 50 mAh g^{-1}, 100 mAh g^{-1}, 200 mAh g^{-1}, and full charge).
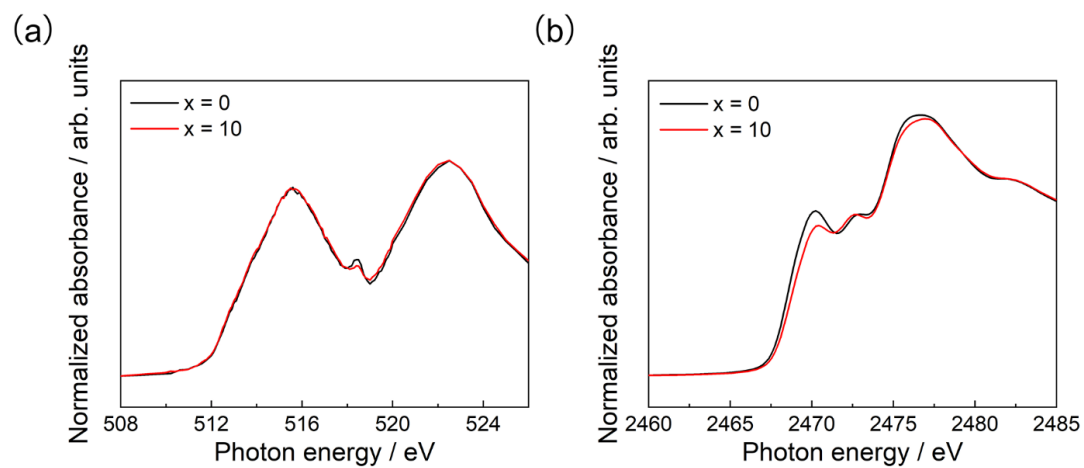
Figure 4.12. XANES of (a) V *L*-edge and (b) S *K*-edge for $0.75Li_2S–0.25V_2S_3$ and $90(0.75Li_2S–0.25V_2S_3)–10LiI$ pristine.
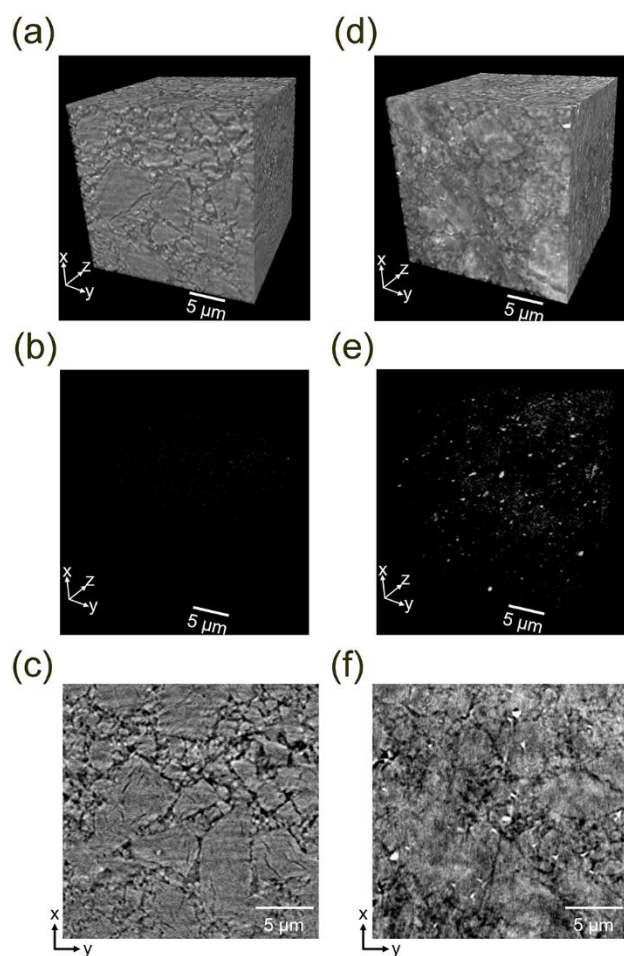
Figure 4.13. Three-dimensional X-ray computerized tomography images of the 90(0.75Li$_2$S–0.25V$_2$S$_5$)–10LiI cathode (a) before and (d) after the first charge process. 3D X-ray computerized tomography images of the high absorption regions of the 90(0.75Li$_2$S–0.25V$_2$S$_5$)–10LiI cathode including LiI and the phase contrast (b) before and (e) after the first charge process. Cross-section images of the interest area in the 3D X-ray computerized tomography images of the 90(0.75Li$_2$S–0.25V$_2$S$_5$)–10LiI cathode (c) before and (f) after the first charge process.
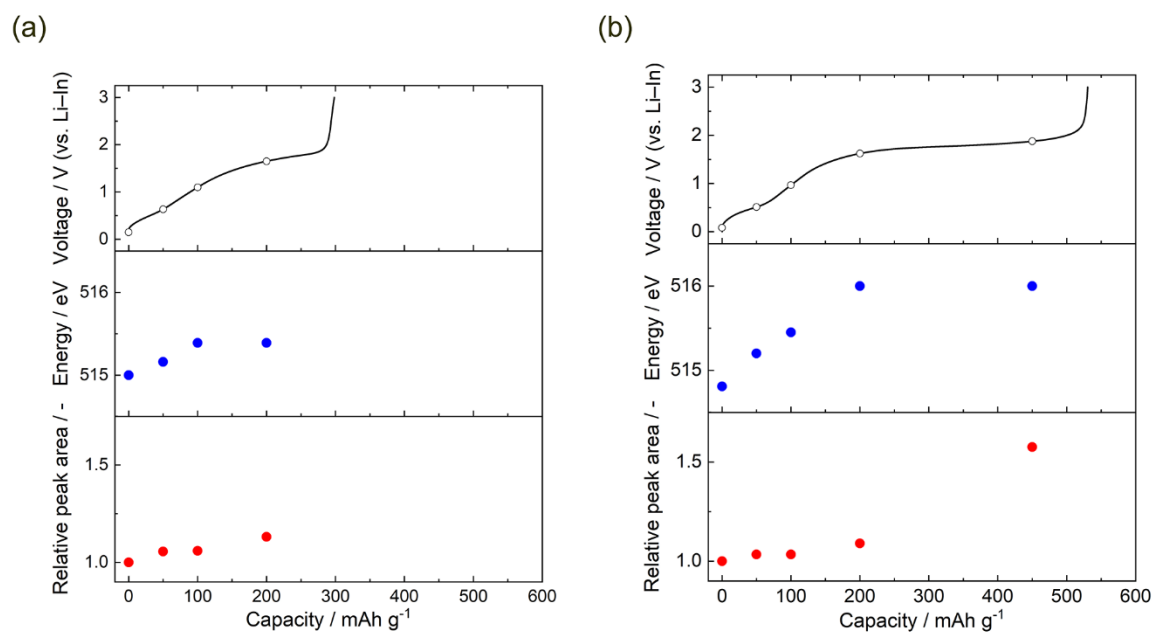
Figure 14. Charge curve (top), peak top energy in the V *L*-edge X-ray absorption near edge structure (XANES) spectra (middle), and relative peak area in the S *K*-edge XANES spectra (bottom) of the (a) $100(0.75Li_2S–0.25V_2S_3)$ and (b) $90(0.75Li_2S–0.25V_2S_3)10LiI$ cathodes during the second charge process.

138
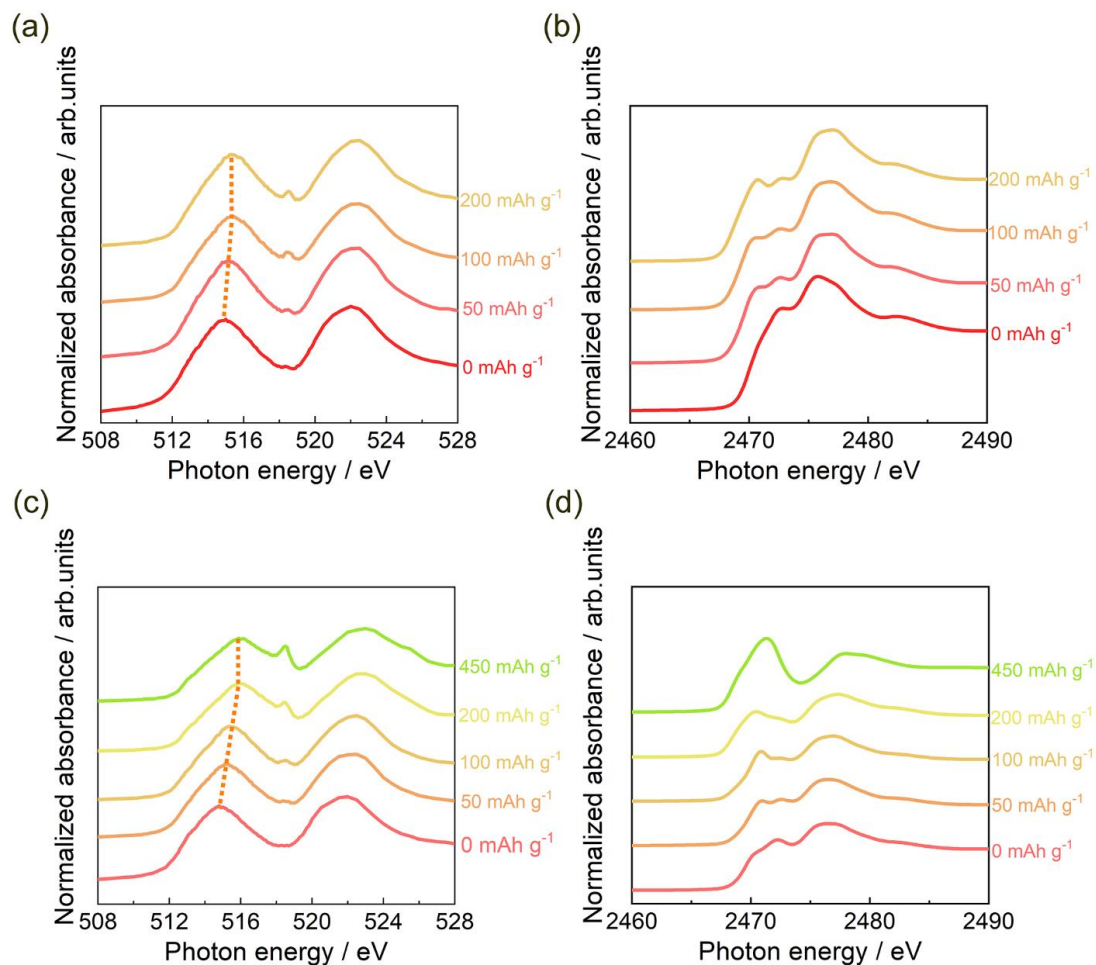
Figure 4.15. XANES for (a) V *L*-edge, (b) S *K*-edge of $100(0.75Li_2S–0.25V_2S_3)$ during the second charge process at different state of charge (0 mAh g^{-1}, 50 mAh g^{-1}, 100 mAh g^{-1} and 200 mAh g^{-1}), (c) V *L*-edge, and (d) S *K*-edge of $90(0.75Li_2S–0.25V_2S_3)–10LiI$ cathode during the second charge at different state of charge (0 mAh g^{-1}, 50 mAh g^{-1}, 100 mAh g^{-1}, 200 mAh g^{-1} and 450 mAh g^{-1}.
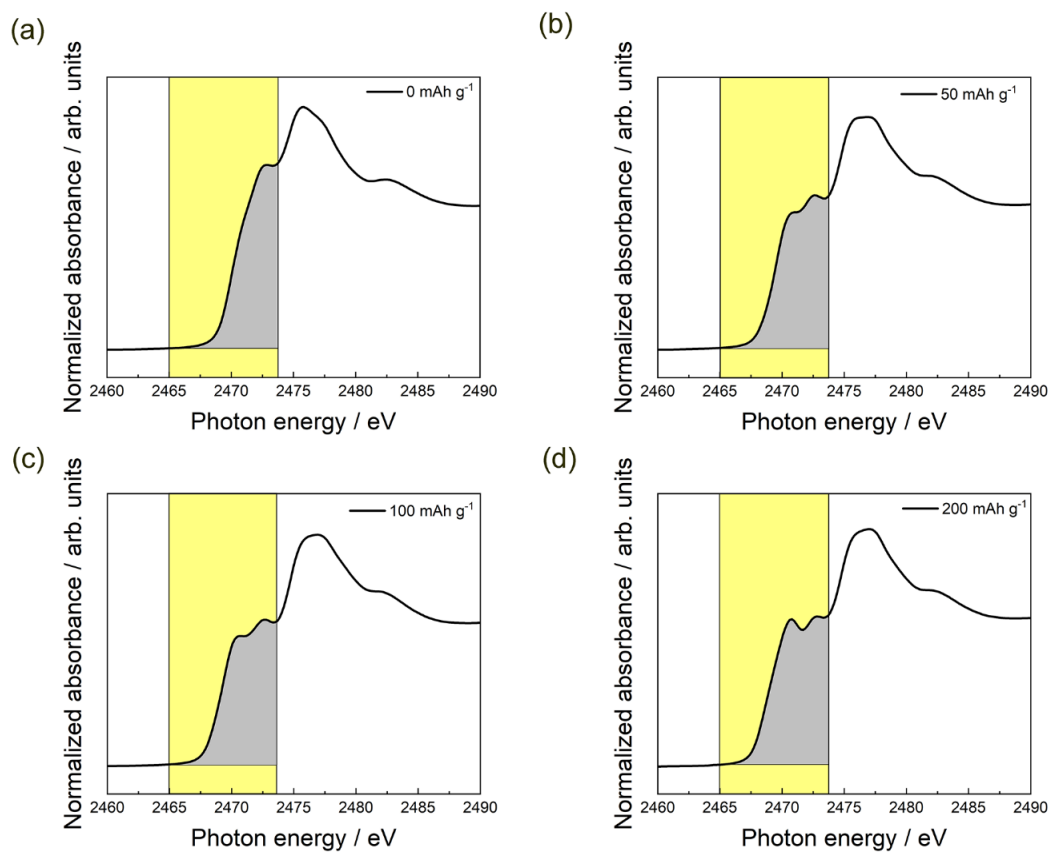
Figure 4.16. S *K*-edge XANES and the integration area for the100(0.75Li$_2$S–0.25V$_2$S$_3$) cathode during the second charge at (a) 0 mAh g^{-1}, (b) 50 mAh g^{-1}, (c) 100 mAh g^{-1} and (d) 200 mAg g^{-1}.
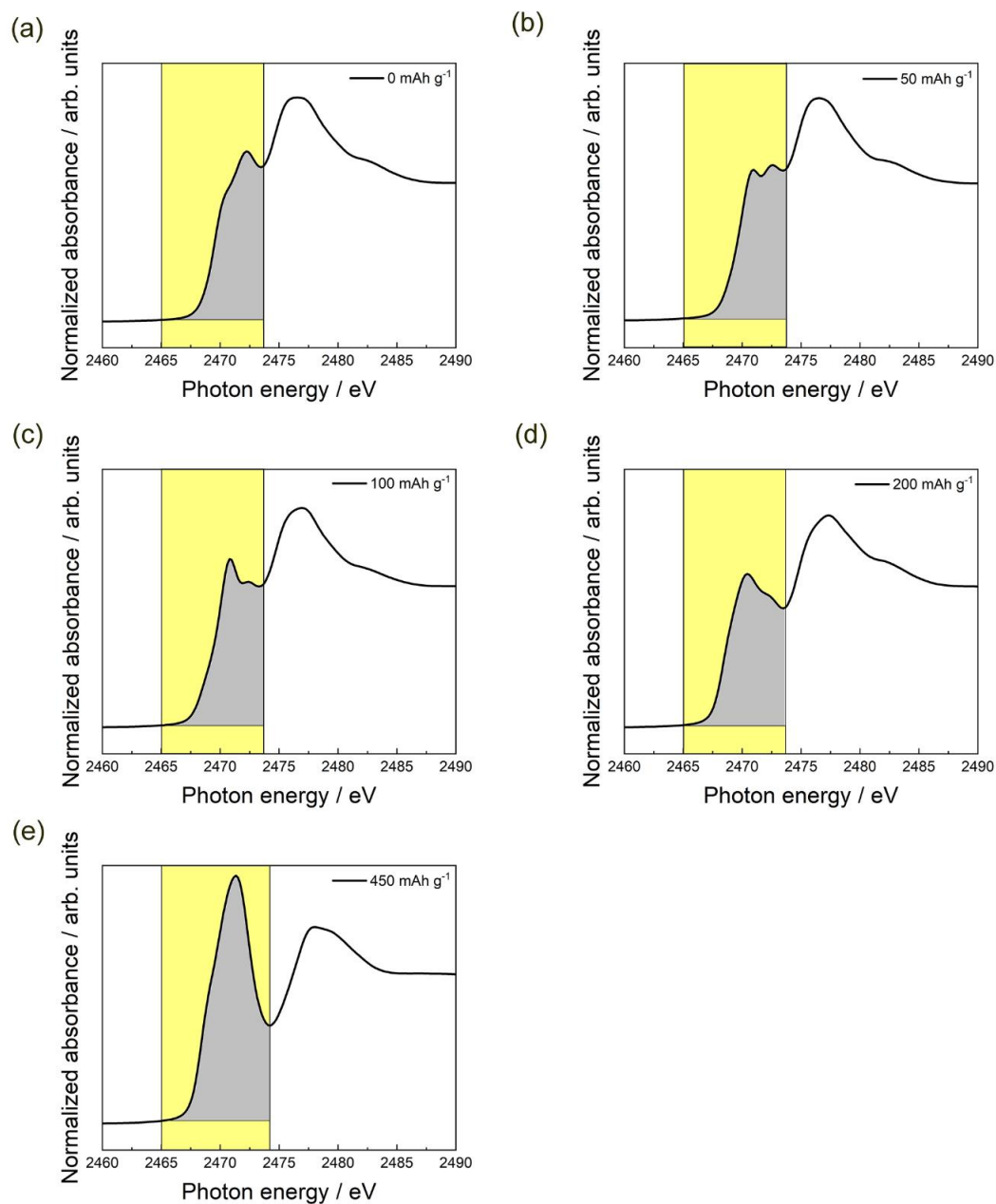
Figure 4.17. S *K*-edge XANES and the integration area for $90(0.75Li_2S–0.25V_2S_3)–$ 10LiI cathode during the second charge at (a) 0 mAh g^{-1}, (b) 50 mAh g^{-1}, (c) 100 mAh g^{-1} (d) 200 mAg g^{-1}and (e) 450 mAg g^{-1}.
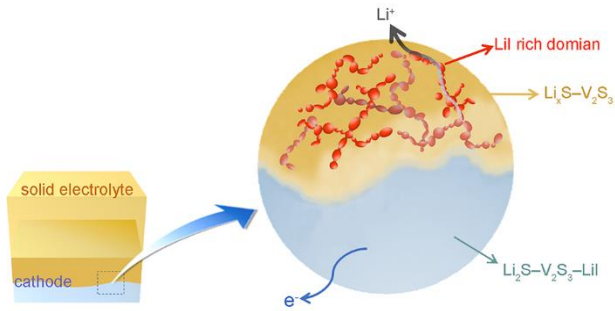
Figure 4.18. Model of self-forming ion conduction pathway in $Li_2S–V_2S_3–LiI$ composites.

Reference

(1)   Oudenhoven, J. F. M.; Baggetto, L.; Notten, P. H. L. All-Solid-State Lithium-Ion Microbatteries: A Review of Various Three-Dimensional Concepts. *Adv. Energy Mater*. **2011**, *1*, 10-33.

(2)   Zhang, Y.; Liu, T.; Zhang, Q.; Zhang, X.; Wang, S.; Wang, X.; Li, L.; Fan, L.-Z.; Nan, C.-W.; Shen, Y. High-performance all-solid-state lithium–sulfur batteries with sulfur/carbon nano-hybrids in a composite cathode. *J. Mater. Chem. A.* **2018**, *6*, 23345-23356.

(3)   Zhou, J.; Ji, H.; Liu, J.; Qian, T.; Yan, C. A new high ionic conductive gel polymer electrolyte enables highly stable quasi-solid-state lithium sulfur battery. *Energy Storage Materials*. **2019**, *22*, 256-264.

(4)   Zhang, Q.; Huang, N.; Huang, Z.; Cai, L.; Wu, J.; Yao, X. CNTs@S composite as cathode for all-solid-state lithium-sulfur batteries with ultralong cycle life. *Journal of Energy Chemistry*. **2020**, *40*, 151-155.

(5)   Kato, Y.; Hori, S.; Saito, T.; Suzuki, K.; Hirayama, M.; Mitsui, A.; Yonemura, M.; Iba, H.; Kanno, R. High-power all-solid-state batteries using sulfide superionic conductors. *Nat. Energy*. **2016**, *1*, 16030.

(6)   Yi, J. G.; Chen, L.; Liu, Y. C.; Geng, H. X.; Fan, L. Z. High Capacity and Superior Cyclic Performances of All-Solid-State Lithium-Sulfur Batteries Enabled by a High-Conductivity $Li_{10}SnP_2S_{12}$ Solid Electrolyte. *ACS Appl. Mater. Interfaces*. **2019**, *11*, 36774-36781.

(7)   Sakuda, A.; Kitaura, H.; Hayashi, A.; Tatsumisago, M.; Hosoda, Y.; Nagakane, T.; Sakamoto, A. All-solid-state Lithium Secondary Batteries Using $Li_2S–P_2S_5$ Solid Electrolytes and $LiFePO_4$ Electrode Particles with Amorphous Surface Layer. *Chem. Lett.* **2012**, *41*, 260-261.

(8)   Machida, N.; Kashiwagi, J.; Naito, M.; Shigematsu, T. Electrochemical properties of all-solid-state batteries with ZrO_2-coated $LiNi_{1/3}Mn_{1/3}Co_{1/3}O_2$ as cathode materials. *Solid State Ionics*. **2012**, *225*, 354-358.

(9)   Oh, G.; Hirayama, M.; Kwon, O.; Suzuki, K.; Kanno, R. Bulk-Type All Solid-State Batteries with 5 V Class $LiNi_{0.5}Mn_{1.5}O_4$ Cathode and $Li_{10}GeP_2S_{12}$ Solid Electrolyte. *Chem. Mater.* **2016**, *28*, 2634-2640.

(10)   Peng, G.; Yao, X.; Wan, H.; Huang, B.; Yin, J.; Ding, F.; Xu, X. Insights on the fundamental lithium storage behavior of all-solid-state lithium batteries containing the $LiNi_{0.8}Co_{0.15}Al_{0.05}O_2$ cathode and sulfide electrolyte. *J. Power Sources*. **2016**, *307*, 724-730.

(11)   Nagao, M.; Hayashi, A.; Tatsumisago, M. Sulfur–carbon composite electrode for all-solid-state Li/S battery with $Li_2S–P_2S_5$ solid electrolyte. *Electrochim.*

Acta. **2011**, *56*, 6055-6059.

(12) Nagao, M.; Hayashi, A.; Tatsumisago, M.; Ichinose, T.; Ozaki, T.; Togawa, Y.; Mori, S. Li$_2$S nanocomposites underlying high-capacity and cycling stability in all-solid-state lithium-sulfur batteries. *J. Power Sources*. **2015**, *274*, 471-476.

(13) Hayashi, A.; Ohtsubo, R.; Ohtomo, T.; Mizuno, F.; Tatsumisago, M. All-solid-state rechargeable lithium batteries with Li$_2$S as a positive electrode material. *J. Power Sources*. **2008**, *183*, 422-426.

(14) Pan, M. Y.; Hakari, T.; Sakuda, A.; Hayashi, A.; Suginaka, Y.; Mori, S.; Tatsumisago, M. Electrochemical Properties of All-solid-state Lithium Batteries with Amorphous FeSx-based Composite Positive Electrodes Prepared via Mechanochemistry. *Electrochemistry*. **2018**, *86*, 175-178.

(15) Li, X. N.; Liang, J. W.; Luo, J.; Wang, C. H.; Li, X.; Sun, Q.; Li, R. Y.; Zhang, L.; Yang, R.; Lu, S. G.; Huang, H.; Sun, X. L. High-Performance Li-SeSx All-Solid-State Lithium Batteries. *Adv. Mater.* **2019**, *31*, 1808100.

(16) Machida, N.; Kobayashi, K.; Nishikawa, Y.; Shigematsu, T. Electrochemical properties of sulfur as cathode materials in a solid-state lithium battery with inorganic solid electrolytes. *Solid State Ionics*. **2004**, *175*, 247-250.

(17) Sakuda, A.; Takeuchi, T.; Okamura, K.; Kobayashi, H.; Sakaebe, H.; Tatsumi, K.; Ogumi, Z. Rock-salt-type lithium metal sulphides as novel positive-electrode materials. *Sci. Rep*. **2014**, *4*, 1-5.

(18) Tatsumisago, M.; Nagao, M.; Hayashi, A. Recent development of sulfide solid electrolytes and interfacial modification for all-solid-state rechargeable lithium batteries. *Journal of Asian Ceramic Societies*. **2013**, *1*, 17-25.

(19) Shin, B. R.; Nam, Y. J.; Kim, J. W.; Lee, Y. G.; Jung, Y. S. Interfacial Architecture for Extra Li$^+$ Storage in All-Solid-State Lithium Batteries. *Sci. Rep*. **2014**, *4*, 5572.

(20) Aso, K.; Sakuda, A.; Hayashi, A.; Tatsumisago, M. All-Solid-State Lithium Secondary Batteries Using NiS-Carbon Fiber Composite Electrodes Coated with Li$_2$S–P$_2$S$_5$ Solid Electrolytes by Pulsed Laser Deposition. *ACS Appl. Mater. Interfaces*. **2013**, *5*, 686-690.

(21) Chen, K.; Shinjo, S.; Sakuda, A.; Yamamoto, K.; Uchiyama, T.; Kuratani, K.; Takeuchi, T.; Orikasa, Y.; Hayashi, A.; Tatsumisago, M.; Kimura, Y.; Nakamura, T.; Amezawa, K.; Uchimoto, Y. Morphological Effect on Reaction Distribution Influenced by Binder Materials in Composite Electrodes for Sheet-type All-Solid-State Lithium-Ion Batteries with the Sulfide-based Solid Electrolyte. *J.Phys.Chem. C.* **2019**, *123*, 3292-3298.

(22) Hu, Y.-S. Batteries: getting solid. *Nat. Energy*. **2016**, *1*, 1-2.

(23) Seino, Y.; Ota, T.; Takada, K.; Hayashi, A.; Tatsumisago, M. A sulphide lithium

super ion conductor is superior to liquid ion conductors for use in rechargeable batteries. *Energy Environ. Sci*. **2014**, *7*, 627-631.

(24) Lau, J.; DeBlock, R. H.; Butts, D. M.; Ashby, D. S.; Choi, C. S.; Dunn, B. S. Sulfide solid electrolytes for lithium battery applications. *Adv. Energy Mater*. **2018**, *8*, 1800933.

(25) Chen, S.; Xie, D.; Liu, G.; Mwizerwa, J. P.; Zhang, Q.; Zhao, Y.; Xu, X.; Yao, X. Sulfide solid electrolytes for all-solid-state lithium batteries: structure, conductivity, stability and application. *Energy Storage Materials*. **2018**, *14*, 58-74.

(26) Lin, Z.; Liu, Z. C.; Dudney, N. J.; Liang, C. D. Lithium Superionic Sulfide Cathode for All-Solid Lithium-Sulfur Batteries. *ACS Nano*. **2013**, *7*, 2829-2833.

(27) Han, F. D.; Yue, J.; Fan, X. L.; Gao, T.; Luo, C.; Ma, Z. H.; Suo, L. M.; Wang, C. S. High-Performance All-Solid-State Lithium-Sulfur Battery Enabled by a Mixed-Conductive Li_2S Nanocomposite. *Nano Lett.* **2016**, *16*, 4521-4527.

(28) Tachez, M.; Malugani, J.-P.; Mercier, R.; Robert, G. Ionic conductivity of and phase transition in lithium thiophosphate Li_3PS_4. *Solid State Ionics*. **1984**, *14*, 181-185.

(29) Kanno, R.; Murayama, M. Lithium Ionic Conductor Thio-LISICON: The Li_2S-GeS_2-P_2S_5 System. *J. Electrochem. Soc.* **2001**, *148*.

(30) Mizuno, F.; Hayashi, A.; Tadanaga, K.; Tatsumisago, M. New, Highly Ion-Conductive Crystals Precipitated from Li_2S–P_2S_5 Glasses. *Adv. Mater.* **2005**, *17*, 918-921.

(31) Kamaya, N.; Homma, K.; Yamakawa, Y.; Hirayama, M.; Kanno, R.; Yonemura, M.; Kamiyama, T.; Kato, Y.; Hama, S.; Kawamoto, K.; Mitsui, A. A lithium superionic conductor. *Nat. Mater.* **2011**, *10*, 682-686.

(32) Teragawa, S.; Aso, K.; Tadanaga, K.; Hayashi, A.; Tatsumisago, M. Liquid-phase synthesis of a Li_3PS_4 solid electrolyte using N-methylformamide for all-solid-state lithium batteries. *J. Mater. Chem. A.* **2014**, *2*, 5095-5099.

(33) Yubuchi, S.; Teragawa, S.; Aso, K.; Tadanaga, K.; Hayashi, A.; Tatsumisago, M. Preparation of high lithium-ion conducting Li_6PS_5Cl solid electrolyte from ethanol solution for all-solid-state lithium batteries. *J. Power Sources*. **2015**, *293*, 941-945.

(34) Phuc, N. H. H.; Morikawa, K.; Mitsuhiro, T.; Muto, H.; Matsuda, A. Synthesis of plate-like Li_3PS_4 solid electrolyte via liquid-phase shaking for all-solid-state lithium batteries. *Ionics*. **2017**, *23*, 2061-2067.

(35) Rosero-Navarro, N. C.; Kinoshita, T.; Miura, A.; Higuchi, M.; Tadanaga, K. Effect of the binder content on the electrochemical performance of composite cathode using Li_6PS_5Cl precursor solution in an all-solid-state lithium battery.

Ionics. **2017**, *23*, 1619-1624.

(36)   Rosero-Navarro, N. C.; Miura, A.; Tadanaga, K. Composite cathode prepared by argyrodite precursor solution assisted by dispersant agents for bulk-type all-solid-state batteries. *J. Power Sources*. **2018**, *396*, 33-40.

(37)   Hayashi, A.; Hama, S.; Morimoto, H.; Tatsumisago, M.; Minami, T. Preparation of Li_2S-P_2S_5 amorphous solid electrolytes by mechanical milling. *J. Am. Ceram. Soc.* **2001**, *84*, 477-479.

(38)   Santhosha, A. L.; Medenbach, L.; Buchheim, J. R.; Adelhelm, P. The Indium-Lithium Electrode in Solid-State Lithium-Ion Batteries: Phase Formation, Redox Potentials, and Interface Stability. *Batteries & Supercaps*. **2019**, *2*, 524-529.

(39)   Asano, T.; Yubuchi, S.; Sakuda, A.; Hayashi, A.; Tatsumisago, M. Electronic and Ionic Conductivities of $LiNi_{1/3}Mn_{1/3}Co_{1/3}O_2$-$Li_3PS_4$ Positive Composite Electrodes for All-Solid-State Lithium Batteries. *J. Electrochem. Soc.* **2017**, *164*, A3960-A3963.

(40)   Shannon, R. D. Revised effective ionic radii and systematic studies of interatomic distances in halides and chalcogenides. *Acta Crystallographica Section A*. **1976**, *32*, 751-767.

(41)   Liu, Z.; Fu, W.; Payzant, E. A.; Yu, X.; Wu, Z.; Dudney, N. J.; Kiggans, J.; Hong, K.; Rondinone, A. J.; Liang, C. Anomalous High Ionic Conductivity of Nanoporous β-Li_3PS_4. *J. Am. Chem. Soc.* **2013**, *135*, 975-978.

(42)   Cai, L.; Zhang, Q.; Mwizerwa, J. P.; Wan, H.; Yang, X.; Xu, X.; Yao, X. Highly Crystalline Layered VS_2 Nanosheets for All-Solid-State Lithium Batteries with Enhanced Electrochemical Performances. *ACS Appl. Mater. Interfaces*. **2018**, *10*, 10053-10063.

(43)   Takeuchi, T.; Kageyama, H.; Nakanishi, K.; Tabuchi, M.; Sakaebe, H.; Ohta, T.; Senoh, H.; Sakai, T.; Tatsumi, K. All-Solid-State Lithium Secondary Battery with Li_2S–C Composite Positive Electrode Prepared by Spark-Plasma-Sintering Process. *J. Electrochem. Soc.* **2010**, *157*, A1196.

Chapter 5 Electrochemical properties of all-solid-state lithium batteries with Li₃CuS₂ as composite cathode materials

For solid-state lithium sulfur battery, the sufficient electronic and ionic conductivity is necessary for cathode electrode. Metal sulfides have shown to improve the performance for all-solid-state lithium sulfur battery, owing to the high electronic conductivity. In this study, we developed Li_3CuS_2 as active materials with high electronic conductivity. Li_3CuS_2 was mix with Li_3PS_4 as composite cathode for all-solid-state lithium sulfur battery. The 1st charge and discharge capacity of Li_3CuS_2-Li_3PS_4 composite cathode is about 346.86 mAh/g and 347.82 mAh/g. And the reaction mechanism of cathode composites was clarified by soft X-ray absorption spectroscopy (XAS) of S K-edge, Cu K-edge and L-edge at the different state of charge process. The oxidation of S and Cu ion can be found and gradually increase of Cu-S bond was also proved by extended X-ray absorption fine structure (EXAFS).

5.1 Introduction

Lithium–sulfur batteries are a new generation of lithium secondary batteries. Unlike the traditional transition metal oxide lithium-ion batteries, lithium–sulfur batteries consist of sulfur / lithium sulfide, lithium metal, and conventional organic ethers as the cathode, anode, and electrolyte, respectively. During charge and discharge process,

sulfur / lithium sulfide can contribute two electrons S + 2 e$^-$ $\leftrightarrow$ S^{2-}. Therefore, the specific capacity of sulfur and Lithium sulfide cathodes can reach extremely high values (1675 mAh/g and 1168 mAh/g, respectively), which exceed those of the current lithium-ion battery cathodes.[1-5] And sulfur is abundant, inexpensive compared with metallic minerals, low-toxic, environmentally friendly, and degradable, it presents great potential for large-scale practical applications.[6-12] However, when sulfur or lithium sulfide are used as the cathode materials in liquid lithium-sulfur battery, the polysulfides will be formed during cycling and react with the electrolyte. This causes a shuttle effect and leads to the consumption of the active substances, which results in poor cycling performance.[13-17]

Replacing liquid electrolytes with solid electrolytes can completely prevent polysulfides dissolution in electrolytes.[18, 19] However, the ionic and electronic insulating properties of sulfur and lithium sulfide are major drawbacks for the development of sulfur-based cathodes. The electronic and ionic conductivity of sulfur and lithium sulfide can be improved by homogeneously mixing electronic and ionic conductor additives with sulfur.[20] Han et al.[21] used a bottom-up method to prepare a battery featuring Li$_2$S, Li$_6$PS$_5$Cl, and polyvinylpyrrolidone as the active material, electrolyte, and carbon precursor of the cathode material. Nagao et al[22] studied the effect of Li$_2$S particle size on the electrochemical performance of all-solid-state batteries and determined that decreasing cathode particle size can effectively improve the reversible and rate performances of batteries.

Recently, metal sulfides have received increasing attention owing to their high electrochemical activity, excellent electronic conductivity, and remarkable theoretical capacity. The interface between the sulfide cathode and the sulfide solid electrolyte is stable and presents low resistance and excellent electrochemical properties.[23]

In this research, Li_3CuS_2 active materials were developed as novel materials with high electronic by mechanical milling of the mixture of copper, sulfur and lithium sulfide powders. The crystal and morphology of Li_3CuS_2 were investigated, All-solid-state lithium sulfur battery using Li_3CuS_2-Li_3PS_4 as composite electrode layers were fabricated and characterized in order to demonstrate their advantage as cathode materials in all solid-state lithium sulfur battery.

5.2 Experimental Section
5.2.1 Preparation of samples

The Li_3CuS_2 samples in this study were prepared using ball milling. Stoichiometric amounts of Li_2S (99% purity, Mitsuwa), Cu (99% purity, FujiFilm), and S (99% purity, Aldrich) were hand-mixed in a mortar for 30 min, followed by mechanical mixing with ZrO_2 balls at 390 rpm for 90 h. The Li_3PS_4 glass powder used to fabricate the SE was prepared via ball milling using a previously reported procedure, as follows. Li_2S (99% purity, Aldrich) and P_2S_5 (99% purity, Aldrich) powders with a 3:1 molar ratio were mechanically mixed using ZrO_2 balls at 370 rpm for 30 h. The Li_3CuS_2-Li_3PS_4 samples were weighted to weight ratio at 70:30 (wt %), then the mixture were mixed with ZrO_2 balls at 160 rpm for 1 h. All these procedures were carried out under a dry Ar atmosphere glove box.

5.2.2   Characterization

XRD for the as-prepared Li_3CuS_2 samples was performed by RINT-Ultima III (Rigaku) with CuKα radiation. Soft X-ray absorption spectroscopy measurements for S K-edge and Cu L-edge were performed at BL27SU at SPring-8, Japan. Hard X-ray absorption spectroscopy measurements for Cu K-edge were performed at BL14B2 at SPring-8. The particle morphology of the samples was observed by scanning electron microscopy ((FE-SEM, JEOL, JSM-6610A).

5.2.3 Electrochemistry measurement

All the solid-state batteries are prepared inside an Ar-filled glove box and tested by all solid-state cell. First, the 80 mg Li_3PS_4 were placed in a polycarbonate tube (diameter of 10 mm) and pressed to form the SE (solid electrolyte) layer, and then 4mg cathode powder Li_3CuS_2 or Li_3CuS_2-Li_3PS_4 mixture were dispersed on one side of the SE layer and pressed at 360 Mpa. Finally, A Li–In alloy was placed on the another of the SE layer of the bilayer pellet to function as an anode. The Li_3CuS_2 cathodes were conducted with cut-off voltages of 0.0 V-3.0 V (0.62 V-3.62 V vs. Li) for charge and discharge. And the Li_3CuS_2-Li_3PS_4 composite cathode were conducted with cut-off voltage of 1.0 V- 1.9 V (1.62 V-2.52 V vs. Li) for charge and discharge.

To measure the electronic conductivity and ionic conductivity for Li_3CuS_2 composite two kinds of symmetric cell was used as previous report.[24] The ion blocking cell was used for measurement of the electronic conductivity. The cell was fabricated by pressing the composite sample into pellet under 360 MPa at room temperature. The pellet was set between two stainless-steel (SS) plates as current collectors. The electron-blocking cell was used for the measurement of the ionic conductivities. The cell consists of five layers pellet (Li-In/SE/sample/SE/Li-In). The SE layers (Li_3PS_4) were used as electron blocking layers. The AC impedance technique was used to measure the electronic conductivity and ionic conductivity by Solartron Modulab ECS. The AC amplitude was 10 mV, with the applied frequency ranging from 1 MHz to 10 Hz.

For galvanostatic intermittent titration technique (GITT), after each galvanostatic step for 30 min at 0.13 mA cm^{-2}, the cell was relaxed at open circuit voltage (OCV) for 4 h to approach the quasi-equilibrium state.

The Li$^+$ diffusion coefficients of Li$_3$CuS$_2$ were calculated by potentiostatic intermittent titration technique (PITT) measurement. The chronoamperometries was tested repeatedly with a potential step of 0.01 V from 1.6 V to 1.9 V by HZ-7000 (Hokuto Denko).

5.3 Result and discussion

Li_3CuS_2 was prepared form Li_2S, Cu and sulfur by ball milling method. From the XRD pattern (Figure 5.1a), the composite showed the single anti-fluorite structure with the space group is Fm-3m (as shown in Figure 5.1b). Sulfur atom occupied the 4a site, Li atom and copper atom occupied the 8c site, meanwhile the occupation of Li atom and copper atom is 0.75 and 0.25 respectively. And SEM images of Li_3CuS_2 was shown in Figure 5.1c, the particle size of samples were about 2 um to 10 um. Typically, the EDX mapping of Li_3CuS_2 were also shown in Figure 1c, sulfur and copper spread uniform in cathode composite.

To study the electronic and ionic conductivity of the Li_3CuS_2 composites, the ion-blocking and electron-blocking cells as previous report[24] were used to separate the electronic conductivity and ionic conductivity. Figure 5.2 and 5.3 show the electronic conductivity and ionic conductivity of Li_3CuS_2 composite. At 25 ^oC, the electronic conductivity and ionic conductivity of Li_3CuS_2 are 0.14 S cm^{-1} and 7.96 x 10^{-5} S cm^{-1}.

As the Li_3CuS_2 can show the high electronic conductivity, the pure Li_3CuS_2 was used as the cathode electrode without additive of any electronic and ionic conductor. The electrochemical performance of the prepared Li_3CuS_2 cathode materials were measured by galvanostatic charge and discharge measurements at 0.13 mA/cm^2 and the results were shown in Figure 5.4. The 1st charge and discharge capacity of Li_3CuS_2 is about

153

45.14 mAh/g and 41.89 mAh/g. And cycle ability of Li_3CuS_2 was also shown in Figure5.4b, the coulombic efficiency for 1st cycling is about 92.78% and after 1st cycle the coulombic efficiency is around 100%. Li_3CuS_2 can show limited charge capacity without additive of other electronic and ionic conductor, however the charge capacity is much lower than the theoretical charge capacity (542 mAh/g) of Li_3CuS_2 when 3 Li^+ can deinserted from Li_3CuS_2. The reason for poor charge capacity may owning to the lower ionic conductivity than electronic conductivity of Li_3CuS_2, only parts of the Li_3CuS_2 which are in touch with the solid electrolyte can inserted or deinserted the Li^+, and leading the poor electrochemical performance of Li_3CuS_2. At this point, the ionic conductivity of Li_3CuS_2 is needed to be improved.

In order to improve the ionic conductivity of Li_3CuS_2, Li_3PS_4 was mix with Li_3CuS_2 as cathode composite, the weight ratio of Li_3CuS_2 and Li_3PS_4 is 70:30%. The electrochemical performance of Li_3CuS_2-Li_3PS_4 composite were measured by galvanostatic charge and discharge measurements and the result were shown in Figure 5.5. The 1st charge and discharge capacity of Li_3CuS_2-Li_3PS_4 composite cathode at 0.13 mA/cm^2 is about 346.86 mAh/g and 347.82 mAh/g. Rate performances of Li_3CuS_2-Li_3PS_4 at different current density were also shown in Figure 3b. After mixed with Li_3PS_4 the capacity of Li_3CuS_2 was obviously improved, owing to the construction of fine Li^+ path between Li_3CuS_2 and solid electrolyte.

Galvanostatic intermittent titration technique (GITT) was used to further understand the electrochemical process, as displayed in Figure 5.6. The cell was relaxed at open circuit voltage (OCV) for 3 h to approach the quasi-equilibrium state, after each galvanostatic charging/discharging stage for 0.5 h at 0.13 mA cm^{-2}. The overpotential upon charging and discharge process is small and the OCV values of every galvanostatic stages were stabilized as presented in Figure 5.6b, the are no too much differences of OCV between the charging and discharging states. The only one charge and discharge plateau and low polarization of OCV may suggested two phase transformation between charge and discharge process.

The Li^{+} diffusion coefficients of Li$_3$CuS$_2$ were also calculated by potentiostatic intermittent titration technique (PITT) measurement. The chronoamperometries was tested repeatedly with a potential step of 0.01 V. The Li^{+} diffusion coefficients were calculated by PITT results based on the following equation.

$$D_{Li^+} = -\frac{d \ln I(t)}{dt} \frac{4L^2}{\pi^2} \tag{1}$$

Where D is the diffusion coefficient, L (cm) is the diffusion length (thickness of cathode), and $I(t)$ (A) is the recorded transient current as a function of time (t), respectively.

The Li^{+} diffusion coefficient at different potential was shown in figure 5.7a, and it was around ~10^{-11} to ~10^{-12} cm^2 s^{-1} during the charge process. As the Li+ diffusion coefficient is constant, that can explain the steady OCV (figure 5.6) during the charge process. And such high diffusion coefficient is comparable with that of typical LiFePO$_4$ and LiCoO$_2$, indicating a smooth ion diffusion in Li$_3$CuS$_2$.

The rate-determining step was also discussed by Kolmogorov-Johnson-Mehl-Avrami (KJMA) theory. According to KJMA model, the volumetric fraction (V) of product in phase-transition mechanism is subjected to the following correlation,

$$V = 1 - \exp\left(-kt^n\right) \tag{2}$$

where k, t and n are rate constant, time and Avrami exponent, respectively. The equation (2) can be rearranged as:

$$\ln \ln[1/(1 - V)] = n \ln t + \ln k \tag{3}$$

Therefore, the Avrami exponent n can be obtained by plotting and linear-fitting $\ln \ln [1/(1-V)]$ vs. $\ln t$. The Avrami exponent n is further explained as:

$$n = a + bc \tag{4}$$

The value of a represents the nucleation rate as a function of time, where $a = 0$, $0 < a < 1$, $a = 1$ and $a > 1$ refer to zero, decreasing, constant and increasing nucleation rate, respectively. The values of b and c describe the phase-growth dimension ($b = 1, 2, 3$ for 1D, 2D, 3D growth, respectively) and rate-determining step ($c = 1$ for phase-boundary-movement controlled and $c = 0.5$ for diffusion controlled). The crystalline fraction V are evaluated by SOC, which was acquired by integrating the current densities upon chronoamperometric process as a function of time.

The transient current of potential step from 1.71 to 1.72 V (figure 5.7b) exhibited a typical nucleation and growth in a two-phase electrochemical reaction. The current increasing from point (I) to (II) represents nucleation process that produce a large number of new phase boundaries and reach maximum at point (II), and the following current decreasing from point (II) to (III) represents the nuclei growth which lead to the merges of phase boundaries.

156

The fitting results of avrami exponent n was 1.028. The $n = 1.028$ can be explained as $a = 0.028$, $b = 1$ and $c = 1$. which could be interpreted as being due to a phase-boundary-controlled 1D phase transition with decreasing nucleation rate (a = 0.028, b = 1, and c = 1).

Sulfur K-edge XAS of Li_3PS_4, Li_3CuS_2 and Li_3CuS_2-Li_3PS_4 were performed and shown in figure 5.8, and the XAS of Li_3CuS_2-Li_3PS_4 is the combine spectroscopy of Li_3PS_4 and Li_3CuS_2. And XAS were also performed to clarify electronic structure changes of Li_3CuS_2-Li_3PS_4 (Figure 5.9a) during charge process, during the charge process the absorption peak at 2473 eV gradually shift to 2472 eV and the absorption peak at 2477 eV gradually shift to high energy, which may owing to the oxidation of S^{2-} to sulfur during charge process.[25] And the isosbestic point at 2472.6 eV can be observed during charge process, this can attribute to the two phase transition during charge process. Meanwhile, the absorption peak at 2471 eV which corresponding to S K-edge of Li_3PS_4, the peak intensity was gradually increased during charge process, this may corresponding the oxidation of Li_3PS_4.[26, 27]

Copper L-edge XAS was also performed during 1st charge process of Li_3CuS_2-Li_3PS_4(figure 5.9b),as the peak intensity of peak at 931.8 eV gradually increase during chare process, the copper may also be oxidized. And the isosbestic point can be observed at 934.5 eV, that may also attribute to the two phase transition during charge process.

X-ray Absorption Near Edge Structure (XANES) of copper K-edge during charge process were shown in Figure 5.10a. The copper K-edge was gradually shift to the higher energy, which corresponding to the oxidation of copper during the charge process. The copper k-edge of CuS was also shown as the reference in figure 7a and 7b, as the copper K-edge XAFS of Li_3CuS_2 gradually shift to CuS during charge process the final product was proposed as the CuS form our XAFS result.

Meanwhile Extended X-ray Absorption Fine Structure (EXAFS) of copper K-edge were also shown in Figure 5.10b. As the peak intensity around 1.8 Å increasing during charge process, that may owing to the increasing of Cu-S bond during the delithiation process. The reference EXAFS of CuS was also shown in figure 7b, as the EXAFS of Li_3CuS_2 during charge process is gradually fit to CuS, we believe that there are phase transition between Li_3CuS_2 and CuS during the charge process.

5.4 Conclusion

In this work, we successfully synthesized Li_3CuS_2 as a new type of all solid-state lithium sulfur battery cathode material. Furthermore, XAS was used to elucidate the reaction mechanism of Li_3CuS_2 during charging. These findings could facilitate the design of new types of cathode materials for all-solid-state lithium sulfur batteries.
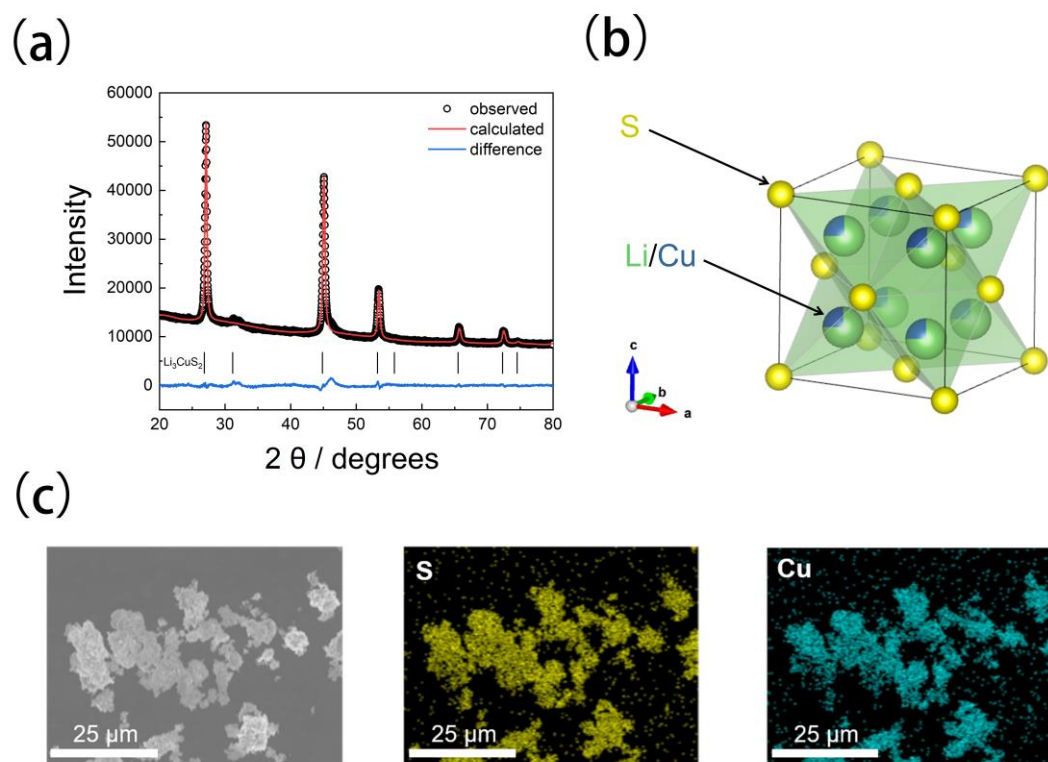
Figure 5.1. (a) synchrotron XRD of Li_3CuS_2 (b) crystal structure of Li_3CuS_2 (c) SEM image and EDX mapping for Li_3CuS_2.
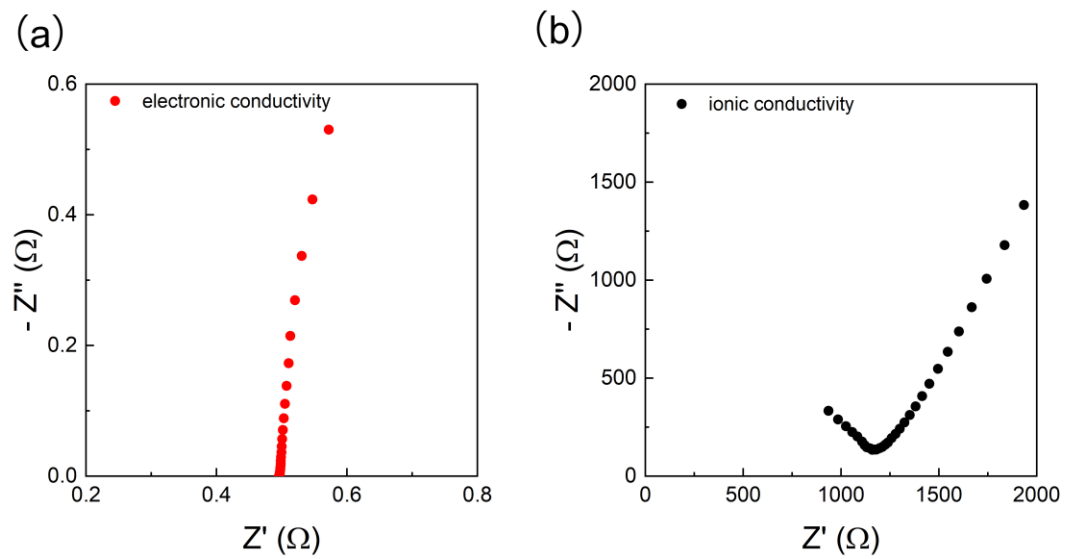
Figure 5.2. (a) electronic conductivity of Li$_3$CuS$_2$, (b) ionic conductivity of Li$_3$CuS$_2$.
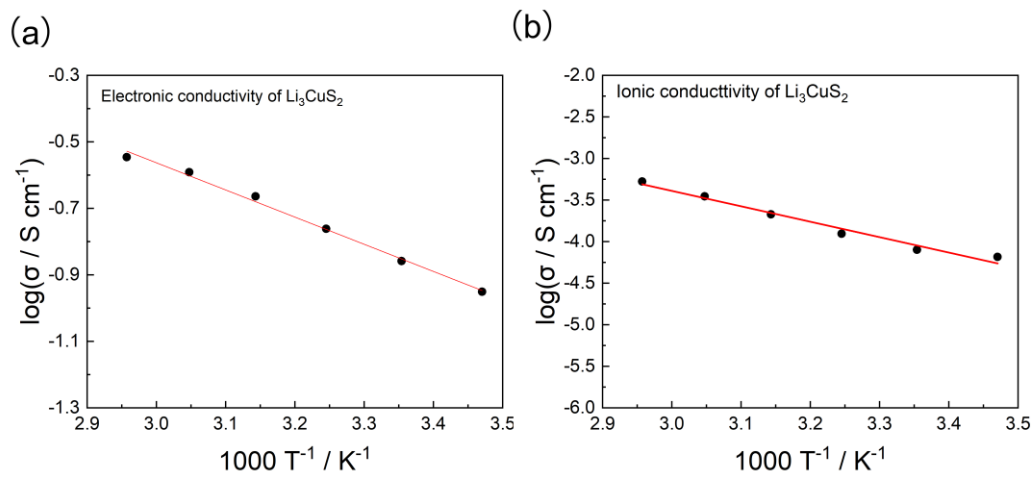
Figure 5.3. Arrhenius plot of (a) electronic conductivity of Li₃CuS₂, and (b) ionic conductivity of Li₃CuS₂.
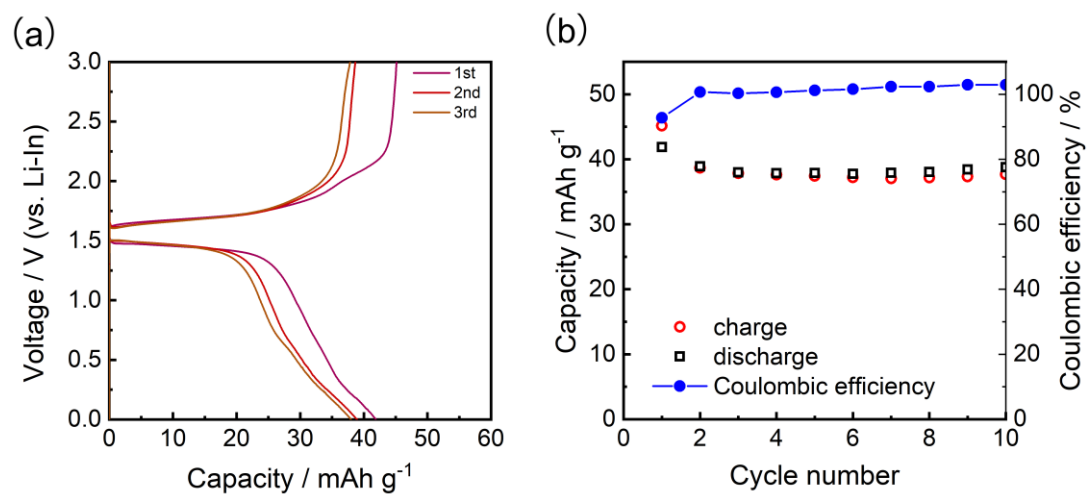
Figure 5.4 (a) Charge/discharge curves of Li_3CuS_2 cathode at current density 0.13 mA / cm^2, (b) charge and discharge cyclability of Li_3CuS_2 at 0.13 mA / cm^2.
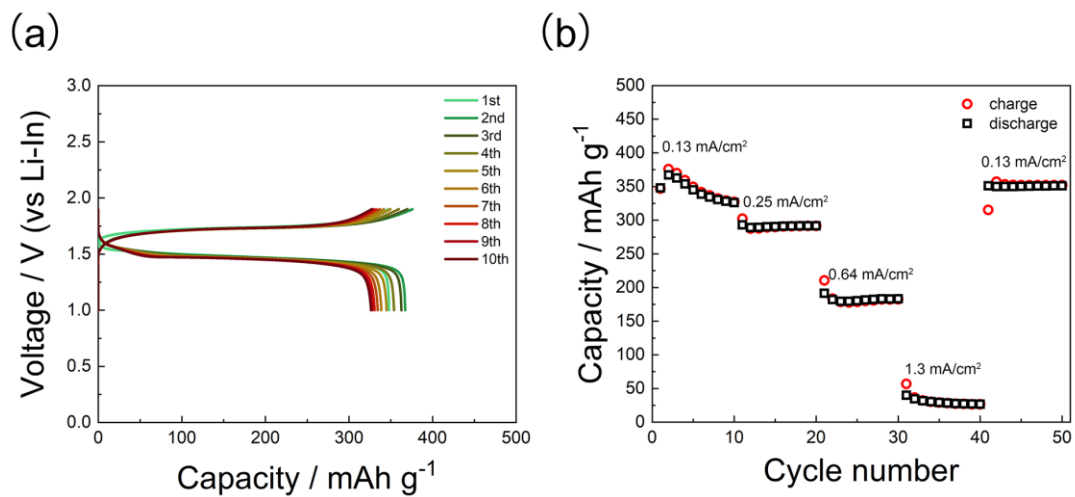
Figure 5.5. (a) Charge/discharge curves of Li_3CuS_2-Li_3PS_4 cathode, (b) cyclability of Li_3CuS_2-Li_3PS_4.
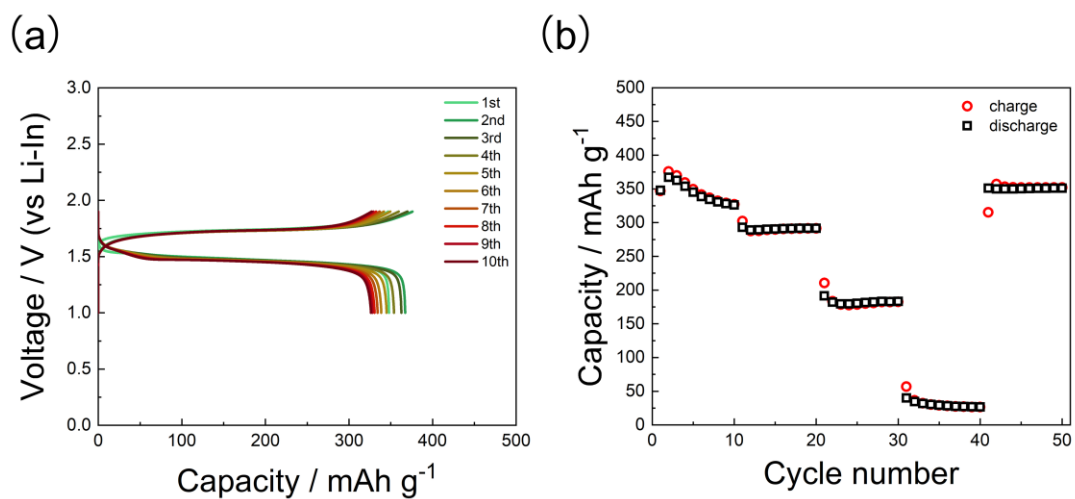
**Figure 5.6.** (a) Galvanostatic intermittent titration technique of Li_3CuS_2-Li_3PS_4 during charge and discharge process, (b) OCVs after charge and discharge.
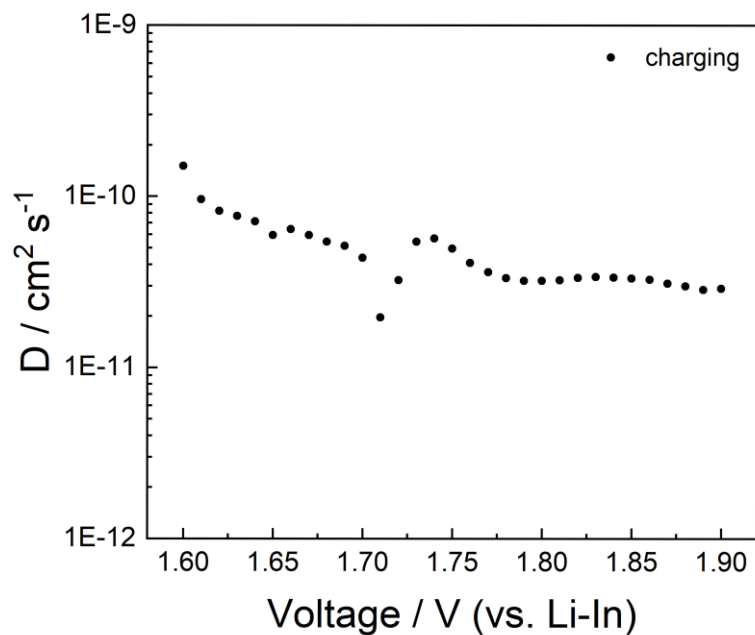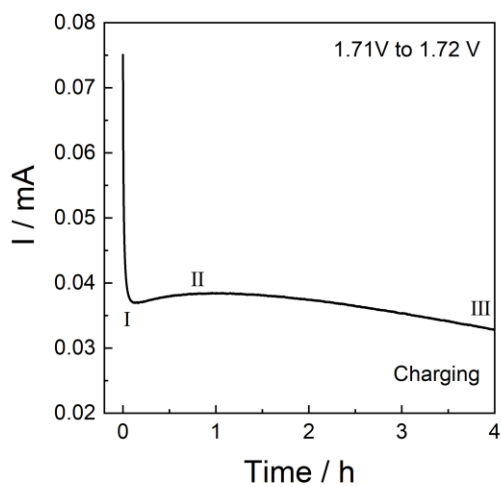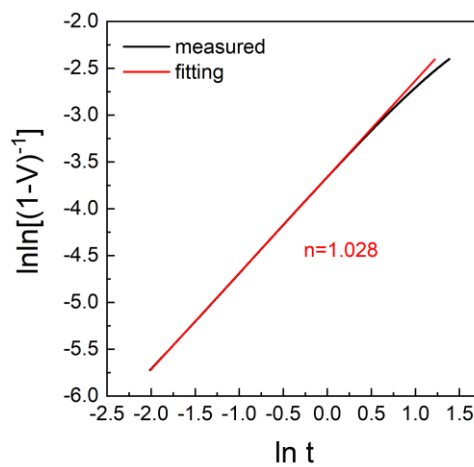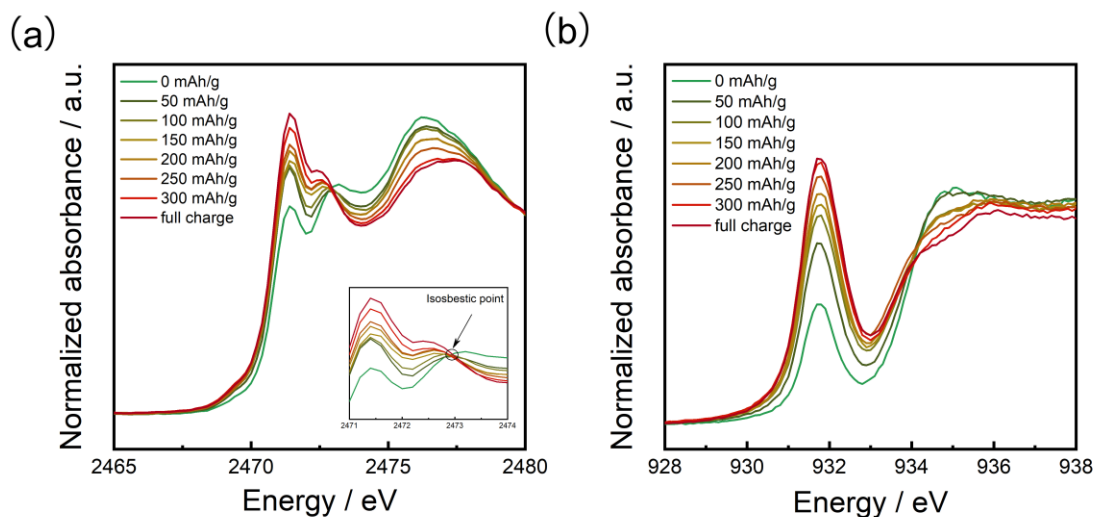
**Figure 5.7** (a) The Li$^+$ diffusion coefficient of Li$_3$CuS$_2$ calculated by PITT results, (b) The current response in potential-step chronoamperometry measurement from 1.71 charged to 1.71 V, (c) KJMA analysis for potential-step chronoamperometry measurement from 1.71 charged to 1.71 V.
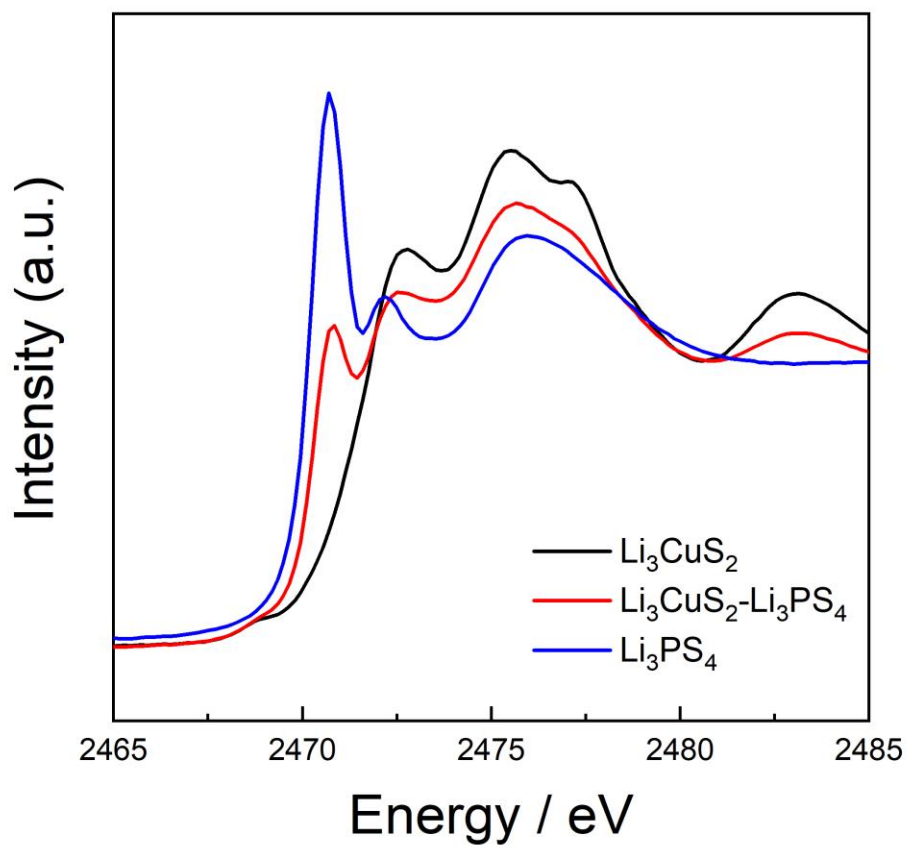
Figure 5.8. S K-edge XANES of Li_3PS_4, Li_3CuS_2 and Li_3CuS_2-Li_3PS_4.

Figure 5.9 (a) 1st charge curve of Li$_3$CuS$_2$-Li$_3$PS$_4$, (b) sulfur K-edge XANES of Li$_3$CuS$_2$-Li$_3$PS$_4$ cathode during 1st charge, (C) copper L-edge XANES of Li$_3$CuS$_2$-Li$_3$PS$_4$ cathode during 1st charge.
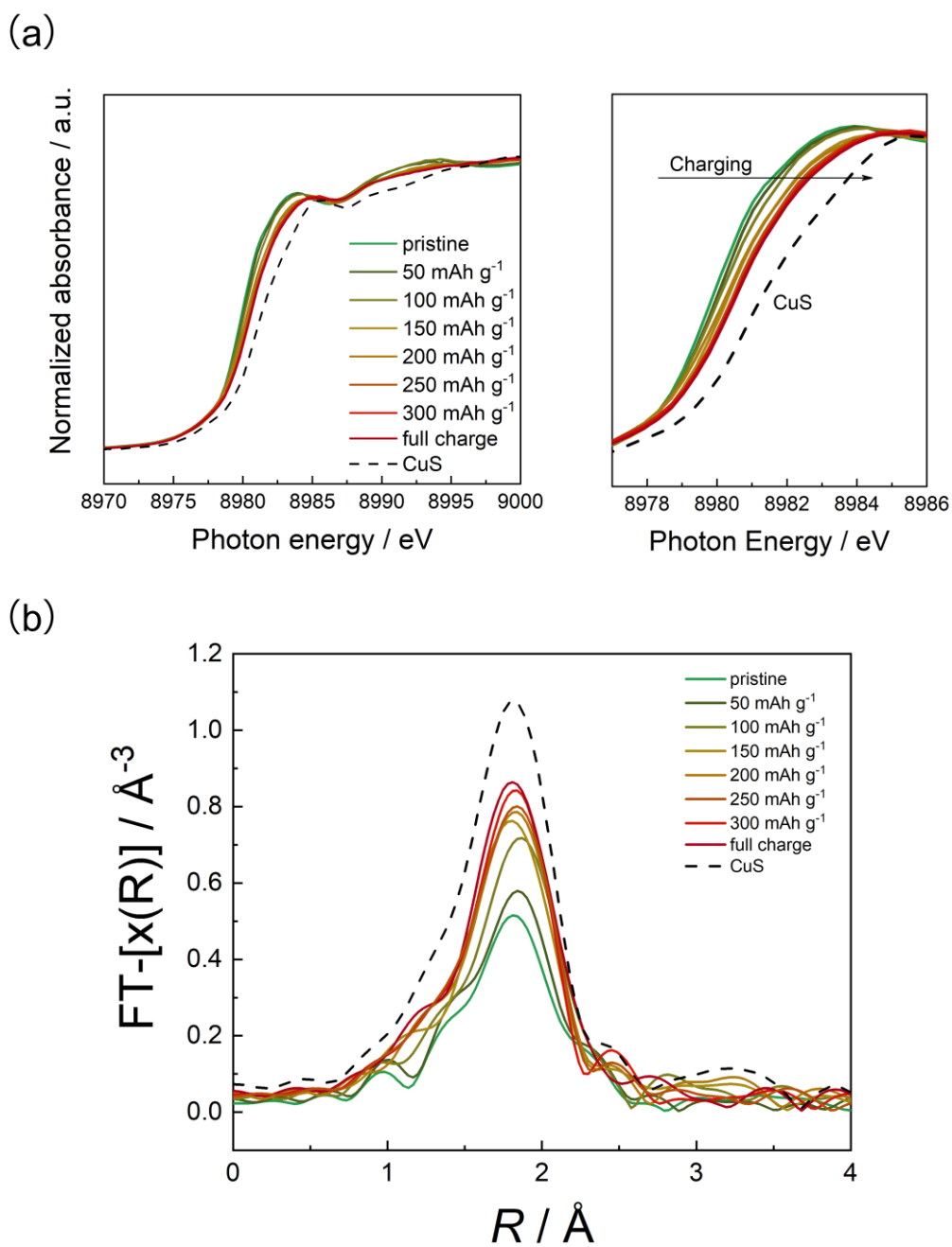
Figure 5.10 (a) XANES of copper k-edge of Li_3CuS_2-Li_3PS_4 during charge, (b) EXAFS of Li_3CuS_2-Li_3PS_4 during charge.

Reference

(1)   Ji, X. L.; Nazar, L. F. Advances in Li-S batteries. *J. Mater. Chem.* **2010**, *20*, 9821-9826.

(2)   Manthiram, A.; Fu, Y. Z.; Su, Y. S. Challenges and Prospects of Lithium-Sulfur Batteries. *Acc. Chem. Res.* **2013**, *46*, 1125-1134.

(3)   Yin, Y. X.; Xin, S.; Guo, Y. G.; Wan, L. J. Lithium-Sulfur Batteries: Electrochemistry, Materials, and Prospects. *Angewandte Chemie-International Edition*. **2013**, *52*, 13186-13200.

(4)   Mikhaylik, Y. V.; Akridge, J. R. Polysulfide shuttle study in the Li/S battery system. *J. Electrochem. Soc.* **2004**, *151*, A1969-A1976.

(5)   Manthiram, A.; Fu, Y. Z.; Chung, S. H.; Zu, C. X.; Su, Y. S. Rechargeable Lithium-Sulfur Batteries. *Chem. Rev.* **2014**, *114*, 11751-11787.

(6)   Pang, Q.; Liang, X.; Kwok, C. Y.; Nazar, L. F. Advances in lithium–sulfur batteries based on multifunctional cathodes and electrolytes. *Nat. Energy*. **2016**, *1*, 16132.

(7)   Seh, Z. W.; Sun, Y.; Zhang, Q.; Cui, Y. Designing high-energy lithium-sulfur batteries. *Chem. Soc. Rev.* **2016**, *45*, 5605-5634.

(8)   Bruce, P. G.; Freunberger, S. A.; Hardwick, L. J.; Tarascon, J. M. Li-O_2 and Li-S batteries with high energy storage. *Nat. Mater.* **2011**, *11*, 19-29.

(9)   Yin, Y.-X.; Xin, S.; Guo, Y.-G.; Wan, L.-J. Lithium-sulfur batteries: electrochemistry, materials, and prospects. *Angew. Chem., Int. Ed.* **2013**, *52*, 13186-200.

(10)   Evers, S.; Nazar, L. F. New Approaches for High Energy Density Lithium-Sulfur Battery Cathodes. *Acc. Chem. Res.* **2013**, *46*, 1135-1143.

(11)   Ellis, B. L.; Lee, K. T.; Nazar, L. F. Positive Electrode Materials for Li-Ion and Li-Batteries†. *Chem. Mater.* **2010**, *22*, 691-714.

(12)   Zheng, D.; Wang, G. W.; Liu, D.; Si, J. Y.; Ding, T. Y.; Qu, D. Y.; Yang, X. Q.; Qu, D. Y. The Progress of Li-S Batteries-Understanding of the Sulfur Redox Mechanism: Dissolved Polysulfide Ions in the Electrolytes. *Advanced Materials Technologies*. **2018**, *3*, 1700233.

(13)   Lin, Z.; Liang, C. Lithium–sulfur batteries: from liquid to solid cells. *J. Mater. Chem. A*. **2015**, *3*, 936-958.

(14)   Ueno, K.; Park, J.-W.; Yamazaki, A.; Mandai, T.; Tachikawa, N.; Dokko, K.; Watanabe, M. Anionic Effects on Solvate Ionic Liquid Electrolytes in Rechargeable Lithium–Sulfur Batteries. *J. Phys. Chem. C*. **2013**, *117*, 20509-20516.

(15)   Barchasz, C.; Lepretre, J. C.; Patoux, S.; Alloin, F. Electrochemical properties of ether-based electrolytes for lithium/sulfur rechargeable batteries. *Electrochim.*

Acta. **2013**, *89*, 737-743.

(16)   Dokko, K.; Tachikawa, N.; Yamauchi, K.; Tsuchiya, M.; Yamazaki, A.; Takashima, E.; Park, J. W.; Ueno, K.; Seki, S.; Serizawa, N.; Watanabe, M. Solvate Ionic Liquid Electrolyte for Li-S Batteries. *J. Electrochem. Soc.* **2013**, *160*, A1304-A1310.

(17)   Xin, S.; Gu, L.; Zhao, N. H.; Yin, Y. X.; Zhou, L. J.; Guo, Y. G.; Wan, L. J. Smaller sulfur molecules promise better lithium-sulfur batteries. *J. Am. Chem. Soc.* **2012**, *134*, 18510-3.

(18)   Yan, H.; Wang, H.; Wang, D.; Li, X.; Gong, Z.; Yang, Y. In Situ Generated Li_2S-C Nanocomposite for High-Capacity and Long-Life All-Solid-State Lithium Sulfur Batteries with Ultrahigh Areal Mass Loading. *Nano Lett.* **2019**, *19*, 3280-3287.

(19)   Yang, X.; Li, X.; Adair, K.; Zhang, H.; Sun, X. Structural Design of Lithium–Sulfur Batteries: From Fundamental Research to Practical Application. *Electrochemical Energy Reviews*. **2018**, *1*, 239-293.

(20)   Yue, J. P.; Yan, M.; Yin, Y. X.; Guo, Y. G. Progress of the Interface Design in All-Solid-State Li-S Batteries. *Adv. Funct. Mater.* **2018**, *28*, 1707533.

(21)   Han, F. D.; Yue, J.; Fan, X. L.; Gao, T.; Luo, C.; Ma, Z. H.; Suo, L. M.; Wang, C. S. High-Performance All-Solid-State Lithium-Sulfur Battery Enabled by a Mixed-Conductive Li_2S Nanocomposite. *Nano Lett.* **2016**, *16*, 4521-4527.

(22)   Nagao, M.; Hayashi, A.; Tatsumisago, M. High-capacity Li2S-nanocarbon composite electrode for all-solid-state rechargeable lithium batteries. *J. Mater. Chem.* **2012**, *22*, 10015-10020.

(23)   Matsuyama, T.; Hayashi, A.; Ozaki, T.; Mori, S.; Tatsumisago, M. Electrochemical properties of all-solid-state lithium batteries with amorphous MoS3 electrodes prepared by mechanical milling. *J. Mater. Chem. A.* **2015**, *3*, 14142-14147.

(24)   Asano, T.; Yubuchi, S.; Sakuda, A.; Hayashi, A.; Tatsumisago, M. Electronic and Ionic Conductivities of $LiNi_{1/3}Mn_{1/3}Co_{1/3}O_2$-$Li_3PS_4$ Positive Composite Electrodes for All-Solid-State Lithium Batteries. *J. Electrochem. Soc.* **2017**, *164*, A3960-A3963.

(25)   Li, X.; Banis, M.; Lushington, A.; Yang, X. F.; Sun, Q.; Zhao, Y.; Liu, C. Q.; Li, Q. Z.; Wang, B. Q.; Xiao, W.; Wang, C. H.; Li, M. S.; Liang, J. W.; Li, R. Y.; Hu, Y. F.; Goncharova, L.; Zhang, H. M.; Sham, T. K.; Sun, X. L. A high-energy sulfur cathode in carbonate electrolyte by eliminating polysulfides via solid-phase lithium-sulfur transformation. *Nat. Commun.* **2018**, *9*, 4509.

(26)   Camacho-Foreroi, L. E.; Balbuena, P. B. Elucidating Interfacial Phenomena between Solid-State Electrolytes and the Sulfur-Cathode of Lithium-Sulfur

Batteries. *Chem. Mater.* **2020**, *32*, 360-373.

(27) Hakari, T.; Deguchi, M.; Mitsuhara, K.; Ohta, T.; Saito, K.; Orikasa, Y.; Uchimoto, Y.; Kowada, Y.; Hayashi, A.; Tatsumisago, M. Structural and Electronic-State Changes of a Sulfide Solid Electrolyte during the Li Deinsertion–Insertion Processes. *Chem. Mater.* **2017**, *29*, 4768-4774.

Chapter 6 General conclusions

This thesis consists of six chapters, which report the reaction mechanisms of cathode materials for liquid and all-solid-state lithium sulfur batteries during charge–discharge and provide new insight into the design of cathode materials for lithium–sulfur batteries.

Chapter 1 briefly outlines the research background and fundamental principle of lithium-ion and lithium–sulfur batteries. Liquid and all-solid-state lithium sulfur batteries are introduced, and the cathode materials, electrolytes, and anode materials of the two types of batteries are discussed in detail.

Chapter 2 describes the changes in electronic structure of sulfur cathodes in conventional liquid, concentrated liquid, and solid-state electrolytes observed using X-ray absorption spectroscopy (XAS). And investigates the difference in the reaction pathway of sulfur cathode between the liquid and solid electrolyte by using soft X-ray absorption spectroscopy. We believe that these pieces of information about sulfur cathode will help to understand the reaction mechanisms of sulfur cathode and also to design the sulfur cathode with high electrochemical performance.

Chapter 3 focuses on clarifying the reaction mechanism of microporous carbon-supported sulfur cathodes using *operando* soft XAS. It was determined that the narrow pores of microporous carbon prevented the dissolution of polysulfides and affected the reaction mechanism of sulfur cathodes. Our results can provide further insights into the deeper understanding of the behavior of sulfur in carbon-supported cathodes, and it will be helpful for designing new cathodes with high performance.

Chapter 4 addresses the development of novel Li_2S–V_2S_3–LiI-based electrode active materials with excellent electronic and ionic conductivity. All-solid-state lithium sulfur battery featuring Li_2S, V_2S_3, and LiI composite electrode layers were fabricated and characterized to demonstrate their advantages in all-solid-state lithium sulfur battery. As no more electronic conductor and ionic conductor (such as carbon and solid-state

173

electrolyte) are need to add into the composite, we believe this research can helpful for guiding and designing of new kinds of cathode composite in all solid-state battery.

Chapter 5 describes the successful synthesis of Li_3CuS_2 as a new type of all solid-state lithium sulfur battery cathode material. Furthermore, XAS was used to elucidate the reaction mechanism of Li_3CuS_2 during charging. These findings could facilitate the design of new types of cathode materials for all-solid-state lithium sulfur batteries.

Chapter 6 presents the conclusions of this study and future prospects for lithium–sulfur batteries.

Acknowledgement

I would like to express my gratitude to all those who helped me during the writing of this thesis.

Firstly, I would like to express my sincere gratitude to my advisor Prof. Yoshiharu Uchimoto for his continuous support and help during my whole doctoral research. The perspective, motivation and encouragements from him help me to overcome the difficult in my research.

I also like to appreciate to Dr. Kentaro Yamamoto for his useful comments and discussions. I am also grateful to Dr. Koji Nakanishi, Dr. Tomoki Uchiyama and Dr. Toshiki Watanabe for their helps on measuring and analyzing XAS spectra. I also thank Prof. Toshiyuki Matsunaga for his helps on measuring and analyzing XRD patterns.

Finally, I would like to express my sincere thanks to all the members in Prof. Uchimoto's laboratory.

<div align="right">

Yao Xiao

Kyoto, Japan, November, 2020

</div>